



**CZECH TECHNICAL UNIVERSITY IN PRAGUE**

---

**Faculty of Civil Engineering  
Department of Physics**

## **Micro- and nanoscale diamond structuring**

### **DOCTORAL THESIS**

**Ing. Mária Domonkos**

Doctoral study programme: Civil Engineering

Branch of study: Physical and Material Engineering

Doctoral thesis tutors:

prof. RNDr. Pavel Demo, CSc.

doc. Ing. Alexander Kromka, DrSc.

**Prague, 2018**



**CZECH TECHNICAL UNIVERSITY IN PRAGUE**

**Faculty of Civil Engineering**

Thákurova 7, 166 29 Praha 6

## **DECLARATION**

Ph.D. student's name: Ing. Mária Domonkos

Title of the doctoral thesis: Micro- and nanoscale diamond structuring

I hereby declare that this doctoral thesis is my own work and effort written under the guidance of the tutor prof. RNDr. Pavel Demo, CSc..

All sources and other materials used have been quoted in the list of references.

The doctoral thesis was written in connection with research on the projects: SGS14/111/OHK1/2T/11, SGS16/197/OHK1/3T/11 and P108/12/G108 (GACR).

In Prague on .....

.....  
Signature

## Acknowledgements

*First of all, I would like to thank my supervisors, namely prof. RNDr. Pavel Demo, CSc. at the Czech Technical University in Prague and doc. Ing. Alexander Kromka, DrSc. at the Institute of Physics of the Czech Academy of Sciences for their careful guidance, for providing help and expertise throughout my studies and giving me opportunities for improving my knowledge, mainly in the field of experimental material research.*

*I am also grateful to my colleagues from the Institute of Physics of the Czech Academy of Sciences, who have been co-workers on various parts of this thesis. I have received technical assistance (e. g. SEM, AFM, Raman measurements, diamond deposition, simulations, etc.) and useful suggestions from them. I want to especially mention: Ing. Rayisa Yatskiv; Ing. Tibor Ižák, Ph.D.; Ing. Marián Varga, Ph.D.; Ing. Štěpán Potocký, Ph.D.; Ing. Karel Hruška; Mgr. Pavla Bauerová; Egor Ukraintsev, Ph.D.; RNDr. Lukáš Ondič, Ph.D. and Ing. Jan Fait.*

*Vašek Procházka, thanks for creating a fun filled environment and for the emotional support.*

*Anna Artemenko, Halyna Kozak, Jana Rezková, Pavla Štenclová, Rayisa Yatskiv, thanks for the ladies' lunches.*

*Hálával tartozom egykori tanárainknak, Papp Editnek és Szabó Endrének, akik megalapozták a fizika iránti érdeklődésemet és lelkesedésemet.*

*A szakmai segítség mellett a családomnak szeretnék köszönetet mondani. Szüleim biztosították a háttér tanulmányaim elvégzéséhez, bátyám pedig a számítógépeim karbantartását végezte.*

*Ezt a disszertációt férjemnek és nyelvi lektoromnak, Andornak ajánlom, aki rendíthetetlenül javította a cikkeimet és nyugodt környezetet biztosított a kutatásomhoz. Nem bírtam volna a támogatásod és a paradicsomos pennéd nélkül :)*

## Abstrakt

Překládaná disertační práce se zabývá nukleací, růstem a strukturováním tenkých vrstev polykrystalických diamantů.

V první části jsou popsány dvě alternativní metody používané k iniciaci nukleace a růstu diamantu a porovnány se standardními metodami nukleace. Spontánní nukleace probíhá na horizontálně a vertikálně orientovaných neupravených (tj. bez diamantového prášku) silikonových substrátech v lineárním plazmatickém systému CVD za různých hodnot parametrů depozice. Dále je zkoumána nukleace na bázi polymeru ve fokusovaném systému CVD. Byly použity různé polymery (polystyren-PS, polyaktát-glykolová kyselina a polyvinylalkohol) na křemíkových substrátech v různých formách (tj. mikrosféry, monovrstvy, vícevrstvy a kompozity se zabudovanými diamantovými nanočásticemi).

Druhá část práce se zabývá strukturováním mikro- a nanokrystalických diamantových tenkých vrstev pomocí litografie mikrokuliček (LMS). LMS je jednoduchou, spolehlivou, levnou (z hlediska vybavení a provozu) a materiálově nezávislou metodou výroby periodických polí nanostruktur pomocí samouspořádaných mikrosfér jako masky. Monovrstvy PS kuliček v hexagonálním uspořádání jsou připraveny na hladkých (Si) a drsných površích (diamantové filmy) použitím tzv. spin-coatingu. Jsou zde podrobně popsány základní problémy spin-coatingu (parametry procesu, drsnost povrchu podkladu, defekty). Po přípravě masky se monovrstvy kuliček modifikují pomocí leptání reaktivními ionty ve dvou různých plazmatických systémech. Vedle leptání v plazmě se používají různé procesní postupy (žihání, nanášení kovu/diamantu, odstranění kuliček) pro vytvoření požadovaných geometrických šablon. Výsledné nanostruktury mají širokou škálu aplikací v mnoha důležitých oblastech, jako je fotonika, plasmonika, senzorka, biomedicína, atd. V práci jsou popsány různé strategie výroby („top-down“ and „bottom-up“) periodických diamantových struktur. Příprava „kopečkovitých“ struktur je demonstrována výrobním procesem „top-down“ sestávající ze čtyř kroků (růst diamantů, příprava masky PS, úprava masky a leptání diamantu). Selektivní růst periodicky uspořádaných diamantových sloupců se provádí pomocí strategie „bottom-up“ (PS kuličky se používají jako mechanická maska pro plazmatické leptání diamantových vrstev).

Závěrem je realizována příprava polykrystalického diamantového dvourozměrného fotonického krystalu (tj. porézní struktura v hexagonálním uspořádání). Rozměry fotonického krystalu jsou vyladěny tak, aby měly vytékající vidy v blízké infračervené oblasti (1.31  $\mu\text{m}$ ). Srovnání simulace a měření propustnosti potvrzuje funkčnost fotonického krystalu.

**Klíčová slova:** diamant, nanofabrikace, litografie mikrokuliček, reaktivní iontové leptání

## Abstract

Presented doctoral thesis deals with nucleation, growth, and structuring of polycrystalline diamond thin films.

In the first part, two alternative methods used to initiate diamond nucleation and growth are investigated and compared to the standardly established nucleation methods. Spontaneous nucleation is studied on horizontally and vertically oriented non-treated (i.e. absence of pre-existing diamond seeds) silicon substrates in a linear plasma CVD system using different deposition parameters. Furthermore, polymer-based nucleation is studied in a focused CVD plasma system. Various polymers (polystyrene-PS, polylactic-co-glycolic acid and polyvinyl alcohol) are applied on silicon substrates in different forms (i.e. microspheres, monolayers, multilayers and composites with embedded diamond nanoparticles) to initiate diamond growth.

The second part of the thesis deals with the structuring of micro- and nanocrystalline diamond thin films using the technique of microsphere lithography (MSL). MSL is shown as a simple, reliable, inexpensive (in terms of equipment and operation) and material independent fabrication method for producing periodic arrays of nanostructures using self-assembled microspheres as a mask. Monolayers of PS spheres with hexagonal close-packed ordering are fabricated on smooth (Si) and rough surfaces (diamond films) using spin-coating. The essential issues of spin-coating (process parameters, substrate surface roughness, defects) are described in details. After mask preparation the close-packed sphere arrays are modified using reactive ion etching in two different plasma systems. Besides plasma etching various process steps (annealing, metal/diamond deposition, lift-off) are utilised to create the desired geometrical patterns. The resulting nanostructures have a wide range of applications in many important areas such as photonics, plasmonics, sensors, biomedicine. This thesis also covers various top-down and bottom-up strategies for manufacturing periodic diamond structures. The preparation of hillock-like structures is demonstrated using a four-step top-down fabrication process (diamond deposition, PS mask preparation, mask modification and diamond etching). Selective area deposition of periodically ordered diamond columns is realised using a bottom-up strategy (PS spheres are employed as a mechanical mask for plasma etching of the seeding layer).

Finally, the fabrication of a polycrystalline diamond-based two-dimensional photonic crystal slab (i.e. hexagonal lattice of air holes) is demonstrated. The dimensions of the structure are tuned to have a leaky mode in the near-infrared wavelength region at 1.31  $\mu\text{m}$ . Comparison of simulation and transmittance measurements confirm the functionality of the photonic crystal.

**Keywords:** diamond, nanofabrication, microsphere lithography, reactive ion etching

## Contents

<b>Acknowledgements .....</b>	<b>III</b>
<b>Abstrakt .....</b>	<b>IV</b>
<b>Abstract.....</b>	<b>V</b>
<b>List of abbreviations and acronyms.....</b>	<b>IX</b>
<b>INTRODUCTION .....</b>	<b>1</b>
<b>1. Motivation .....</b>	<b>2</b>
1.1 Objectives and organisation of the thesis .....	4
<b>2. Diamond.....</b>	<b>6</b>
2.1 Carbon allotropes .....	6
2.2 Diamond properties and applications .....	7
2.3 Diamond synthesis .....	9
2.3.1 Chemical vapour deposition .....	10
2.3.2 Diamond deposition phase diagram .....	11
2.4 Diamond film classification .....	12
2.5 Diamond nucleation and growth .....	13
2.5.1 Spontaneous nucleation .....	13
2.5.2 Polymer-based nucleation.....	14
2.6 Diamond film structuring .....	15
2.6.1 Porous diamond fabrication.....	17
2.6.2 Photonic crystal fabrication .....	18
<b>3. Microsphere lithography .....</b>	<b>19</b>
3.1 Introduction .....	19
3.2 Mask preparation.....	19
3.2.1 Self-assembly.....	19
3.2.2 Materials .....	20
3.2.3 Deposition methods .....	21
3.3 Applications of microsphere lithography .....	22
<b>EXPERIMENTAL PART .....</b>	<b>25</b>
<b>4. Processing and analytical techniques.....</b>	<b>26</b>
4.1 Chemical vapour deposition systems .....	26
4.1.1 Focused plasma CVD system .....	27
4.1.2 Linear plasma CVD system.....	27
4.2 Reactive ion plasma etching.....	28
4.3 Spin-coating .....	29
4.4 Employed procedures .....	30
4.5 Material characterisation and other equipment .....	30

<b>5.</b>	<b>Microsphere lithography .....</b>	<b>32</b>
5.1	Introduction.....	32
5.2	Mask preparation using spin-coating .....	32
5.2.1	Substrate properties .....	34
5.2.2	Colloidal dispersion .....	34
5.2.3	Critical process parameters of spin-coating .....	35
5.2.4	Analysis of the self-assembled monolayers .....	36
5.2.5	Defect formation .....	37
5.3	Post-assembly processing .....	38
5.3.1	Plasma etching .....	38
5.3.2	Evaporation and lift-off.....	44
5.3.3	Surface roughness .....	46
5.4	Conclusion .....	46
<b>6.</b>	<b>Diamond nucleation and growth .....</b>	<b>47</b>
6.1	Spontaneous nucleation and growth .....	47
6.1.1	Experimental .....	47
6.1.2	Results .....	48
6.1.3	Discussion .....	55
6.1.4	Conclusion.....	58
6.2	Three-dimensional diamond growth on a porous template .....	59
6.2.1	Experimental .....	59
6.2.2	Results and discussion.....	60
6.2.3	Conclusion.....	62
6.3	Polymer-based nucleation of diamond films .....	62
6.3.1	Experimental .....	62
6.3.2	Results and discussion.....	64
6.3.3	Conclusion.....	68
<b>7.</b>	<b>Structuring of polycrystalline diamond thin films.....</b>	<b>70</b>
7.1	Diamond film deposition and characterisation .....	70
7.1.1	Micro- and nanocrystalline diamond films .....	70
7.2	Maskless surface structuring of diamond films .....	72
7.2.1	Reactive ion etching in O <sub>2</sub> and CF <sub>4</sub> /O <sub>2</sub> gas mixtures.....	72
7.2.2	Reactive ion etching in SF <sub>6</sub> and Ar gas mixtures.....	73
7.2.3	Etching rates of diamond films .....	74
7.3	Structuring of diamond films using MSL: top-down strategy.....	76
7.3.1	Experimental .....	76
7.3.2	Results and discussion.....	77
7.4	Structuring of diamond films using MSL: bottom-up strategy.....	78
7.4.1	Experimental .....	79
7.4.2	Results and discussion.....	80

7.5	Conclusion.....	83
<b>8.</b>	<b>Fabrication of a diamond photonic crystal using MSL .....</b>	<b>85</b>
8.1	Experimental .....	85
8.1.1	Spin-coating on rough polycrystalline diamond films .....	85
8.1.2	Diamond photonic crystal design and fabrication .....	85
8.2	Results and discussion.....	87
8.2.1	Spin-coating on rough surfaces .....	87
8.2.2	Fabrication of diamond photonic crystal .....	89
8.2.3	Transmission measurements.....	92
8.2.4	Discussion and future prospects .....	94
8.3	Conclusion.....	95
	<b>SUMMARY .....</b>	<b>96</b>
<b>9.</b>	<b>Summary of the thesis .....</b>	<b>97</b>
	<b>References.....</b>	<b>101</b>
	<b>About the author .....</b>	<b>127</b>
	<b>List of publications.....</b>	<b>128</b>



## List of abbreviations and acronyms

2D	two-dimensional
3D	three-dimensional
a.u.	arbitrary units
AFM	atomic force microscope
CC	colloidal crystal
CCP	capacitively coupled plasma
CVD	chemical vapour deposition
DI	deionised water
DNP	diamond nanoparticle
EBL	electron beam lithography
FWHM	full width at half maximum
HPHT	high pressure high temperature
IR	infrared
MCD	microcrystalline diamond
MW	microwave
NCD	nanocrystalline diamond
NEMS	nano-electro-mechanical systems
NIR	near-infrared
MEMS	micro-electro-mechanical systems
MSL	microsphere lithography
PDMS	polydimethylsiloxane
PhC	photonic crystal
PLGA	poly (lactic-co-glycolic acid)
PMMA	polymethylmethacrylate
PS	polystyrene
PTV	peak-to-valley
PVA	polyvinyl alcohol
RCWA	rigorous-coupled wave-analysis
RF	radiofrequency
RIE	reactive ion etching
RMS	root-mean-square
SAD	selective area deposition
SEM	scanning electron microscope
SERS	surface-enhanced Raman spectroscopy
TE	transverse electric
UNCD	ultrananocrystalline diamond
UV	ultraviolet
VIS	visible



# **INTRODUCTION**

## 1. Motivation

Materials science and engineering is a large interdisciplinary field studying the composition, structure and properties of materials. It aims to design, develop and produce new materials with the desired micro/nanostructure as well as to improve existing products. Carbon is one of the most intriguing and abundant elements in the universe [1]. After the discovery of its allotropic nanoforms (graphene, nanoribbons, nanotubes, fullerenes, etc.), carbon-based materials have become a very important area of material research and nanotechnology due to their manifold properties.

Diamond has been the most sought-after gemstone since ancient times for its natural beauty, however, in the last century, synthetic diamond has also gained a reputation for its attractive physicochemical properties, such as robustness, low dielectric constant and loss, high thermal conductivity and excellent biocompatibility [2–5]. Furthermore, diamond has a wide bandgap (5.5 eV), high refractive index (2.41), wide transparency window from deep UV to the far IR, can be doped (n- and p-type) and can host different colour centres (e.g. nitrogen, silicon, erbium, boron) [6–9]. These properties make diamond a promising material for industrial and scientific purposes for a wide range of applications such as tooling (e.g. cutting, drilling, grinding, machining, polishing), anti-wear and corrosion coatings, electronic and semiconductor devices (e.g. high-power and high-frequency devices), optical components (e.g. window material for IR, X-ray, antireflection), electrochemical components (e.g. electrodes, sensors) and biomedical engineering (e.g. coating of stents, hip joints) [10].

Over the last 60 years, various techniques have been developed for the deposition of diamond thin films. Currently, chemical vapour deposition (CVD) is the most widespread technique for their synthesis. CVD techniques allow production of polycrystalline diamond films over large areas on various non-diamond substrates with reasonable growth rate and cost. The properties of deposited films (such as surface topography, morphology, grain shape and size, thickness, quality, doping, etc.) are tailorable on demand using synthesis steps in three main categories: i) pre-deposition treatments, ii) deposition, iii) post-deposition treatments [11].

Efficient diamond growth on non-diamond substrates requires some kind of surface pre-treatment due to the high surface energy of diamond relative to foreign substrates. To obtain fully closed films with good homogeneity and adhesion with a reasonable growth rate, various pre-treatment methods (e.g. scratching, seeding with

diamond particles, bias enhanced nucleation, etc.) are used to enhance the diamond nucleation.

The properties of the diamond films are further altered by the deposition technique used (gaseous phase activation, plasma type, reactor design), its process parameters (e.g. gas pressure, power, gas mixture, substrate temperature, etc.) and the substrate properties [12, 13]. Based on grain size, the deposited polycrystalline diamond thin films can be categorised into microcrystalline, nanocrystalline and ultrananocrystalline films. A smaller grain size results in a lower surface roughness and enhanced surface to volume ratio, however it also causes a higher  $sp^2$  (non-diamond phase) content due to the increased grain boundary area [14]. Understanding the relationship between the growth parameters and the resulting morphology makes it possible to design diamond structures for specific applications [15]. For example, diamond films with small grains and a low surface roughness are required for optical [16] and MEMS [17] applications, while thick films with large grains are needed for heat spreaders [18].

Surface modifications (e.g. surface patterning, functional terminations) can be used to further enhance the intrinsic properties of diamond films. The creation of new morphologies (such as whiskers, nanotips, nanocones, nanopillars, columnar structures etc.) with high aspect ratio expands the area of possible applications. However, due to its extreme properties (i.e. chemical inertness, high-temperature stability and hardness), it is difficult to structure diamond [19]. Generally speaking, the fabrication of diamond structures can be realised either using a top-down strategy (i.e. structuring after the growth process), or a bottom-up strategy (pre-growth structuring, also known as selected area deposition).

Various lithographic techniques are the current standard in the fabrication of micro- or nanoscale diamond structures in a controlled fashion [20]. Although these sophisticated techniques have almost reached perfection in precision, most of them (e.g. electron-beam lithography, focused ion beam lithography) suffer from high costs and relatively long fabrication times, especially for processing large areas ( $\sim \text{cm}^2$ ) [21]. Thus, it is highly desirable to develop a more favourable method for sculpting diamond structures. Alternative lithographic techniques, such as nano- or microsphere lithography (MSL) could become strong competitors to the aforementioned lithographic techniques [22]. The principle of MSL is based on the self-assembly of monodisperse microspheres (e.g. polystyrene,  $\text{SiO}_2$ , etc.) into a hexagonal close-packed (hcp) monolayer or a face-centered cubic multilayer [23, 24]. These arrays of spheres can then be used as masks or templates for various subsequent deposition, etching or imprinting processes [25–27]. MSL is a material independent fabrication approach capable of manufacturing a wide variety of 1D–3D tailor-made (different feature size, shape, lattice constant, etc.) periodic structures [28–30].

## 1.1 Objectives and organisation of the thesis

The presented thesis deals with polycrystalline diamond thin films synthesised using chemical vapour deposition. The motivation is to study diamond films from various aspects important to the fabrication of diamond-based structures. The experimental work is separated into two main topics. In the first part, nucleation and early stages of growth are studied, which are critical in producing films with specific properties. Two alternative nucleation methods are investigated and compared to the standardly established methods. The second part focuses on the fabrication of diamond-based structures. Various pre- and post-growth procedures are utilised for the fabrication of periodic diamond structures.

The experimental work of the PhD research was realised at the Joint Laboratory of the Institute of Physics (Department of Optical Materials) of the Czech Academy of Sciences and the Faculty of Civil Engineering (Department of Physics) of the Czech Technical University in Prague.

This thesis consists of 9 chapters:

Chapter 1 presents the motivation and concept of the experiments.

Chapter 2 gives a literature survey on diamond thin films (properties, applications, synthesis and structuring of polycrystalline thin films).

Chapter 3 deals with microsphere lithography (basic concept, mask preparation methods, potential applications).

Chapter 4 focuses on the processing (CVD deposition systems, reactive ion etching, spin-coating) and analytical techniques (scanning electron microscopy, atomic force microscopy, Raman spectroscopy, etc.) used for the experiments.

Chapters 5 to 8 describe the experimental results of this thesis, which are divided into two main parts. The first part (Chapter 6) presents results and discussion on the nucleation and growth of diamond thin films in linear and focused microwave plasma CVD systems. The second part (Chapters 7 and 8) covers various strategies used for the structuring of diamond thin films. Finally, the main results of the thesis and some outlooks for future work are summarised (Chapter 9).

---

A brief outline of the topics and basic concepts of the experiments:

## **I. Diamond nucleation and growth**

### **1) *Spontaneous nucleation***

- optimisation of process parameters (e.g. deposition duration, gas mixture) in order to achieve high nucleation density on non-treated Si substrates
- study of the effect of sample orientation (vertical and horizontal)
- better understanding of the diamond nucleation and growth mechanisms in a linear antenna CVD plasma system

### **2) *Polymer-based nucleation***

- application of various polymer films as a seeding layer to initiate diamond growth in a focused CVD plasma system
- testing of different kinds (e.g. PS, PVA, PLGA) and forms (e.g. microspheres, thin films, composites) of polymers

## **II. Structuring of diamond thin films**

### **1) *Maskless***

- reactive ion etching of micro- and nanocrystalline diamond films using different process parameters

### **2) *With mask - microsphere lithography***

- study of the technological details of MSL (mask preparation, modification and removal)
  - optimisation of spin-coating process parameters to create homogeneous arrays of microspheres over a large area
  - development of new masks (various materials, geometry) using reactive ion etching of monolayers with varying etching parameters
- development of different routes for the fabrication of various periodic diamond arrays using bottom-up and top-down strategies

## 2. Diamond

### 2.1 Carbon allotropes

Carbon is essential for all forms of life on Earth and is without a doubt one of the most important natural elements in the periodic table. It is the 2<sup>nd</sup> most abundant element in the human body, the 15<sup>th</sup> most abundant element in the Earth's lithosphere, and the 4<sup>th</sup> most abundant in the universe [31].

The neutral carbon atom bears six electrons – two tightly bound (1s) close to the nucleus and four as valence electrons (two in the 2s subshell and two in the 2p subshell) [32]. The ground state electron configuration of carbon ( $1s^2 2s^2 2p^2$ ) allows it to bond in three different ways (single, double and triple bonds) and with many different elements. For this reason, carbon manifests itself in many different allotropic forms with entirely different properties [33]. All of them have the same building block, the carbon atom, but their crystalline structure is different. The three basic carbon allotropes with an integer degree of carbon bond hybridisation are carbene, graphite and diamond corresponding to  $sp$ ,  $sp^2$  and  $sp^3$  hybridisation of the atomic orbitals (Figure 2.1) [34].

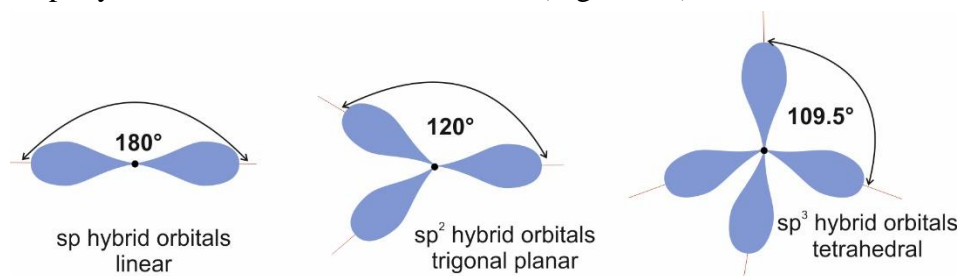


**Figure 2.1 Drawing of  $sp$ ,  $sp^2$  and  $sp^3$  hybrid orbitals [34].**

- $sp$  hybridisation (linear): one s-orbital hybridises with one of the p-orbitals to make two  $sp$ -hybridized orbitals. The angle between these new orbitals is  $180^\circ$  and the carbon atom bonds by a diagonal symmetry.

- $sp^2$  hybridisation (trigonal planar): one s-orbital is mixed with two of the p-orbitals to form three hybridised orbitals with a trigonal symmetry and with characteristic  $120^\circ$  angles between them [31].



- $sp^3$  hybridisation: each carbon atom is arranged tetrahedrally. Each tetrahedron combines with four other tetrahedra and forms a strongly bonded, entirely covalent face-centred cubic crystal structure (Figure 2.2). Diamond can also exist in a hexagonal (lonsdaleite) form [36].

There are other allotropes of carbon that have also received considerable attention due to their usefulness in material science [35]. Carbon allotropes of all dimensionalities are known, but there is no consensus on how many are defined at present. Moreover, other new forms are predicted (e.g. novamene, 2017) [37].

Several well-known allotropes of carbon are graphite (1917), fullerene (1970), nanotube (1991), graphene (2004), nanobud (2006) (Figure 2.3), nanodiamond, nanofoam, nanoribbon, nanohorn, nanosheet, etc. [38]. This structural diversity allows many different types of scientific and technological utilisation.

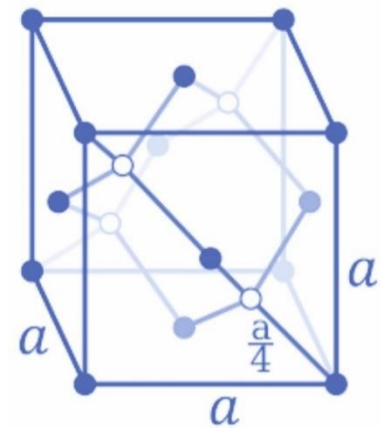


**Figure 2.2 Diamond lattice structure [35].**

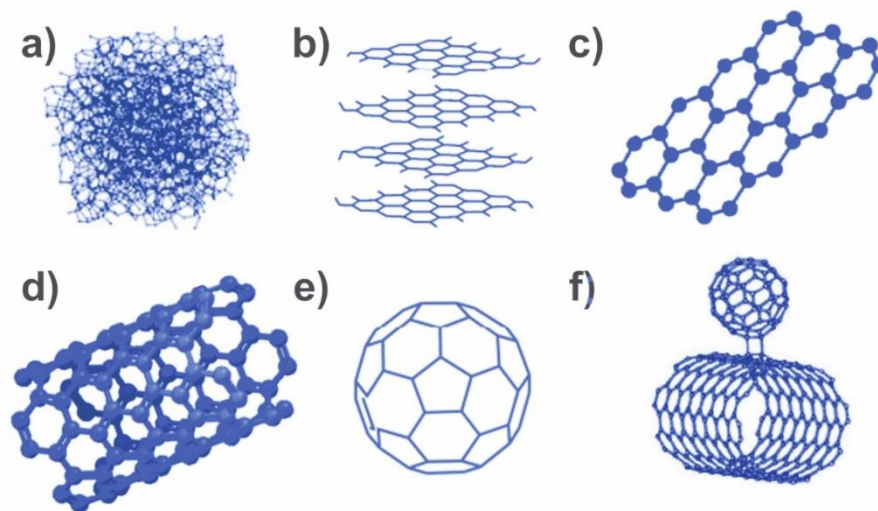


**Figure 2.3 a) Amorphous carbon and selected carbon allotropes: b) graphite, c) graphene, d) nanotube, e) fullerene f) nanobud [35].**

## 2.2 Diamond properties and applications

Natural diamond is one of the most highly prized gemstones in the world. It is renowned for its bright sparkle, rarity and precision. The ancient Greeks, combining the words “adamas” (unbreakable or invincible) and “diaphanes” (transparent), gave the name diamond, perfectly suggesting the qualities of this stone: hardness and clarity [39]. Natural diamond is formed at a depth of more than 150 km in the mantle of Earth at a pressure of more than 4.5 GPa and temperatures between 900 and 1300 °C, then volcanic

eruptions bring them to the surface [31]. Its carbon composition was determined by Antoine Lavoisier in 1772. The oldest, and at the same time one of the biggest diamond surviving to our day (105.6 carats, cut down from 186 carats = 37.2 g) is the Kooh-i-Noor.

Diamond is an outstanding material. Its selected valuable properties, which make it suitable for industrial use, are summarised in Table 2.1 [40]. Due to these unique thermal, mechanical, optical and electrical properties, diamond films have a broad number of applications such as optical components, nano- and microelectromechanical systems (NEMS/MEMS), sensors, etc. (Figure 2.4).

**Table 2.1 Selected properties of diamond [5, 41–43].**

Property	Value	Comments
hardness	9 000 kg/mm <sup>2</sup> (Mohs 10)	the hardest, the least compressible and the best thermal conductor among all natural materials; applications: windows for CO <sub>2</sub> lasers, cutting tools, heat sinks
Young's module	$3.5 \times 10^9$ Pa	
thermal conductivity *	20 W/cmK	
density	3.51 g/cm <sup>3</sup>	high
chemical reactivity *	extremely low	resistance to chemically harsh environments
optical transparency	from 225 nm to near IR	gem, windows and mirrors for high power IR lasers, beam splitters
refractive index (at $\lambda = 10 \mu\text{m}$ )	2.32 – 2.42	optical, IR detectors
absorption coefficient (at $\lambda = 10 \mu\text{m}$ )	$< 0.1 \text{ cm}^{-1}$	Fresnel lenses
electrical properties *	indirect bandgap: 5.45 eV	insulator, photodetector
doping	boron: p-type bandgap: 0.37 eV phosphorus: n-type bandgap: 0.6 eV	semiconductor
biocompatibility	high	natural science, biosensorics, drug and gene delivery, coating body implants, tissue engineering,

\* at room temperature and pressure

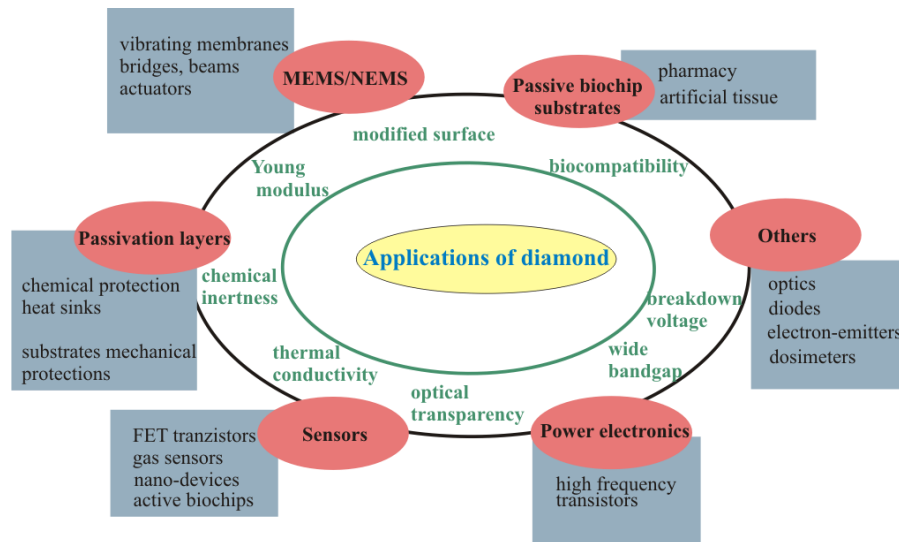


Figure 2.4 Selected properties and potential applications of diamond films [5, 41–43].

### 2.3 Diamond synthesis

The phase diagram of carbon (Figure 2.5) shows which phase is thermodynamically preferred for a given temperature and pressure. At high temperatures and pressures, diamond is thermodynamically more stable (i.e. has lower free energy) than graphite. At ambient conditions, diamond is metastable relative to graphite, since it is kinetically stable and thermodynamically unstable [43]. Conversion of diamond to graphite is thermodynamically favourable but does not occur because the kinetics of the reaction are extremely slow. Due to these facts, diamond synthesis was hampered for a long time. Over the past few decades, a variety of techniques have been developed for the production of synthetic diamond [33, 40].

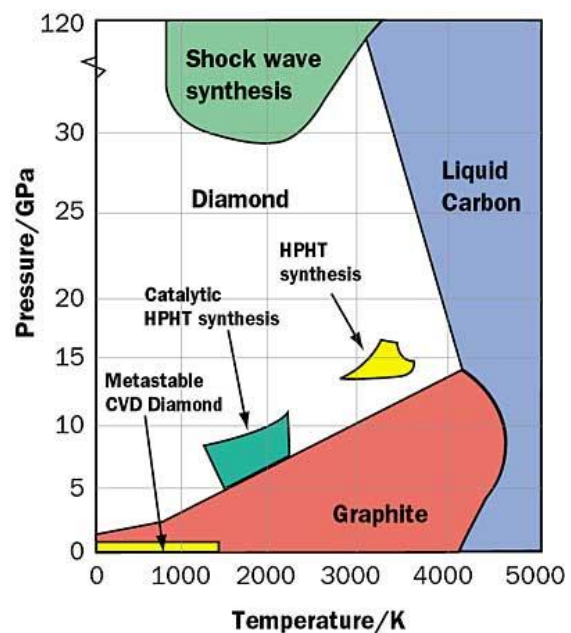


Figure 2.5 The phase diagram of carbon [44].

The age of industrial diamond began in 1955 when General Electric (F.P. Bundy et al.) started the production of diamond using the high pressure-high temperature (HPHT) technique. The HPHT synthesis of diamond essentially imitates natural diamond formation, i.e. conversion of graphite to diamond. [31, 42]. However, this technique can only produce crystals with limited size, mainly suitable for mechanical applications (e.g. grinding and cutting tools). Other thermodynamically stable methods of diamond production are shock wave and detonation synthesis [45].

### 2.3.1 Chemical vapour deposition

The major breakthrough in diamond synthesis came in the mid-1960s with the discovery of chemical vapour deposition (CVD) by William G. Eversole (Union Carbide Corporation, United States) [32, 42]. It was realised that diamond synthesis outside of its thermodynamically stable region is possible (Figure 2.5). In this case, the synthesis is a kinetic rather than thermodynamic process. The deposition occurs at low pressures (below one atmosphere) and moderate temperatures (200 °C – 1200 °C) [46].

In the early experiments, the growth rate was too low for practical usage, later on, high deposition rates were limited to small areas and high temperatures. Today the technology is developing at a rapid rate. New types of reactors have been developed, a significant increase in the deposition rate, improvement in the material quality, reduction of deposition temperatures and reduction in production cost has been achieved [46]. In recent years the deposition of diamond films at low temperatures (< 400 °C) on a large area (e.g. 20 × 30 cm<sup>2</sup>) became achievable in linear antenna microwave plasma systems (see section 4.1.2) [47].

As the name of the CVD method implies, the process involves a large number of chemical reactions inside a vapour phase as well as deposition onto a substrate surface. The accurate theory (thermodynamics, plasma physics, kinetics, chemistry, etc.) of the process is not fully understood and described at this time [48]. The following points briefly summarise the basic stages of the conventional diamond CVD process [31, 41, 42, 49].

**0) Surface pre-treatment** of the non-diamond substrate is desired due to the high surface energy of foreign substrates. The substrate surface must be susceptible to support the heterogeneous nucleation and subsequent growth of the diamond film. This means that the substrate surface should be at the solubility limit for carbon (at the specific deposition parameters) in order to stimulate the nucleation of diamond on the surface instead of the concurrent diffusion of carbon into the substrate.

**1) Activation of gas phase** by an external source of energy: thermal activation (hot filament), plasma activation (radiofrequency, microwave, plasma-jet), chemical activation (combustion flame) [50]. For our experiments, microwave (MW) enhanced plasma systems were used (see section 4.1). The microwave generated plasma is attractive because its excitation frequency (2.45 GHz) can oscillate electrons. High ionisation of plasma is achieved through the collisions of gas species. These types of plasma are typically described as having “hot” (~ 5000 °C) electrons and “cold” (~ 800 °C) ions and neutrals.

**2) Production of various gas species** via chemical reactions.

The plasma consists of randomly oscillating electrons, ions, atoms, molecules and radicals. This gas mixture must contain a carbon-containing species (e.g. methane, carbon monoxide, carbon dioxide, acetylene, ethylene, etc.) and a sufficiently high concentration

of species (like atomic hydrogen), which etch or suppress the non-diamond phases during the deposition [32, 51].

**3) Transport of gas species** to the substrate.

In most cases, the driving force for the transport of carbon-containing species to the substrate is a temperature gradient (the activated gas phase is much hotter than the substrate surface). The transport of species may also be enhanced by electric fields.

**4) Chemical reactions** of gas species on the substrate surface.

**5) Nucleation and growth** of individual crystallites, faceting, coalescence of crystallites, formation and growth of fully closed film [39].

### 2.3.2 Diamond deposition phase diagram

In 1991 Bachmann et al. summarised numerous reliable experimental data of diamond depositions and constructed a triangle diagram, the so-called atomic C–H–O phase diagram [52]. The diagram comprised more than 80 deposition experiments (different types of reactors, C:H:O ratios in the gas phase, etc.) covering 30 years of research. The experimental data were divided into three regions: no growth, diamond growth and non-diamond carbon growth (Figure 2.6) [53, 54].

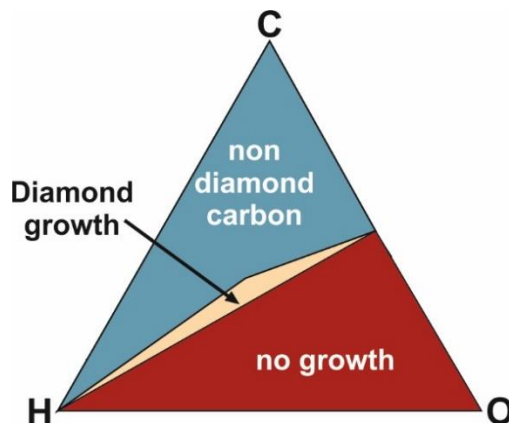


**Figure 2.6 Simplified atomic C-H-O diamond deposition phase diagram [55].**

Standard CVD diamond growth is realised in hydrogen-rich gas mixtures containing 1–5% methane ( $\text{CH}_4$ ), which acts as the source of carbon. The activation of the gas phase breaks down the input gas and initiates a cascade of exothermic chemical reactions, which produce hydrocarbon free radicals and dissociates the stable hydrogen diatomic molecule ( $\text{H}_2$ ) into free atoms. [46].

Atomic hydrogen plays an important role in the deposition process, its critical role was recognised during the 1990s. In contrast to molecular hydrogen, atomic hydrogen is extremely reactive and selectively etches non-diamond carbon phases (at least twenty times faster than diamond). Moreover, atomic H interacts with the surface hydrogen atom and forms molecular hydrogen, which may depart from the substrate surface leaving behind a vacancy. Then the carbon from a methyl radical ( $\text{CH}_3$ ) fills the vacancy, thus continuing the carbon lattice. Unfortunately, the vacancy is more probable to be filled by another atomic hydrogen (10 000 times) than by a carbon radical [54, 56, 57].



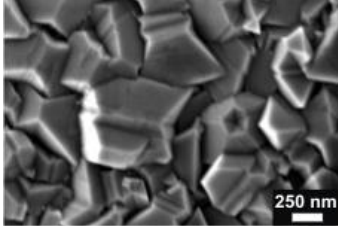
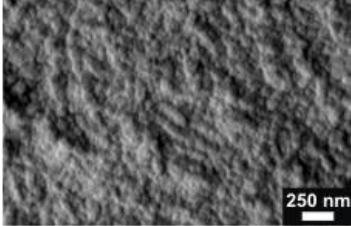
Addition of small amount of oxygen-containing compound (e.g.  $\text{O}_2$ ,  $\text{CO}_2$ ) to the gas mixture enhances the deposition rate as well as the quality of the diamond films [58].

Addition of proper elements (e.g. boron, phosphorus) results in p- and n-type doping of the films [59].

## 2.4 Diamond film classification

Laboratory-grown diamond films fall into two basic categories: monocrystalline (i.e.  $sp^3$  bonded one crystal or grain) and polycrystalline diamond. Monocrystalline one is formed by homoepitaxial growth and requires a monocrystalline substrate (natural or synthetic diamond).

**Table 2.2 Comparison of microcrystalline (MCD), nanocrystalline (NCD), ultrananocrystalline (UNCD) diamond film properties.**

	MCD	NCD	UNCD
<b>Schematics of growth mechanisms</b>		→	
<b>Growth mechanisms</b>		→ crystal growth is hindered secondary nucleation enhanced higher presence of $sp^2$ phases and grain boundaries	
<b>SEM images</b>		→	
<b>Growth chemistry</b>	hydrogen-rich plasma	→	hydrogen-deficient plasma, argon-, nitrogen-rich plasma
<b>Re-nucleation velocity</b>	low	high	very high
<b>Grain size</b>	5–10 $\mu\text{m}$	below 100 nm, usually 10–100 nm	below 10 nm, usually 2–5 nm
<b>Surface roughness</b>	0.4–1 $\mu\text{m}$ rough surface	50–100 nm relatively smooth surfaces	20–40 nm smooth surfaces
<b>Possible applications</b>	cutting tools, abrasive coatings, heat sinks	optics, MEMS	coatings for 3D structures, biological applications

Polycrystalline diamond film is cheaper to produce than monocrystalline, partly because it can be grown on a variety of substrates. It consists of randomly oriented crystallites containing a varying amount of non-diamond carbon phases and defects. Depending on crystal size it can be divided into micro-, nano- and ultrananocrystalline diamond (Table 2.2). Polycrystalline diamond thin films synthesised using chemical vapour deposition are recognised as promising materials for various applications [10, 39,

60]. Their properties (topography, morphology, quality) is controlled by synthesis conditions (pre-treatments, deposition type and its process parameters, post-treatments, etc.) [11]. Understanding the relationship between the synthesis conditions and morphology makes it possible to design diamond structures for specific applications [15].

## 2.5 Diamond nucleation and growth

Fundamentally, the diamond film synthesis is divided into two main stages, namely, nucleation and growth [61]. Nucleation is one of the least understood processes of the diamond deposition [62, 63]. Nucleation and the early stages of diamond growth have significant effects on properties of the formed film [12, 13]. They influence the size and crystallographic orientation of the growing crystals, their chemical purity (i.e.  $sp^3$  to  $sp^2$  ratio), film homogeneity, morphology, diamond-substrate interface (e.g. induced stress and adhesion of the film to the substrate), etc. [64, 65].

### 2.5.1 Spontaneous nucleation

Spontaneous nucleation and subsequent diamond growth on non-diamond surfaces without pre-treatment are very complex and slow processes (i.e. they require long incubation durations). The high surface energy of diamond relative to foreign substrates (e.g.  $6 \text{ J/m}^2$  to  $1.5 \text{ J/m}^2$  in the case of silicon), low sticking coefficient of gaseous precursors and the competition of non-diamond phases are the most crucial factors blocking spontaneous diamond growth [14, 66, 67]. The efficiency of the nucleation process can be expressed by the surface nucleation density ( $N_d$ ), i.e. the number of nuclei formed per unit area ( $\text{cm}^{-2}$ ), often approximated and indirectly calculated as the number of diamond grains per  $\text{cm}^2$  visible after the CVD process [62]. In the case of non-treated Si substrates the intrinsic  $N_d$  is very low, typically  $\sim 10^3$ – $10^5 \text{ cm}^{-2}$  [68]. Thus, several pre-treatment methods have been successfully developed for enhancing the nucleation density, such as scratching of the substrate surface with abrasive material (e.g. diamond paste or particles) [69], bias enhanced nucleation (for conductive substrates) [70–72], ultrasonic seeding with diamond nanoparticles or in combination with metal nanoparticles [66, 73–76] and polymers (see section 6.3) [77], etc. The used method controls the properties of the final diamond film, thus, it directly determines its industrial uses. For example, homogeneous diamond films with small grains and low surface roughness are required for optical [78], biomedicine and MEMS [17] applications, while thick films with large grains are needed for heat spreading [18]. Typical nucleation densities for pre-treated non-diamond substrates vary from  $10^8$  to  $10^{12} \text{ cm}^{-2}$ . Presently, these methods are becoming routinely used. However, they are limited in treating substrates with complex geometry or soft/unstable substrates such as polymers, thin metal films, optical mirrors, membranes or electrically insulating substrates (glass or ceramics), etc. They can easily cause surface damage (microscopic

defects or scratches), impurities or incomplete (non fully closed) diamond coverage [79–81].

In the experimental part of this thesis (section 6.1) spontaneous nucleation in a linear plasma CVD system is presented. It is demonstrated that if clean Si substrates (without pre-treatment procedure) are exposed to proper deposition parameters, high nucleation density can be achieved.

## 2.5.2 Polymer-based nucleation

Recently, considerable effort has been dedicated to innovative polymer-based nucleation methods, where the polymer acts as a carrier matrix for embedded diamond nanoparticles [82–84] or as a primary carbon source for the  $sp^2$  to  $sp^3$  transformation [85–87]. Using polymer composites, it is possible to achieve relatively high density of diamond nanoparticles on the substrate and the subsequent growth of a fully closed ultrathin diamond film (below 100 nm). It has also been shown that polymer coatings are suitable for the nucleation of substrates with complex 3D geometry. Girard et al. [88] provided seeding of 3D substrates with high aspect ratio. This method is based on the electrostatic interactions between the oxygen-terminated nanodiamonds (characterised by a negative zeta potential) and the cationic polymer-coated sample. Opposite charges caused grafting of particles to the substrate surface via the thin polymer layer, which is then immediately removed during the first seconds of the chemical vapour deposition.

Polymer composites were also used in the form of nonwoven textiles containing diamond nanoparticles [89, 90]. These nanofibre composites were produced by needleless electrospinning [91] and were found to be effective for coating copper rods with diamond thin film. In this case, nanofibre composites also contributed to the inhibition or suppression of carbon diffusion into copper as well as to the lateral stress compensation [90]. Another study has shown that diamond nanoparticles (DNPs) dispersed in the PVA matrix led to the formation of long fibre-like diamond structures. This effect was attributed to the combined effect of seeding by DNPs, the pressure difference ( $\sim$  GPa) across the fibre interface and local nanocracks. The highest concentration of DNPs resulted in the growth of a nearly fully closed diamond film on Si substrates. For low DNP concentration in the PVA polymer matrix, shortening of the fibre-like structures and the lowering of surface coverage was observed [89]. All these results confirm that utilizing PVA polymer nanofibres with diamond nanoparticles is a rapid, simple and economically favourable method to nucleate different substrate materials with 3D geometry on a large scale.

In the abovementioned strategies, diamond growth is primarily initialized by the diamond nanoparticles. However, there is also a possibility of transformation of polymers into diamond structures or films. Recently, polycarbynes, such as poly(methylcarbyne), poly(phenylcarbyne) or poly(hydridocarbyne) [92], have aroused interest among researchers for their potential application as polymeric precursors to promote diamond



growth. Poly(phenylcarbyne), as a carbon-based random network polymer, was transformed into diamond-like carbon or diamond phases at atmospheric pressure by thermal decomposition (at 1000–1600 °C for 7 h in argon ambient) [93]. Successful transformation of poly(methylcarbyne) to diamond was achieved by Nur et al.[86] via sintering under atmospheric pressure of nitrogen at 1000 °C for 24 h. Early studies about poly(phenylcarbyne) as a seeding layer on silicon substrates exposed to hot filament CVD revealed enhanced nucleation densities [85, 94] and growth of isolated diamond crystals in sizes ranging from nanometres up to micrometres was observed. However, applying other polymers (phenolic resin, polyethylene, pump oil, etc.) as precursors did not result in diamond growth at lower substrate temperatures (400–500 °C) [77].

In the experimental part of this thesis (section 6.3) polymer-based nucleation in a focused plasma CVD system is presented. Three types of polymers (polystyrene, polylactic-co-glycolic acid, and polyvinyl alcohol) is applied in different forms, i.e., microspheres, monolayers, multilayers and composites with embedded diamond nanoparticles.

## 2.6 Diamond film structuring

The current and potential applications of diamond films depend not only on their intrinsic physical and chemical properties but also on their morphology [95]. Structuring the surface of diamond film (i.e. fabrication of nanorods, nanoneedles, nanorings, nanocones, nanowires, porous structures, etc.) increases its attractiveness for various applications such as life science applications [96–98], MEMS/NEMS devices [99], etc. For example, a high surface-to-volume ratio enhances the overall performance of sensors (including sensitivity and selectivity) [100, 101]. NCD films are excellent substrates for the adhesion and growth of various types of cells. However, the substrate topography (i.e. size and shape of the surface irregularities) has a significant effect on cell behaviour (e.g. differentiation, survival rate, etc.) [102]. Surface structuring also enhances the field-emission properties of diamond films due to the local-field enhancement effect, which makes them a promising material for field emission devices and photonics [103, 104]. Representative diamond structures and their potential applications are shown in Figure 2.7.

Nanostructuring methods can be divided into two major categories: bottom-up strategy (i.e. assembling atomic or molecular building blocks into more complex nanoscale structures) and top-down strategy (i.e. creating nanostructures with desired geometries from bulk materials) [105]. Due to high-temperature stability, super hardness and chemical inertness, it is hard to structure diamond, e.g. wet chemical etching is not applicable.

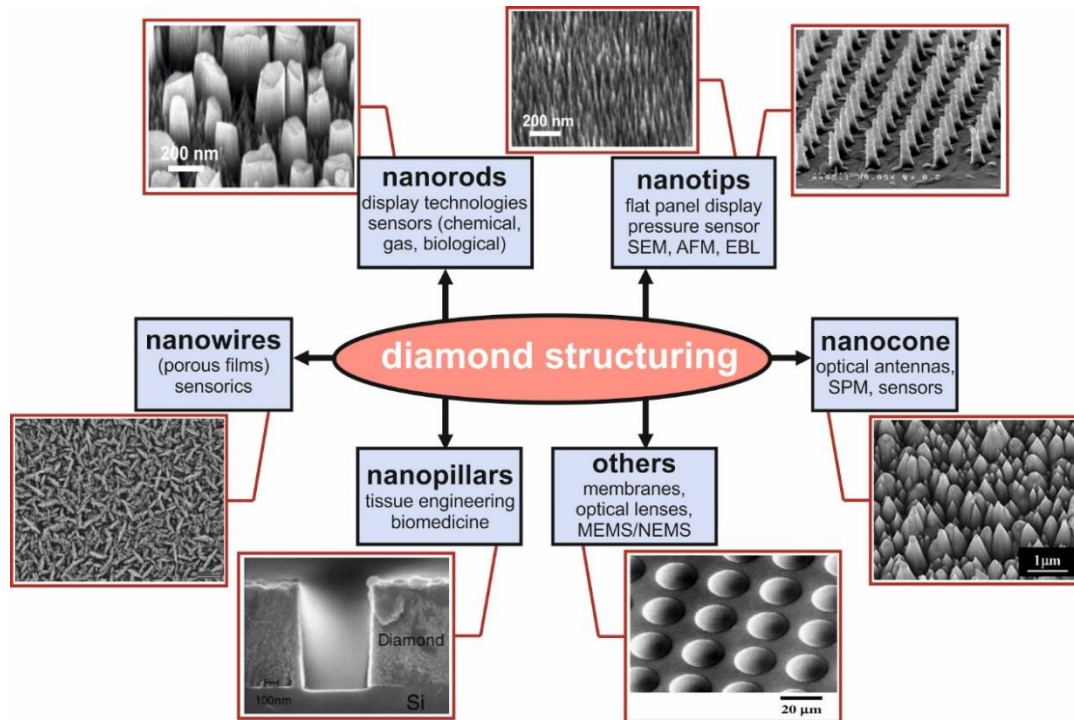


**Figure 2.7** Illustration of diamond structuring and its potential applications [95, 106–111].

Top-down strategies (i.e. post-growth structuring) remove selected areas from fully closed films [107, 112]. Reactive ion plasma etching through a mask is used most commonly. The morphology and geometrical patterns of the final structures are defined by the etching mask (e.g. material, size, shape) and etching parameters (power, pressure, gas mixture, duration, etc.). A broad family of possible masking materials (metals, polymers, oxides, nitrides, etc.) is available. The masks are usually created using lithographic techniques (photolithography, electron beam lithography, nanoimprinting, etc.) [113]. However, these processes are cost-intensive and time-consuming. Hence, there is an effort to develop new masking methods such as masks from self-organised and self-assembled metal [104, 114, 115] or polymer nanoparticles (e.g. microsphere lithography).

Compared to the top-down strategies, bottom-up (i.e. pre-growth structuring) strategies are less investigated and their usage is less frequent due to their higher complexity and lower process reliability. Bottom-up strategies are based on the templated growth of diamond films. i.e. diamond growth occurs only on certain areas of the substrate (henceforth selective area deposition, SAD) [116]. SAD requires surfaces with considerable difference in nucleation density. Selective area nucleation can be achieved by nucleating pre-defined areas only (e.g. ink-jet printing, selective BEN) [117] or by the removal of diamond seeds from pre-defined areas (e.g. microsphere lithography, see section 7.4) [28]. After these treatments, the selectivity of diamond film formation on pre-treated (enhanced nucleation) and clean (suppressed nucleation) areas is very high. SAD allows the fabrication of non-periodic or periodic diamond structures without etching.

However, the deposition of high aspect ratio structures is challenging, because diamond crystals grow in three dimensions.

In the experimental part of this thesis, the structuring of polycrystalline diamond thin films will be demonstrated using different concepts (both top-down and bottom-up strategies), without the use of a mask and using various masks/templates (microspheres, metal mask, fibres). Porous diamond membranes will be created using templated growth (see section 6.2). Periodic diamond structures (Chapter 7) and photonic crystals (Chapter 8) will be fabricated using microsphere lithography.

### 2.6.1 Porous diamond fabrication

Over the last decades, significant effort has been devoted to producing porous and self-standing diamond-based membranes. They stand out with extremely high specific surface area, furthermore their properties are easily tunable (porosity, depth of penetration, functionalization, wettability, etc.). However, their fabrication is not a trivial task. For the preparation of such structures, templated growth seems to be an ideal approach, i.e. deposition of diamond within a 3D template such as carbon foam, SiO<sub>2</sub> spheres, fibres, etc. [118].

In section 6.2 it will be demonstrated that fibrous materials are promising candidates as a template for porous diamond membrane fabrication. Fibrous materials attract considerable attention due to their specific characteristics, such as a large specific surface area, high bending performance, flexible surface functionality, good breathability, controllable basis weight (fibre weight per area) and porosity (fibre density) with excellent pore interconnectivity [119, 120]. These unique features and properties make them useful for a wide variety of applications such as filtration, separation, catalysis, adsorption, fibre-reinforced composites, tissue engineering, drug delivery systems, sensors, wound dressings, energy conversion and storage, etc. [121, 122].

Electrospinning [120] (or electrostatic spinning) is a versatile way of preparing nano/microfibers from a broad range of materials. Almost any soluble polymer with sufficiently high molecular weight (e.g. polyolefine, polyamides, polyester, aramid, acrylic) as well as carbon and silica-based fibres can be electrospun [123]. Electrospinning has gathered interest from both academia and industry due to its simple setup and relatively high production rate. It is capable of producing fibres with complex 2D or 3D shapes in sub-micron or even nanometre diameter range unlike conventional fibre techniques (wet spinning, drawing, phase separation, dry spinning, melt spinning, etc.) [124, 125]. It is possible to prepare fibres with both smooth and porous surface features. Porous nanofibers have an even larger surface area compared to smooth fibres. Furthermore, small insoluble particles (e.g. diamond powder), soluble drugs or bacterial agents can be added to the polymer solution and electrospun into fibres.

Nanofibers produced using electrospinning are collected in the form of mats, which can be used as a 3D porous template for diamond deposition [126]. This strategy

is a promising way to combine the advantages of porous structures and diamond film properties [127–130]. Porous diamond structures can control (electro-) chemical processes and serve as converter or catalyst between the bio-, electro-chemical reactions, can facilitate migration of epidermal cells, etc. Furthermore, they can be used for the selective detection of molecules or the stimulated regulation of biological processes.

In section 6.2 a simple, low-cost and effective technique (seeded electrospun  $\text{SiO}_x$  fibre mats coated with polycrystalline diamond film) will be presented for manufacturing a self-standing diamond membrane with a porous 3D structure.

### 2.6.2 Photonic crystal fabrication

The fascinating properties of diamond make it an ideal material for multispectral optical applications, including photonics [131]. Although single-crystal diamond is a better candidate for optical devices than polycrystalline diamond, the production and machining of single-crystals are quite cumbersome [132]. In contrast, a polycrystalline diamond film with desired properties (thickness, morphology, grain size) can be easily and inexpensively deposited on a wide range of substrates and over large areas [133]. It also retains many of the unique characteristics of the single-crystal diamond. Certainly, polycrystalline diamond has its drawbacks. Its slightly poorer optical properties are a consequence of light scattering due to surface roughness, absorption losses, and nonuniform optical properties due to the presence of non-diamond carbon phases located at the grain boundaries [134, 135]. Despite these limitations, polycrystalline diamond has also been successfully used as an eligible material for the realisation of various optical applications [136–139].

Photonic crystals (PhC) are periodic structures artificially designed in one-, two- or three-dimensions for monitoring, controlling or modification of light inside the structure [140]. One of the most important applications of the 1D and 2D PhC structures in photonics is a very efficient coupling of incident light from outside into a planar waveguide. The same structure can also be used reciprocally, i.e. as an efficient light outcoupler. Both these effects appear thanks to the existence of the so-called leaky modes, i.e. the modes of the PhC that are extracted to the surroundings by the Bragg diffraction on the periodicity. Wavelength and angle of the extracted light are given by the geometry and dimensions of the PhC. PhCs with two-dimensional periodicity can also be employed as polarization splitters [141]. However, the fabrication of such periodically arranged uniform nanostructures on large areas is a challenging task. This is particularly true in the case of diamond [19]. Microsphere lithography (see Chapter 3) offers the possibility to realise diamond photonic structures with dimensions tuned for the extraction/coupling of specific wavelengths, such as 738 nm (emission band of SiV centres), 1.31 and 1.55  $\mu\text{m}$  (telecommunication windows).

## **3. Microsphere lithography**

### **3.1 Introduction**

Nanostructuring is an important step in modern material engineering to achieve the desired properties of materials and their surfaces for a variety of applications. Reliable, cost and time efficient nanostructuring methods compatible with industry are always welcome. Both nanostructuring strategies (bottom-up and top-down) have their drawbacks. Some techniques are cumbersome and slow, others require prohibitively expensive equipment, often produce only two-dimensional structures, and almost all require clean rooms and controlled environments [142]. It is highly desirable to develop an effective alternative method for fabrication micro- and nanostructured surfaces [143].

Microsphere lithography (MSL) seems to be a promising technique in this regard because it takes advantage of the combination of bottom-up growth with top-down patterning [144]. Micro- or nanosphere lithography is the more recent term used in literature to describe this method, but it is also referred to as natural lithography [145], colloidal lithography [146] and shadow nanosphere lithography [147]. It allows high spatial resolution over a large patterned area with a relatively low density of defects, has high throughput and can generate well-ordered, 1D–3D periodic structures from a variety of materials on many substrates [148]. It also does not require the time-consuming and expensive step of making a mask with standard lithography techniques. Of course, the ability to generate arbitrary patterns is limited by the lithographic mask [29].

### **3.2 Mask preparation**

#### **3.2.1 Self-assembly**

The first stage of MSL, i.e. mask preparation is inspired by self-assembly phenomenon, which is omnipresent in nature at both macroscopic and microscopic scales [149]. Self-assembly is defined (at all scales) as a closed process in which the unordered set of building blocks spontaneously forms an ordered, stable and static structure that reaches thermodynamic equilibrium. The reversible transition from the initial state (unordered) to the final (ordered) one takes a finite amount of time without human intervention [150, 151]. Researcher realised, the process of self-assembly is also very powerful from a technological point of view. Under appropriate conditions the self-assembly of particles results in organised structures i) monolayer (2D) or ii) multilayer

(3D) periodic arrays [152]. These arrays usually referred to as colloidal crystal, serve as lithographic masks for MSL [29, 153]. Thermodynamically these structures tend to adopt the lowest Gibbs free energy available to them (e.g. spherical particles tend to form a hexagonal close-packed (hcp) or face-centred cubic lattices) [29]. There are three types of forces that are crucial in colloidal self-assembly: i) intrinsic driving forces for the ordering of monodisperse spheres into ordered arrays (entropy-driven process), ii) external forces (e.g. gravity, centrifugation, etc.) (bring the spheres together) and iii) repulsion forces (prevent premature aggregation of spheres) [154, 155].

### 3.2.2 Materials

A rich variety of colloidal particles, including polymers (polystyrene – PS, polymethyl methacrylate – PMMA, poly (lactic-co-glycolic acid) – PLGA), silica (silicon dioxide – SiO<sub>2</sub>) spheres are commercially available from a number of companies (microParticles GmbH, Phosphorex Inc., Bangs Labs Ltd., Duke Scientific, etc.) as dry powder or water dispersion [156, 157]. These particles with narrow size distribution (5–7 %) are synthesised with emulsion, dispersion, precipitation, emulsifier-free polymerisation [158], Stöber process [159], etc. The spheres are available with varying properties: size (diameter, concentration, distribution), composition (density, refractive index) and surface chemistry (hydrophobicity/-philicity, level of functionalization, charge). Some manufacturer also provides hybrid particles: spheres with porous morphology, hollow spheres, spheres with shells of various material, with impregnated VIS or fluorescent dyes.

Polystyrene-based and silica particles with a diameter ranging from 200 to 1300 nm are by far, the most commonly studied spheres because of their ease of synthesis and processing. Polystyrene (density: 1.05 g/cm<sup>3</sup>, refractive index at 589 nm 1.59) is a popular polymer due to its excellent properties, such as its rigidity, low water absorbability, non-biodegradability, low cost and good processability (self-assembly, etching, lift-off, etc.). The main advantage of the silica (density: 2.0 g/cm<sup>3</sup>, refractive index at 589 nm 1.43–1.46) spheres is their high thermal stability, i.e. they can be processed at significantly higher temperature than polymer ones. However, to remove them is more complicated (e.g. using hydrofluoric acid).

Common polymer spheres are generally hydrophobic, they tend to aggregate in the aqueous dispersion. The probability of the aggregation decreases as the diameter of the spheres increases (due to enhanced Brownian motion). Thus, the colloidal dispersions usually contain surfactant agent (e.g. 0.01–0.1% anionic sodium dodecyl sulphate, nonionic sorbitan monolaurate (Tween 20), sodium bicarbonate, potassium sulfate), which provides charge stabilisation and reduce the hydrophobicity [160]. Aqueous silica dispersions rarely require the use of stabilisers, because the spheres are inherently hydrophilic and negatively charged.

### 3.2.3 Deposition methods

In recent years, numerous research groups have been working on different methods for the homogenous spreading of microspheres over planar or non-planar substrate surfaces. Various methods [29, 144, 161] have been developed successfully – vertical, horizontal and tilt methods, e.g. drop-coating, spin-coating, dip-coating, electrophoretic deposition [162], inkjet-printing, template-directed assembly [163], etc. However, the creation of reproducible, large area and high-quality films (i.e. low concentration of defects) is still a fundamental challenge [164, 165]. Selected methods [149, 150, 166, 167] are described in the following paragraphs. With these methods, the monolayer can cover macroscopic scales (several mm<sup>2</sup> up to several cm<sup>2</sup>).

Evaporation methods are based on solvent evaporation from a droplet of microsphere dispersion deposited on a substrate. The evaporation rate determines the ordering and quality of the obtained arrays [149]. **Drop-coating** involves simply placing drops of the dispersion onto the substrate, and subsequently allowing the solvent to evaporate. The substrate surface can be inclined vertically or slightly tilted. The attractive capillary force and convective transport of the microspheres arising from the continuous solvent evaporation are the main factors dominating the self-assembly process. By reducing the temperature, the evaporation rate can be lowered to allow the spheres time to assemble. Nonetheless, this method is not very well controlled [29, 168].

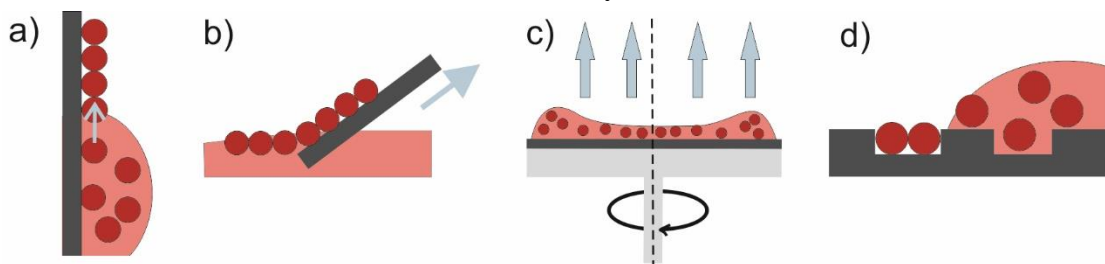


**Figure 3.1 Schematic illustration of diverse mask preparation methods a) dip-coating, b) self-assembly at the gas/liquid interface, c) spin-coating, d) template-directed self-assembly.**

**Dip-coating** is precision controlled immersion of a substrate into a reservoir of dispersion and allowing the excess liquid to drain off (Figure 3.1a) [29]. The control of the evaporation rate is achieved by a step motor, which helps to lift up the wettable substrate from the dispersion at a controlled rate. The film thickness is controlled by several parameters, including the immersion rate, the liquid (e.g. concentration, viscosity, etc.) and substrate (wettability) intrinsic properties and the number of times that the process is repeated. This procedure is suitable for large area monolayer preparation. However, the arrays are formed on both sides of the substrate, which increases the amount of material used [168–170].

Another commonly used method is *self-assembly at the interface of two different media* (e.g. Langmuir-Blodgett method). In this case, the microspheres are dispersed on

the top of the surface of the liquid medium (i.e. liquid-gas interface) [158, 171]. Due to a carefully prepared surface condition, particles are trapped at the interface and self-assemble into a monolayer. Subsequently, the monolayer is deposited on the substrate by a simple removal procedure or by evaporation of the liquid (Figure 3.1b). The colloidal mask can be transferred to any kind of solid substrate (flat, curved, rough). However the monolayer can be easily damaged when it is transferred to the target substrate, therefore, it requires delicate precision skills [172–175].

**Spin-coating** (Figure 3.1c) has some advantages over previous methods, the foremost being speed: large area monolayers (wafer-scale samples) can be routinely fabricated in minutes [176]. In this method, the dispersion is spread over the substrate, which is placed on a rotary stage. The rapid spinning movement of the stage makes the liquid flow away. When the dispersion layer thickness becomes smaller than the diameter of the spheres, capillary forces start pulling spheres together, forming a 2D array [150, 171].

Chemically or physically **pre-patterned substrates** can also be used as masks for MSL. This method has an increased time and cost of sample preparation due to the additional preliminary step in the process. However, more diverse structures can be obtained. Physically patterned substrates are produced using standard lithographic methods (Figure 3.1d). Chemically patterned substrates have a wettability or local charge contrast. These methods are sometimes referred to as “guided” or “templated” assembly because the pre-patterned array guides the spheres into pre-defined spots [29].

### 3.3 Applications of microsphere lithography

In practical utilisation, the functional properties of nanostructured materials are highly dependent on the shape and size of the nanostructures. MSL is a powerful process for the manufacture of a variety of ordered nanostructure arrays, including nanotips, nanowires, nanopillars, nanobowls, nanovoids, nanopores, circular nanorings, hemispherical nanowells, etc. Nonetheless, the controllability of the nanostructure arrays is limited compared to conventional lithographic methods [163, 165, 177]. In recent years, these structures have attracted widespread interest because of their potential applications in numerous fields. They can be used as sensors (e.g. plasmonic, bio- and chemical), filters, surface wetting layers, solar cells, masks for selective deposition, electronic and optical devices, etc. The potential applications in civil engineering/architecture cover both the field of a new generation of sensors for toxic-gases (located in the interiors of buildings) and also development of advanced protective layers of materials (e.g. antibacterial, hydrophobic, hydrophilic).

The following subsections review selected applications of self-assembled polystyrene microsphere monolayers for photonics, sensorics and selective growth [178].



### Surface-enhanced Raman spectroscopy

One of the first applications for periodically ordered nanostructures was related to the sensitive and selective detection of single molecules by using surface-enhanced Raman spectroscopy (SERS). SERS is a vibrational spectroscopy technique based on the plasmonic resonance of thin metal periodic nanostructures [179].

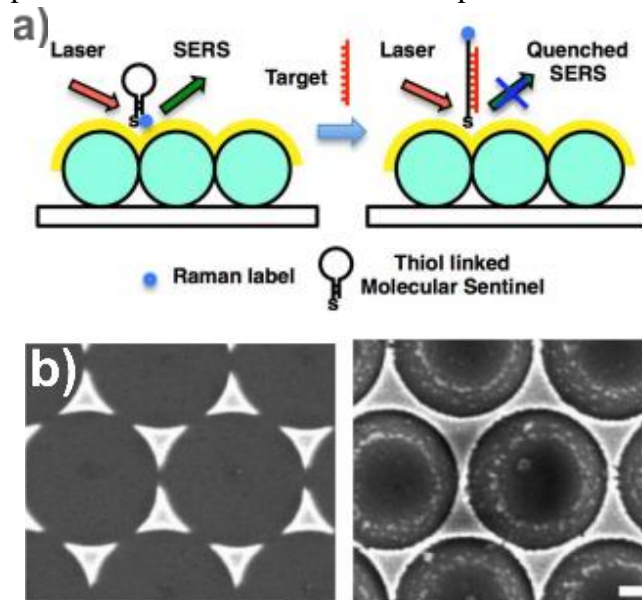


**Figure 3.2** a) Detection scheme for DNA target analysis using a SERS-active substrate (i.e. gold covered PS microsphere array) [180]. b) SEM images of different arrays of Au nanostructures prepared by Au evaporation using a monolayer of PS microspheres [181].

Recently, with the development of microsphere lithography, SERS techniques got a new impulse for further progress. Figure 3.2a shows representative structures of gold nanostructure arrays prepared using a PS microsphere array [180]. Such type of substrate (i.e. metal film over microsphere array) due to its simple fabrication and high enhancement factor, was used in a wide range of chemical and biological sensing applications such as trace or DNA [180] detection. Since 1984 this technique was improved and several new types of arrays were fabricated (e.g. 2D triangle-like (Figure 3.2b) [181], cavities, nanoring, nanotip,

etc.) for detection of environmental pollutants, bacterial pathogens, biomarkers, etc. [163, 182].

### Fine structuring of surfaces

PS microsphere arrays have also been used for structuring substrate surfaces and creating various nanoobjects such as grating, nanopillars, nanocones, nanotips (Figure 3.3), nanostars, nanowires, nanobowls, nanovoids, nanorings and nanocrescents.

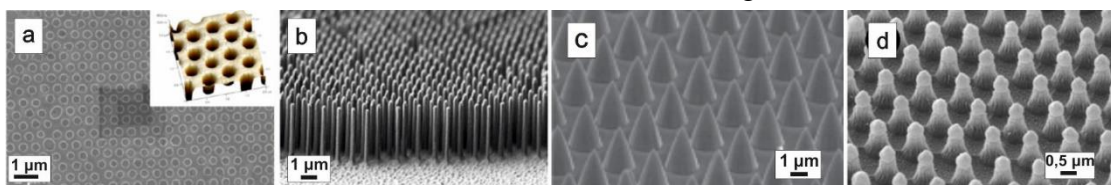


**Figure 3.3** Periodically patterned nanostructures: a) gold nanowell grating [183], b) ordered nanotip array with high aspect ratio [184] c) silicon nanocone arrays [182] and d) nanopillar array for biointerfaces [185].

These structured samples found applications in photonics, biomedical science [185, 186] and other fields. For example, fabricated silicon pillars can be used as stamps for nanoimprint lithography, silicon nanocone arrays mimic the surfaces of natural materials (e.g. leaves of lotus and rice, the eye of moth or wings of cicadas) with superhydrophobic or antireflective properties [182].

### *Selective growth*

The following example demonstrates employing PS microsphere arrays as templates for the growth of patterned structures of graphene (i.e. single layer of carbon atoms in a hexagonal lattice) [187]. The neck width and periodicity of the graphene nanomesh were controlled using reactive ion etching and the initial size of the PS spheres (Figure 3.4). The resulting structure was used as a field-effect transistor exhibiting promising electronic properties featuring high electrical conductivities and on-off ratios of up to 10. The same nanomesh employed as the functional layer in a gas sensor provided high sensitivity to  $\text{NO}_2$  and  $\text{NH}_3$ , significantly higher than its film counterparts [188].

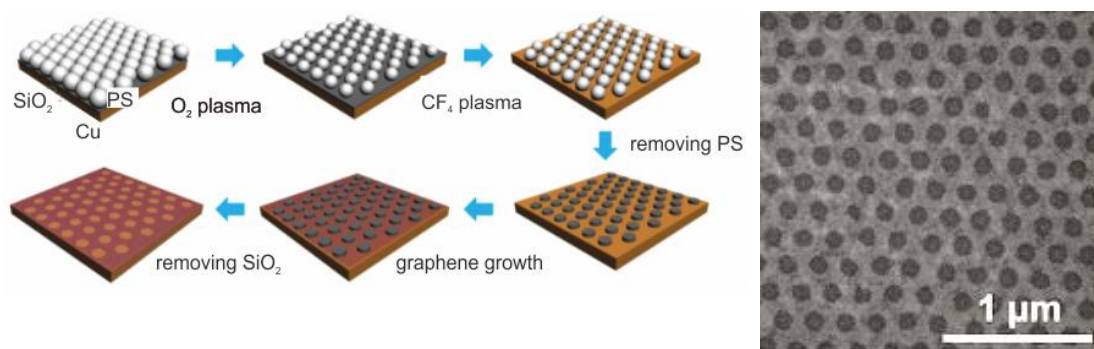


**Figure 3.4** Technological process for the direct growth of graphene nanomesh and corresponding SEM image of graphene nanomesh [187].

# **EXPERIMENTAL PART**

## 4. Processing and analytical techniques

The experimental work of the PhD research was realised at the Joint Laboratory of the Institute of Physics (Department of Optical Materials) of the Czech Academy of Sciences and the Faculty of Civil Engineering (Department of Physics) of the Czech Technical University in Prague. The following chapter describes the main equipment used in the research.

### 4.1 Chemical vapour deposition systems

For diamond growth two different plasma systems were employed:

- **focused microwave plasma** with metallic rotational ellipsoid resonator cavity (P6, Aixtron, Figure 4.1a),
- **pulsed linear antenna microwave plasma** (AK 400, Roth & Rau, Figure 4.1b).

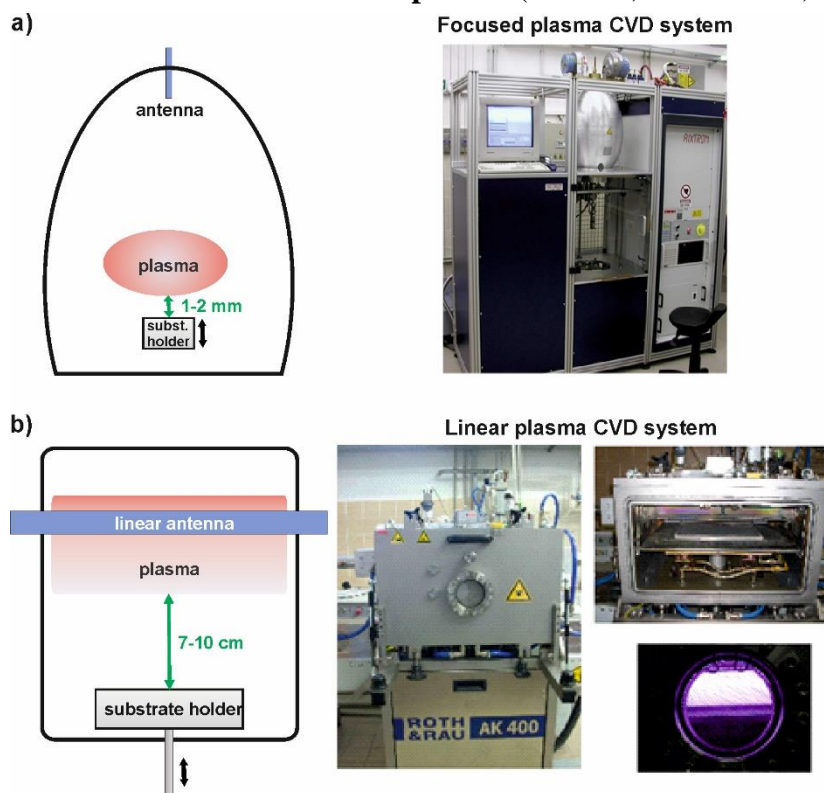


**Figure 4.1** Schematic drawing and a photograph of the a) focused plasma and b) pulsed linear antenna plasma deposition system.

#### 4.1.1 Focused plasma CVD system

The focused microwave plasma CVD system is a representative of a standard ball-type plasma system (so-called ellipsoidal cavity reactor) [189]. It has a removable quartz bell jar placed on the water-cooled substrate holder with vertical movement. The plasma is localised close to the substrate surface at a distance of 1–2 mm. The size of the plasma ball increases with increasing MW power. The effective power is up to 6 kW. In focused MW plasma systems, the microwaves penetrate to the bulk of the plasma, and heat and excite its whole body, which results in a relatively high electron temperature (~ 5–10 eV). The temperature of the gas within the plasma ball can reach ~ 3000 °C [190].

The diamond growth rate in this system can be increased from 0.4 to 10  $\mu\text{m/h}$  by increasing the process pressure from 1500 to 25000 Pa (stable plasma region). Because of the high pressures, the substrate is continuously heated by hot plasma limiting the lowest possible deposition temperature. The substrate temperature typically varies between 370 and 1100 °C, however many substrates are not thermally stable at these temperatures. Another disadvantage of the system is the relatively small deposition area. The homogeneous deposition area is limited by the size of the plasma ball to 5 cm in diameter.

#### 4.1.2 Linear plasma CVD system

The main part of the linear plasma system is based on a commercially available apparatus used for solar cell technology. Some components have been modified in close cooperation with Roth and Rau, AG (Germany).

The system has a large deposition area of about  $20 \times 30 \text{ cm}^2$ , which meets industrial requirements. It combines radiofrequency and microwave plasma, which is one of the main advantages of the system because it offers control over specific plasma parameters [47]. The system employs two MW generators (2.45 GHz, MX4000D, Muegge) working at a pulse-frequency up to 500 Hz and maximum power up to 4.4 kW in pulse mode on each side of the linear conductors located in the quartz tubes. The lowest MW power that can be achieved in the system is 1200 W. Below this value plasma density is extremely low and the plasma becomes unstable and the growth of diamond film is practically impossible. The RF source uses the 13.56 MHz frequency and power up to 600 W to control the energy of ions impinging on the substrate surface. The gas pressure can be varied from 6 to 200 Pa for various gas mixtures. At low pressures (< 10 Pa), the plasma volume expands towards the substrate, and at high pressures (> 100 Pa) it is localised near the quartz tubes [191]. Various deposition parameters change the growth kinetics, for example lowering the process pressure improves the diamond film morphology from nano- to microcrystalline character. Moreover, specific process parameters enable diamond deposition on three-dimensional substrates [90] (see section 6.1) even, even outside the Bachmann phase diagram (Figure 2.6) [192].

Another advantage of the system is the large distance between the high-density plasma and the substrate region (50–100 mm). The surface wave plasma penetrates only a thin layer, the bulk of the plasma is not heated and excited by microwaves, it remains cold and has a low electron temperature ( $< 3$  eV). Thus, the overheating of the substrate from plasma radiation is minimised [133, 193]. This feature allows low-temperature deposition on various temperature-sensitive substrates (e.g. plastics, certain types of glass). The substrate holder can be resistively heated from 250 to 800 °C and moved up/down to control the distance of substrates from the antennas (from 4 to 12 cm).

Besides the diamond CVD deposition, this system was also used for plasma etching PS microspheres. The system offers great control over the size and shape of the microspheres because the self-bias voltage can be controlled independently on other parameters.

## 4.2 Reactive ion plasma etching

Reactive ion etching (RIE) is a dry etching technique combining physical sputtering (ion bombardment) with the chemical reactions of the ions with the sample surface. The main steps involved in the etching process are the formation, adsorption, chemisorption and desorption of reactive species [194]. If the energy of the ions is high enough, they can etch the materials without a chemical reaction. This physical part of the RIE is highly anisotropic (i.e. the etching rate is not equal in all directions). In contrast, chemical etching exhibits an isotropic character (etching rate is the same in both horizontal and vertical directions) [195]. The etching characteristics (such as etching rate, selectivity, surface morphology, isotropy, reproducibility and uniformity) can be calibrated and controlled very precisely with process parameters [194].

For the plasma etching of microspheres and diamond thin films, a capacitively coupled reactive ion etching (CCP-RIE) system (Phantom III, Trion Technology, Figure 4.2) suitable for industrial applications was used.

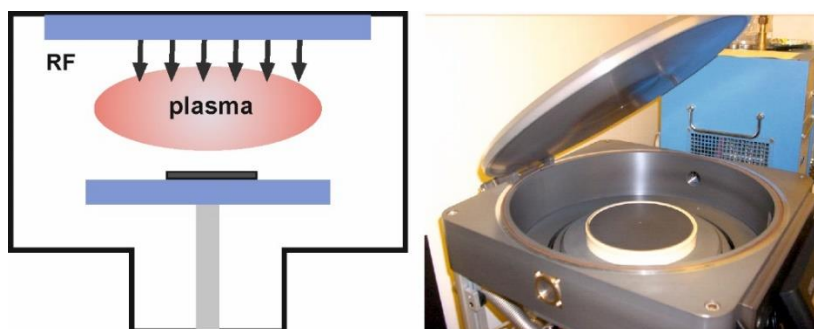


**Figure 4.2 Schematic drawing and a photograph of the CCP-RIE system (Phantom III, Trion Technology).**

The system consists of a vacuum chamber containing two electrodes (15 and 20 cm in diameters). One of them is grounded and the other is driven by a 13.56 MHz RF generator, which generates an oscillating electric field between the two electrodes and creates the etching environment consisting of radicals, ions and electrons. The mean free path of ions is considerably shorter than that of the electrons, which reach the reactor walls and electrodes much faster than the ions. The ions cannot follow the applied field because of their large mass. The electrons, however, are accelerated by an electric field and charge the blocking capacitor negatively. This leads to a negative self-bias voltage ( $-V_{DC}$ ) on the electrode, which repels the electrons and accelerates the positive ions [196]. They arrive at the plasma sheath interface and are then accelerated toward the self-biased electrode (through a maximum potential of  $V_{pp}+V_{DC}$ ), where they bombard the substrate (Figure 4.3) [197]. Sheath regions are formed automatically near the electrodes to keep the plasma semi-neutral (nearly equal number of electrons and ions) [175].

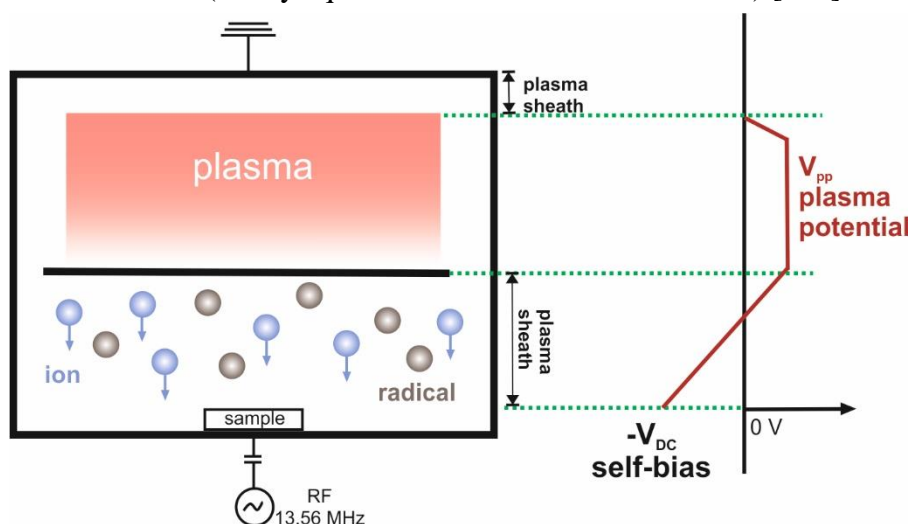


**Figure 4.3 Schematic illustration of self-bias voltage in the CCP-RIE reactor.**

The bias voltage is determined by process parameters (pressure, gas mixture and RF power). The main limitation of the CCP-RIE system is that the ion density is directly related to the ion energy (RF bias). Consequently, high RF power must be employed to obtain high ion densities. The power range is 0–600 W. Available gas sources are: oxygen, tetrafluoromethane, argon, sulfur hexafluoride, nitrogen, etc.

### 4.3 Spin-coating

Spin-coating (Figure 4.4) is an equipment used for depositing uniform thin films ranging from a few nanometres to a few microns in thickness to flat substrates [198]. Advantages of this technique include simplicity, repeatability, safety, mass production and low cost. It is used intensively in a wide variety of industries and technology sectors (e.g. photolithography, semiconductor industry, organic electronics, nanotechnology, etc.).



A typical process involves depositing a small puddle of fluid onto the centre of a substrate. Then the substrate is rotated at high speed (e.g. up to 10 000 rpm) in order to spread the fluid by centrifugal force. Rotation is continued while the fluid spins off the edges of the substrate until the desired thickness of the film is achieved. The applied solvent is usually volatile and simultaneously evaporates [200]. Despite the process simplicity, there are several major factors affecting the coating process. Among these are spin speed, acceleration, spinning duration, etc.



**Figure 4.4 Spin-coating instrument (WS-650Sz Lite Single Wafer Spin coater) [199].**

#### 4.4 Employed procedures

Standard procedures that were repeatedly used for the experiments:

##### *Substrate cleaning*

The preparation process started with a thorough cleaning of the substrates (e.g. silicon, quartz) to remove surface contamination (organic residue, dust particles). The substrates were cleaned in ultrasonic baths of isopropyl alcohol and deionised water for 10 and 5 min, respectively, then dried in nitrogen flow. Ultrasonic agitation is a powerful technique for the removal of contamination without causing surface damage to the substrates.

##### *Substrate nucleation*

In experiments where substrate nucleation was employed, substrates were ultrasonically seeded for 40 min in a dispersion of water and diamond nanoparticles (NanoAmando Aqueous Colloid: Dispersed Buckydiamond with a median diamond grain size of  $4.8 \pm 0.6$  nm) before the diamond deposition process [73].

#### 4.5 Material characterisation and other equipment

The analytical techniques used for sample characterisation and processing equipment employed in experiments are listed below.

##### *Analytical techniques*

The initial analysis of the samples was carried out using **scanning electron microscopy** (SEM; eLine writer, Raith GmbH and MAIA3 Tescan Ltd.). It provides high-resolution images on large areas ( $\sim \text{mm}^2$ ) relatively quickly. Top view and angle



view two-dimensional SEM images provided information about the surface morphology of i) diamond films (homogeneity, crystal size, etc.) and ii) other structures (e.g. surface coverage after spin-coating, diameter and shape of spheres after plasma etching, defect formation, etc.).

Selected regions of samples were further investigated using **atomic force microscopy** (AFM, Dimension 3100, Veeco and Ntegra, NT-MDT). AFM provides a three-dimensional topographic profile. Consequently it is able to give more information about the samples. However, it has a low scan rate and can scan small areas only. For our experiments, AFM measurements were used for the evaluation of the surface roughness of the diamond films, shape and height measurements of diamond grains, etching depth evaluation, determining the shape of the polystyrene spheres after plasma etching, etc.

Diamond-based structures were also studied using **Raman spectroscopy**, which is the most extensively used analytical tool for the characterization of the quality and composition of carbon materials [197]. It is a non-destructive technique that reveals both the diamond and non-diamond phases (graphite, amorphous carbon) of carbon [51]. For our experiments we used a Renishaw In Via Reflex Raman spectrometer with an excitation wavelength of 325 and 442 nm.

The etching depth and profile of the diamond films was determined using a profilometer (Dektak 150 Surface Profiler, Veeco).

The thickness of the diamond film was determined from i) cross-sectional SEM images or ii) by evaluating the interference fringes in the reflectance spectra measured in the VIS and NIR region using the commercial optical thin film modelling software FilmWizard.

***Other processing equipment:***

- home-made evaporation system – metal mask preparation for plasma etching
- oxygen plasma systems (CCP-RIE; Tesla 214 VT; Femto, Diener)
  - for cleaning the organic contamination from silicon substrates
  - for improving the surface wettability of the substrates

***Supporting equipment:***

- ultrasound bath – for substrate cleaning, seeding with diamond nanoparticles, microsphere dispersion preparation
- magnetic stirrer/baking plate – for polymer preparation
- scale, flow-box system, etc.

***Software:***

- OriginPro – for data analysis and graphing
- Atlas –for visualisation and analysis of SEM data
- Gwyddion – for visualisation and analysis of AFM data
- CorelDraw – for image processing
- ImageJ – for image processing

## 5. Microsphere lithography

### 5.1 Introduction

Microsphere lithography (MSL) stands out as a highly parallel, powerful and versatile alternative lithographic technique for producing periodic nanostructures in a controlled fashion. It can generate well-ordered 1D–3D periodic sub-micrometre and nanoscale structures from a variety of materials on many substrate types [146]. MSL is not comparable in flexibility, precision and spatial resolution with conventional lithographic techniques, it wins out however in simplicity, cost and speed, especially on larger areas (from a few mm<sup>2</sup> to several cm<sup>2</sup>) [201, 202].

In order to obtain tailor-made structures, i.e. achieve a different feature size, shape, periodicity, arrangement, etc., deliberate fabrication schemes can be devised [29]. The MSL method consists of variations of the following stages: i) mask preparation (deposition of microsphere array on the substrate), ii) mask alteration (plasma etching), iii) metal/polymer deposition (e.g. Ti, Au, Ag, PDMS, etc.) onto the modified sphere array and iv) sphere removal from the substrate (lift-off).

In this chapter, a conceptual overview of MSL is provided. This chapter is not aimed at developing a general recipe but instead aims to show the most important factors and parameters affecting the preparation of ordered structures.

### 5.2 Mask preparation using spin-coating

First, mask preparation using spin-coating is presented. The purpose is to achieve large area monolayers on various types of substrates, screen out the most influential factors and to minimise structural defects. Then, post-assembly processes are demonstrated (plasma etching and lift-off).

The first steps of MSL are schematically represented in Figure 5.1. The mask preparation includes the following stages: colloidal dispersion preparation, substrate pre-treatment and spin-coating.



**Figure 5.1** A schematic drawing of the steps involved in the mask preparation and modification.

Spin-coating is a widely used, simple, cheap, convenient, fast and highly reproducible one-side coating technique. The coating process comprises four stages: deposition, spin-up, spin-off and evaporation of the solvent (Figure 5.2) [203]. The last three stages overlap.

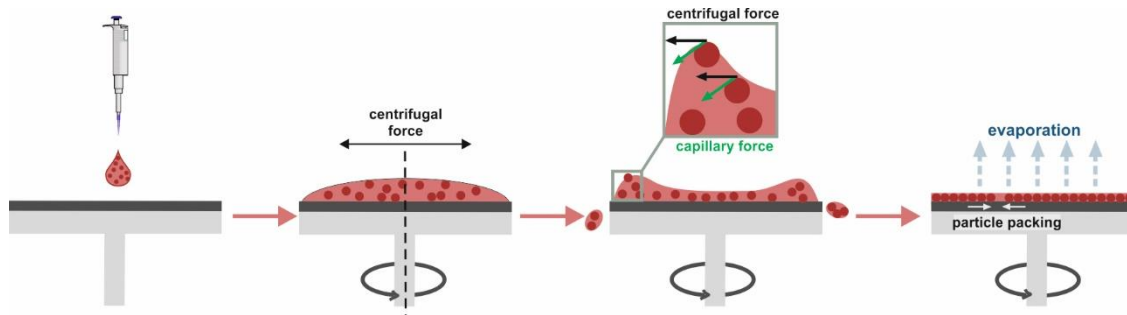


**Figure 5.2 Schematic illustration of the four stages of the spin-coating process.**

First, a drop ( $20 \pm 5 \mu\text{l}$  for  $1 \times 1 \text{ cm}^2$  samples) of the dispersion is pipetted onto a stationary substrate, which is fixed to a rotating substrate holder by vacuum. The dispersion forms a fluid layer in a concave shape. Next, the substrate is accelerated to a desired rotational speed (i.e. spin-up stage) around the axis perpendicular to the substrate holder. The dispersion covers the whole substrate surface and the fluid layer shape changes to concave. The subsequent reduction in fluid layer thickness is driven by the centrifugal force, viscous shear force and evaporation of the dispersant [161]. By evaporation, the dispersion becomes more viscous, which stops the horizontal flow of the liquid (i.e. spin-off stage). When the liquid becomes almost as thin as the diameter of the spheres, the spheres self-assemble due to the strong immersion capillary attraction, which pushes particles into ordered arrangements [204].

The quality (uniformity and compactness) of the spin-coated colloidal crystals is affected by numerous factors [156, 205], which can be divided into four main groups:

- **substrate properties:** material, size, roughness, wettability, etc.;
- **dispersion properties:** diameter and size distribution of the microspheres, particle weight fraction, concentration, presence of surfactant, deposited volume, dispersant mixture, dispersant volatility and viscosity, etc.;
- **spin-coating process parameters:** number of steps [206], rotation speed, acceleration, duration, drop method (“drop while spinning” and “drop before spinning”), etc. [150, 207];
- **ambient environment:** pressure, temperature, humidity, etc.

The final structure is a result of complex non-equilibrium processes whose behaviours are explained by several different theoretical models [203, 208, 209]. However, most of the literature on spin-coating is experimentally based. Researchers develop their empirical recipes, but the described protocols are very different, often contradictory and imprecise, which makes the optimisation process challenging [149].

Plenty of experimental work has been done for this thesis to obtain good quality colloidal crystals, which was essential for the subsequent fabrication steps. However, it

is difficult to carry out a detailed study due to the large number of aforementioned interrelated variables [210]. In the following sections, selected experimental observations and results are summarised and discussed.

### 5.2.1 Substrate properties

Spin-coating works well on clean and chemically homogeneous substrates with low surface roughness. The preparation process starts with a thorough cleaning of the substrate (e.g. silicon, quartz) to remove suspended dust particles and other surface contamination to prevent defect formation (e.g. pinholes, comet streaks). A typical cleaning process involves ultrasonic cleaning in acetone and isopropyl alcohol and drying with nitrogen flow. The cleaned substrates are highly hydrophobic, thus the dispersion cannot cover the whole substrate surface evenly (Figure 5.3a). They require pre-treatment to alter their surface chemistry. The substrates are treated with oxygen plasma to render their surfaces hydrophilic (Figure 5.3b), which is an indispensable prerequisite to obtain homogeneous monolayers [211]. The wettability of the substrate surface is verified using contact angle measurements.

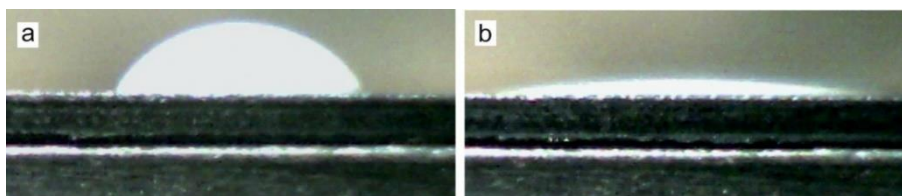


**Figure 5.3 Influence of oxygen-treatment on the PS dispersion wettability of Si substrates: a) non-treated hydrophobic and b) oxygen-treated hydrophilic substrate.**

The wettability of the substrates can also be changed using chemical treatments, i.e. sonication in a hydrophilic solution (e.g. sulphuric acid, diodecyclo-sodiumsulfate solution [212], mixture of ammonium hydroxide, hydrogen peroxide and ultrapure water, [207]).

### 5.2.2 Colloidal dispersion

After the substrate cleaning step, the colloidal dispersion is prepared, which consists of spherical solid particles in a liquid. Before the spin-coating, it is necessary to sonicate the as-received dispersion in an ultrasonic bath for a few minutes to ensure the spheres are homogeneously dispersed. Dispersions, which do not contain surfactant or salt have to be sonicated much longer (~ 1 hour). The temperature should be monitored to ensure that the microspheres are not overheated.

The choice of the liquid substance is a critical factor in the preparation of the colloidal dispersion [213]. Most often mixed solvent (e.g. water-based dispersion diluted with alcohol) is used as the dispersion medium for the spin-coating process. The addition of alcohol (e.g. methanol or ethanol) enhances both the wettability of the surface and the evaporation rate of the dispersion. The alcoholic components evaporate relatively quickly

and give uniform coverage, while the other components (e.g. water) evaporate relatively slowly and gives enough time for the spheres to self-assemble before the substrate is completely dry. A pure alcohol dispersion is not able to create ordered monolayers because of its relatively high evaporation rate, i.e. the spheres have no time to reach their lowest energy configuration before the surface is dried.

Next, the dilution ratio of the colloidal dispersion with alcohol is determined. Achieving a compact monolayer across the whole surface of the substrate is essential for the MSL process. If the mixture is too dilute (i.e. low PS concentration) only sparse coverage and loosely packed islands were observed, i.e. there is an insufficient quantity of spheres in the dispersion to cover the whole sample surface (Figure 5.4a-b). When highly concentrated mixture is used, only multilayers occur, independently of the spin-coating process parameters. It should be mentioned, that multilayers exhibit not only hcp ordering but also square packing (Figure 5.4d), which is a metastable transition state to the hexagonal ordering.

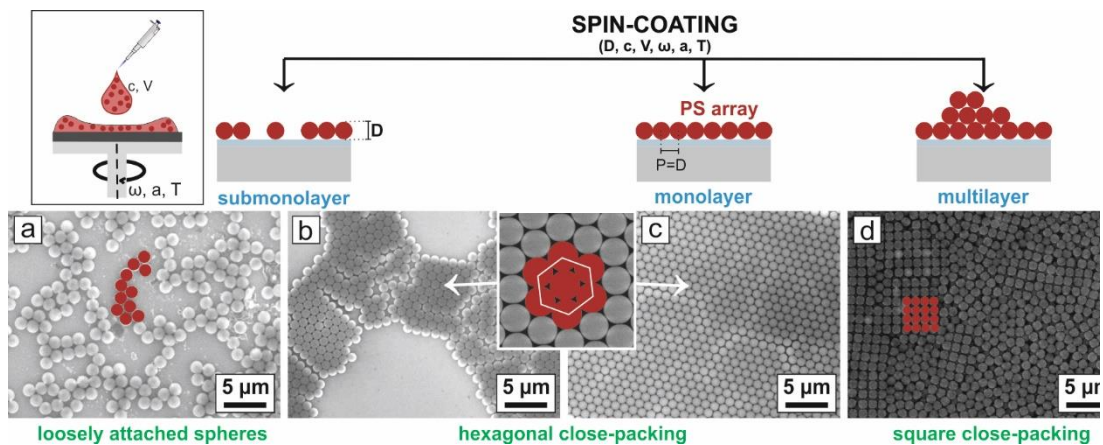


**Figure 5.4 Schematic illustration of possible array configurations after the spin-coating process.**

Surfactant (i.e. amphiphilic non-ionic Triton X-100) addition to the dispersion is also frequently reported [166, 214]. It enhances the wetting of the substrate by decreasing the surface tension of the solvent mixture [215]. The hydrophobic part (hydrocarbon group) of the surfactant adsorbs on the PS spheres and the hydrophilic part (polyethylene oxide group) extends into the aqueous phase leading to the steric stabilisation of the dispersion.

### 5.2.3 Critical process parameters of spin-coating

After determining the appropriate concentration of the dispersion, the various spin-coating process parameters are studied (e.g. number of steps, speed, acceleration, duration) in order to obtain a uniform monolayer.

In most cases, multistep (two or three) processes are employed. The purpose of the first step (100–400 rpm for < 10 s) is to spread the dispersion evenly on the substrate

surface, which improves the uniformity of the final monolayer. It is important to ensure that the dispersion on the substrate surface is free of air bubbles because they cause inhomogeneities in the final layer. Next, the substrate is accelerated to a higher speed (1000–3000 rpm for 30–120 s). During the second step, the centrifugal force, capillary force and solvent evaporation organise the spheres into well-ordered arrays. When the second step spin rate is too high (i.e. high centrifugal force), the solvent evaporates very quickly. Furthermore, the dispersion spins away from the centre, leaving the central part less wet. The ordering starts from the centre and extends towards the exterior, so in this case, the PS microspheres form monolayers, but with partial coverage only – voids and lots of defects emerge [216]. Similarly, if the second step is too short, the PS spheres do not have enough time to migrate on the substrate and achieve close-packing, which results in loosely packed monolayers (the inter-particle capillary forces are weakened). During the third step, excess material (i.e. second and subsequent layers) is spun away from the substrate. If the final rotation speed is too low (centrifugal force not large enough) multilayers remain on the surface. However, if the final spin speed is too high, empty areas with no spheres (voids) occur in the monolayer. The proper process parameters (spin rate, duration, acceleration, etc.) depend on the material and diameter of the spheres. For example, spheres with a smaller diameter move faster, for that reason higher rotation speed must be applied. Polystyrene spheres with diameters ranging from 200 nm to 1.5  $\mu\text{m}$  are the most commonly reported particles used for MSL. In the case of even smaller spheres, stronger Brownian motion and other particle interactions make the mask preparation even more difficult.

## 5.2.4 Analysis of the self-assembled monolayers

### *Optical analysis*

After the spin-coating process, the first indication of good quality monolayers is the angle-dependent iridescent colour generated from the Bragg diffraction of the visible light on the periodically arranged structure. Figure

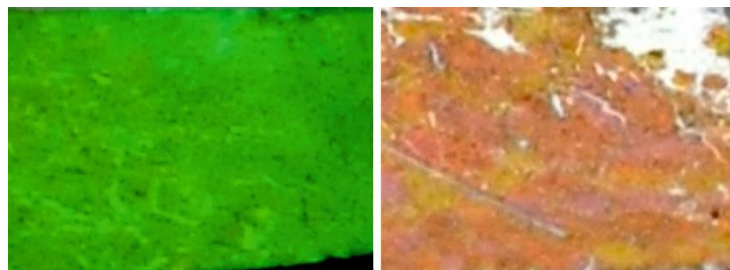


**Figure 5.5 Photographs of samples coated by PS microspheres with different diameters.**

5.5 shows photographs of samples coated by spheres with different diameters. The final film is quite uniform. In case of rotationally asymmetric substrates, the edges of the substrate are patchy. Another undesirable phenomenon is the so-called “coffee-ring” effect, as a consequence of difference in evaporation rate across the droplet mainly on hydrophobic surfaces [217, 218].

### ***SEM analysis***

The deposited monolayers of the PS microspheres were characterised using optical and scanning electron microscopy. Several pictures were taken on each sample at various positions (e.g. centre, edges). The coverage and the quality of the assembly can be determined using Fourier transformations (FT) of the SEM images. In-situ studies are more challenging due to the rapidly rotating sample and high evaporation rates. Real-time observation of colloidal crystallisation is possible using stroboscopic microscopy, i.e. optostrobometer [204]. The majority of studies are performed ex-situ.

A typical SEM image of a monolayer of PS spheres on a large area is presented in Figure 5.4c and Figure 5.6a. The corresponding FT image (Figure 5.6b) created with open-source image-processing software ImageJ clearly confirms the periodical ordering of the spheres.

### **5.2.5 Defect formation**

Due to the limitations in synthesis and deposition of microspheres, defects among them are inevitable. The prepared arrays contain different kinds of arrangement defects [19, 167], including:

- **point defects:** missing spheres, difference in sphere sizes, spheres resting on top of the array;
- **line defects:** grain boundaries, slip dislocations, cracks;
- **area defects:** multilayers, voids, disordered regions;
- **3D aggregates** already present in the dispersion.

The common disadvantage of the spin-coating method is that besides the required uniform monolayers, uncovered areas (voids), submonolayers (randomly and locally ordered) and double layers or even multiple layers (hcp, square close-packed) can also occur on the same substrate (Figure 5.6c-d).

Under proper preparation conditions, uniform self-assembled microsphere monolayers can be obtained over large areas. However, even with optimal concentration and spin-coating parameters other types of defects occur in some areas. Strictly speaking, the obtained monolayer is not perfect. Figure 5.6c-d show defect-rich domains representing typical and most commonly occurring defects in monolayers (e.g. dislocations, smaller, bigger spheres). There are several reasons for the formation of such defects.

The quality of the colloidal crystals fabricated using self-assembly is mostly dependent on the spheres size and shape distribution. The spheres have to be uniform in size, shape, composition and properties (both surface and bulk). Point defects (such as vacancies) are related to the varying sizes of the spheres [219]. Spheres with diameters larger or smaller than the average diameter of the population disrupt the hcp ordering and induce defects in the array. These defect precursors were marked by blue circles in Figure 5.6e-f.



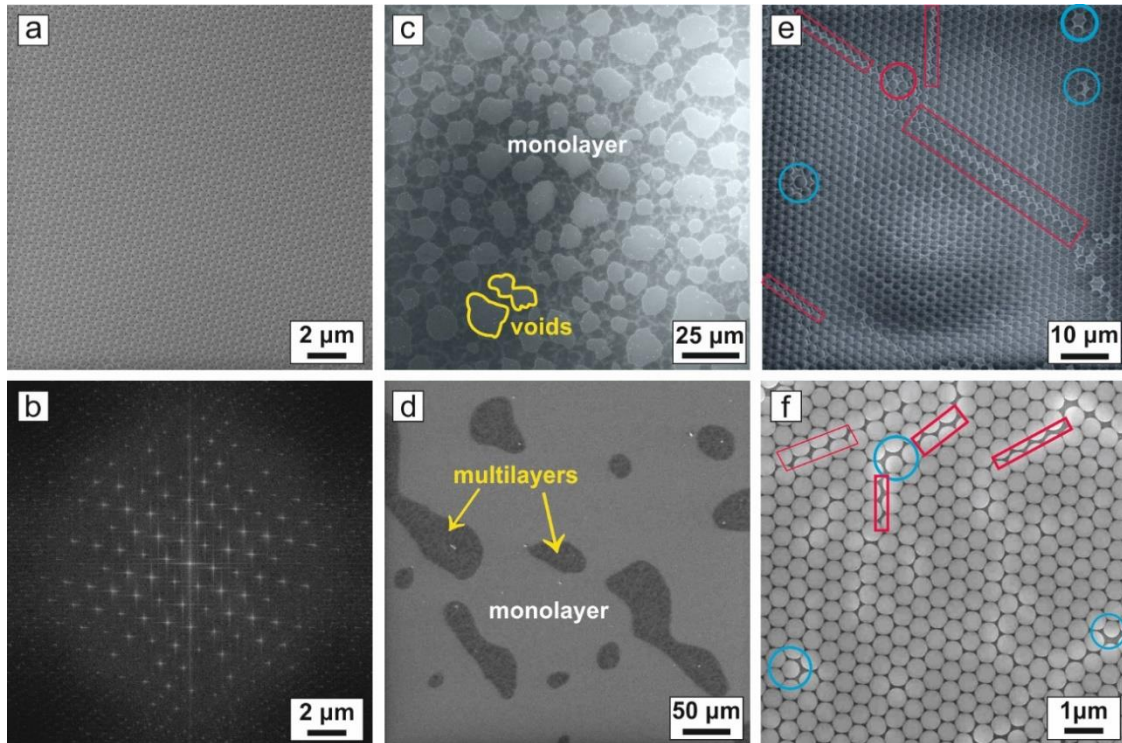


**Figure 5.6** SEM image of monolayer with hcp ordering and b) corresponding FT image. Substrates predominantly covered by monolayer, but c) voids, d) multilayers e) f) defects also occur.

Size deviation is below 5% from most suppliers but becomes worse for smaller spheres. High polydispersity essentially limits the area of defect-free domains. Typically reported defect-free domain sizes are in the 10–200  $\mu\text{m}^2$  range [149]. The acceptable degree of disorder of the colloidal crystals depends on the specific application. For example, fairly well-packed (e.g. high degree of order, low variation in the periodicity) spheres are important to create PhC and less critical in certain other cases, such as photonic glass fabrication.

### 5.3 Post-assembly processing

Modification of the colloidal crystal masks can be achieved using various post-treatment techniques. It is possible to manipulate single particles (e.g. using AFM) or alter the entire lattice using annealing, plasma etching, ion-milling, metal/polymer deposition, lift-off, etc. [202].

#### 5.3.1 Plasma etching

Non-close-packed colloidal crystals (i.e. spheres arranged in a periodic lattice and spaced out equally) are obtained using plasma etching of the initial close-packed array [156, 207, 220–223]. The initial diameter of the spheres defines the periodicity (i.e. the distance between the centre of the spheres), which remains preserved after the plasma

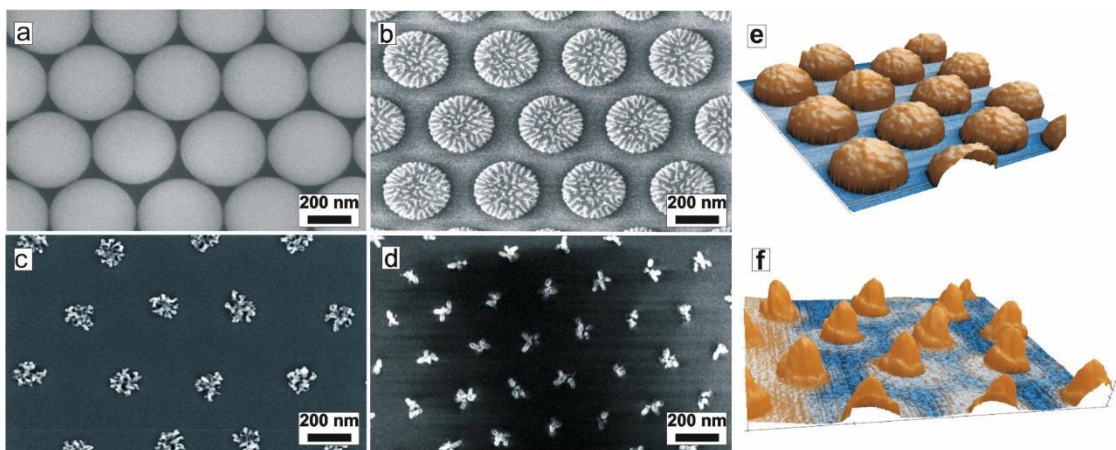


treatment [224]. The etching process can either be isotropic or have an additional anisotropic etch component, depending on the plasma system and parameters.

For our experiments two different reactive ion etching systems were employed: i) capacitively coupled radiofrequency plasma (CCP-RIE) and ii) linear antenna plasma system (see section 4.1), which combines RF and MW plasma system (henceforth dual plasma system). The desired diameter and shape of the spheres as well as the intersphere distance were precisely adjusted via the choice of plasma system and etching process parameters (duration, power, gas mixture, pressure). Both systems have a large processing area (circle with a diameter of 20 cm and  $20 \times 30 \text{ cm}^2$  rectangle, for CCP-RIE and linear plasma system, respectively), i.e. they allow processing many samples at the same time, which is very time efficient.

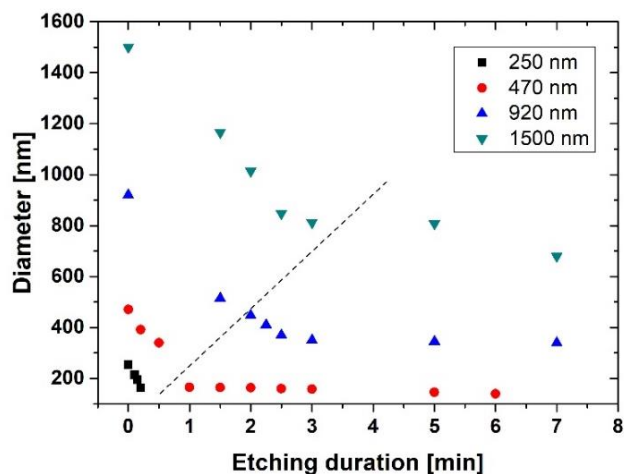
### 5.3.1.1 Etching in the CCP-RIE system

Figure 5.7 shows the effect of deposition duration (from 30 s to 7 min) in the case of pure oxygen plasma, at 12 Pa of pressure and 100 W of RF power. The plasma treatment led to homogeneous etching over the whole sample area and reduced the diameter of the spheres in a non-linear fashion. The plasma treatment can be divided into two regions, where the breakpoint is between 45 s and 1 min (Figure 5.8). For etching durations up to 30 s, the shape of the PS spheres remained sphere-like (Figure 5.7e), while for longer etching durations ( $> 1 \text{ min}$ ) the sphere patterns collapsed, and inhomogeneous PS residues were observed. These structures will be referred to as pyramid-like structures according to their appearance on AFM images (Figure 5.7f). While the etching rate seems to be linear until 1 min of etching duration, for longer etching durations nearly no change was observed (only a slight decrease in diameter).



**Figure 5.7** Top view SEM images of plasma treated arrays of polystyrene spheres on Si substrates after CCP-RIE treatment for a) 0 s, b) 30 s, c) 3 min and d) 7 min ( $\text{O}_2:50 \text{ sccm}$ , 100 W, 12 Pa). AFM images ( $1.5 \times 1.5 \mu\text{m}^2$ ) of e) sphere-like and f) pyramid-like structures [142].

The influence of the etching duration was also studied on microspheres with different sizes, i.e. PS250–PS1500 (Figure 5.8). These experiments confirmed that the diameter of the spheres exhibits a non-linear dependence on the etching duration. In these cases, the breaking point between sphere-like and pyramid-like structures is shifted from shorter (20–30 s) to longer (3 min) durations as the size of the microspheres increases from smaller (PS250) to larger (PS1500) [175].



**Figure 5.8** Sphere diameter as a function of etching duration for PS microspheres with different diameters from 250 nm to 1500 nm (etching parameters:  $O_2$ :50 sccm, 100 W, 12 Pa).

Etching in the CCP-RIE system has highly anisotropic character. From AFM and angle view SEM images (Figure 5.9a-b) it is clearly noticeable, that the plasma etching not only reduced the sphere diameter but also transformed the isotropic microspheres into anisotropic ones, while their position remained unchanged. The emergence of surface roughening with extended etching duration is a result of polymer degradation during plasma etching associated with surface cross-linking [225]. The bottom profiles of the spheres indicate that the etching predominantly starts from the top. The contact area remains circular, as long the shape of the spheres is quasispherical (Figure 5.9d).

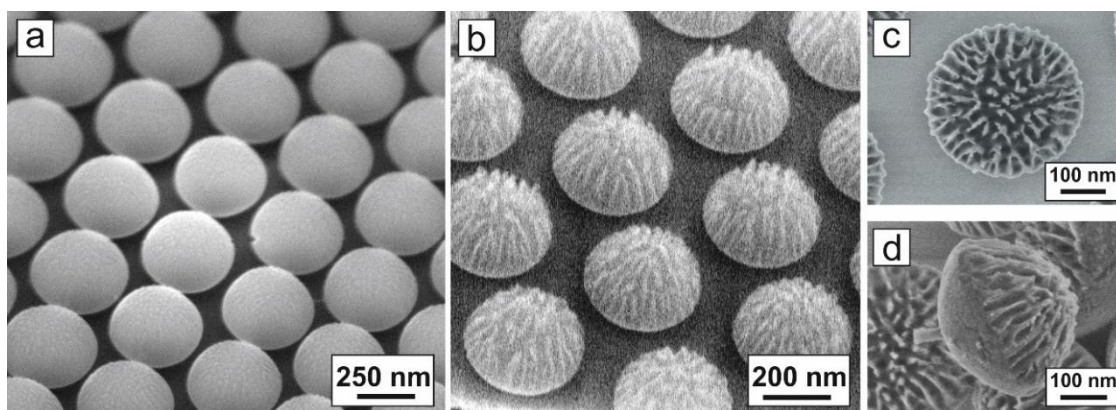


**Figure 5.9** Representative SEM images of PS spheres after oxygen etching in the CCP-RIE system.

Figure 5.10 shows the influence of RF power and  $CF_4$ : $O_2$  ratio on the structuring of the PS microsphere (PS 470 nm) array for 30 s of etching duration. Increasing the power from 60 to 100 W enhanced the etching rates (Figure 5.11) for each ratio of  $CF_4$ : $O_2$ . This fact indicates more extensive ion bombardment of the samples which was also confirmed by the decrease in bias voltage from -18 to -57 V. For example, plasma

treatment in a pure oxygen plasma at 100 W reduced the PS diameter to 340 nm (in comparison to plasma treatment at 60 W, which was 364 nm).

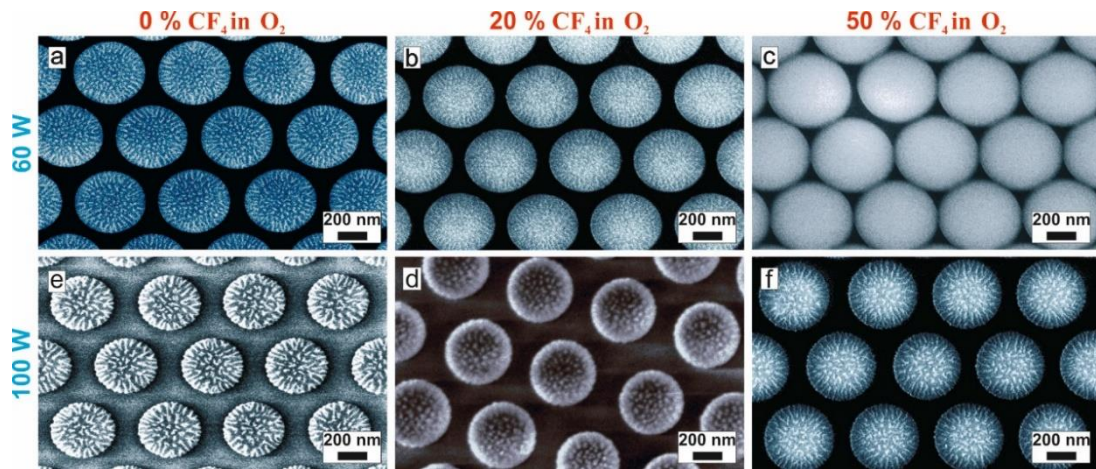


**Figure 5.10 a) - f) Top view SEM images of polystyrene sphere arrays plasma treated using CCP-RIE at different powers (60 and 100 W) and  $\text{CF}_4:\text{O}_2$  ratios [142].**

Most commonly an oxygen-containing gas mixture is utilised for the reactive ion etching of PS spheres. Their hydrocarbon chains are decomposed during the oxygen etching into  $\text{CO}_2$  and water. Furthermore, oxygen does not etch the Si or  $\text{SiO}_2$  substrates. To alleviate the surface roughening, Ar or  $\text{CF}_4$  can be added to the gas mixture. In this case, physical sputtering occurs rather than chemical etching [156, 226], and the etching rate is much lower compared to pure-oxygen etching (Figure 5.11).

On the one hand, the addition of  $\text{CF}_4$  into the  $\text{O}_2$  atmosphere makes the etching process less aggressive, and the surface of the PS microspheres remains much smoother as can be seen on Figure 5.10 (at higher  $\text{CF}_4$  content). On the other hand,  $\text{CF}_4$  reacts with the Si substrate. Random speckle patterns (substrate damage) appeared between the spheres (Figure 5.12), which is undesired for several applications. This could be caused either by the etching of the substrate surface (the interaction between the fluorine-based plasma and the Si substrate produces volatile species such as  $\text{SiF}_4$ ,  $\text{SiF}_3$  which acts as an etching agent for the Si substrate) [194] or by the deposition of polymers from the PS microspheres [175].

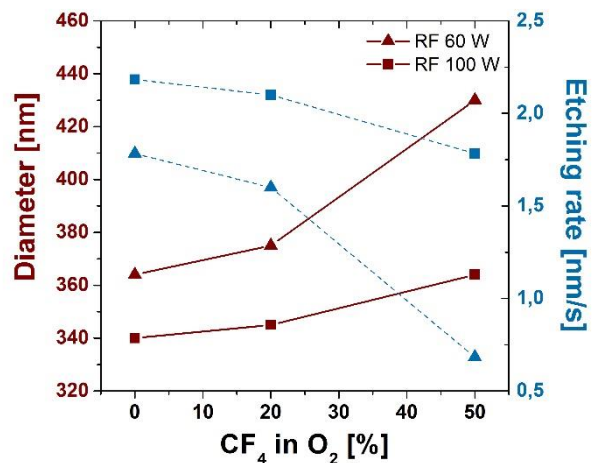


**Figure 5.11 Diameter of microspheres (solid red lines) and attributed etching rates (blue dotted lines) as a function of  $\text{CF}_4:\text{O}_2$  ratio at 60 W (triangles) and 100 W (squares) [142]**



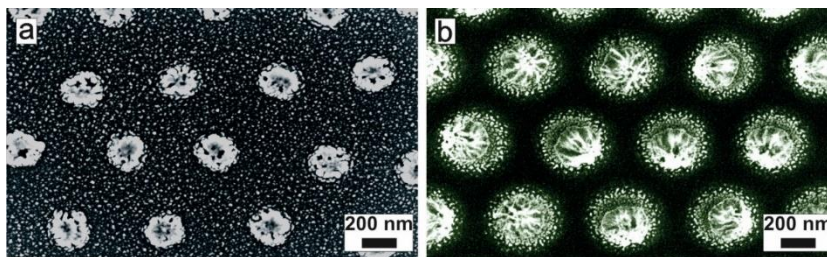


**Figure 5.12** Top view SEM images of microsphere array (PS470) illustrating the “damaged” (etched) surface of the substrate (etching parameters: RF power 100 W, pressure 12 Pa a) 20 % CF<sub>4</sub> in O<sub>2</sub> for 3 min, b) 50 % CF<sub>4</sub> in O<sub>2</sub> for 60 s.

### *Isotropic etching*

For many applications, there is a high demand for smooth sphere-like structures (isotropic etching). The experiments above have shown that the process parameters need to be chosen carefully – in particular, the process duration needs to be short because of the soft material and thin monolayer. The preparation of well-controlled circular patterns is not a simple task in the CCP-RIE system because it is highly anisotropic and longer etching durations result in pyramid-like structures (Figure 5.7f). The formation of smooth PS microspheres is possible only when short etching times are used, or in cases where the initial diameter of PS microspheres needs to be decreased only by a minimal value. To provide an excellent isotropic etching process, the etching rate must be equal in all directions, and the ratio of physical etching to chemical etching must be decreased. The disruptive effect of the high energy ion bombardment can be reduced by decreasing the self-bias voltage (absolute value).

The degree of anisotropy and surface roughening also depends on the temperature and the used plasma system. In general, smoother surfaces can be achieved at lower temperatures (room temperature or less) or using an inductively coupled plasma system equipped with He-cooling [227]. Etching in inductively coupled plasma systems offers more isotropic etching and better size and shape control due to the lower etching rates [175, 225].

Unfortunately, the temperature in our CCP-RIE system cannot be controlled. Moreover, the self-bias voltage also cannot be controlled independently (it is a function of RF power, pressure and gas mixture), therefore we studied the PS microsphere plasma treatment in our dual plasma system. This system combines both RF and MW plasma and allows independent control of the bias voltage, which is responsible for the surface bombardment, and since the plasma is far from the substrate, the heat flow is minimised. The results obtained using the dual plasma system are summarised in the following section.

#### **5.3.1.2 Etching in the dual plasma system**

Several sets of experiments were carried out, a select few of them are shown in Figure 5.13. These tilted SEM images reveal that with various etching parameters

different shapes can be achieved, e.g. spherical, oblate spheroid (resembling biconvex microlenses) and ball-and-stick (spherical connected with “necks”, labelled as b-and-s) structures. The position and surface smoothness of the PS particles are preserved.

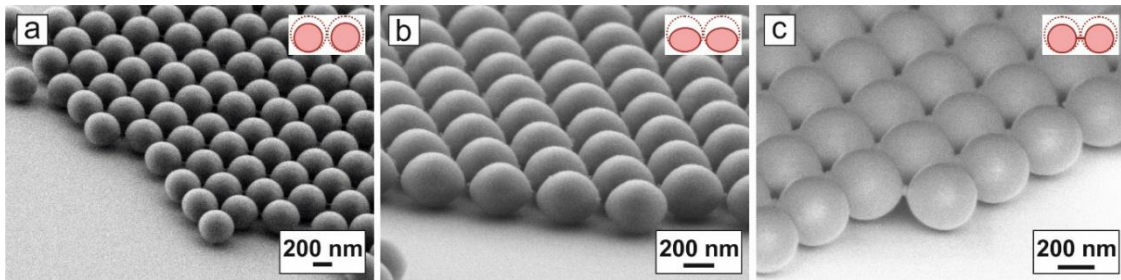


**Figure 5.13** Representative angle view SEM images of PS spheres with different shapes: a) spherical, b) oblate spheroid and c) ball-and-stick structures obtained after plasma etching in dual plasma system.

Figure 5.14 shows representative top view SEM images of arrays etched with RF plasma only and in dual mode (RF + MW). In dual plasma mode, the microspheres were shrunk from their initial diameter of 470 to 416 nm after etching for 1 min, with further etching (3 min) the diameter was reduced to 345 nm. The sphere-like structures were connected to each other with thin necks creating a net even after 3 min of plasma treatment. The length and width of the necks can be influenced by etching parameters [228]. The plasma etches the spheres gently, and their contacts are slowly converted to necks, which are gradually thinning until they break and disappear at a critical sphere spacing [221]. In our case, the net-like structure is not observed for etching times longer than 3.5 min (not shown here). Rapid shrinkage of the spheres does not result in neck formation.

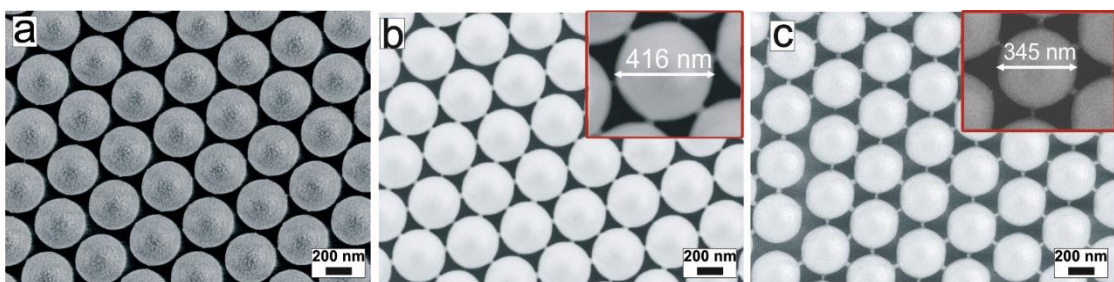


**Figure 5.14** Top view SEM images of polystyrene microsphere arrays on Si substrates plasma treated a) with RF power only (300 W, 7 V) and combination of RF (600 W) and MW ( $2 \times 1200$  W) power for b) 1 min and c) 3 min (10 Pa, pure O<sub>2</sub> atmosphere) [142].

We suppose that the formation of the net-like structure is probably due to the cold plasma character and lower plasma densities near the sample surface in the dual plasma system in comparison to CCP-RIE [229]. It was observed that even at 10 Pa of pressure the effective electron temperature ( $T_e$ ) is strongly dependent on the distance from the microwave antennas, and this influence further increased with increasing pressure (i.e. for the substrates localized at  $z = 70$  mm it means a drop of plasma density by three orders of magnitude in the range of 10 to 150 Pa) [229]. In close vicinity to the antenna (16 mm),

the  $T_e$  reaches 4.5 eV and drops by 2 eV with distance (at 10 Pa). This dependence of the electron temperature and electron density on distance in similar surface-wave plasma systems was also observed by Tsugawa et al. [193]. Secondly, the formation of net-like structures in the dual plasma system can also be caused by lower self-bias voltages. In the dual plasma system, two independent MW and RF power supplies were applied. MW plasma is responsible for enhancing the ion density, while RF plasma accelerates the ions (and electrons) towards the sample. In the case of liner plasma, the bias does not exceed -15 V even at 600 W of RF power, while in the case of CCP-RIE it is -18 V and -57 V for 60 W and 100 W of RF power, respectively [175].

We conclude that the etching process in the low temperature dual plasma system is more controllable than in the CCP-RIE system. It also allows isotropic shrinkage of the spheres to the proper size without surface roughening. Furthermore, it can be applied even to smaller spheres (< 500 nm) due to the lower etching rate.

It should be noted, that small neck formation can also be observed after thermal annealing (Figure 5.15b), when the point contacts between particles are converted to area contacts, presumably as a consequence of softening of the polymer [230]. Thermal annealing (in the case of PS above the glass transition temperature:  $T_g = 110\text{--}120$  °C) also mechanically improves the adhesion between the spheres and substrate surface [212].

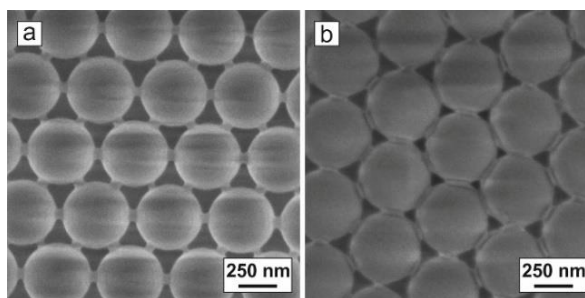


**Figure 5.15 SEM images of ball-and-stick structures a) after plasma etching in dual plasma system, b) after thermal annealing.**

### 5.3.2 Evaporation and lift-off

Nanostructured noble metal (e.g. gold, silver, platinum, palladium) arrays have attracted a lot of attention as SERS active substrates, plasmonic devices and metamaterials due to their strong interactions with the external electromagnetic field [231–233]. The simplest nanostructures (i.e. triangular and spot structures) that can be created using MSL arrays are shown in Figure 5.16. The fabrication process requires only three steps. The unmodified mono- and bilayers are coated with a thin gold layer. The metal fills in areas between the spheres. Then, the desired nanostructures are achieved by removing the PS mask with the use of standard adhesion tape or by the dissolution of PS in an appropriate solvent (e.g. tetrahydrofuran [234], dichloromethane, toluene [167]) by mild sonication. It should be noted, that strong or long vibration of the ultrasonic bath can cause damage to fragile samples.

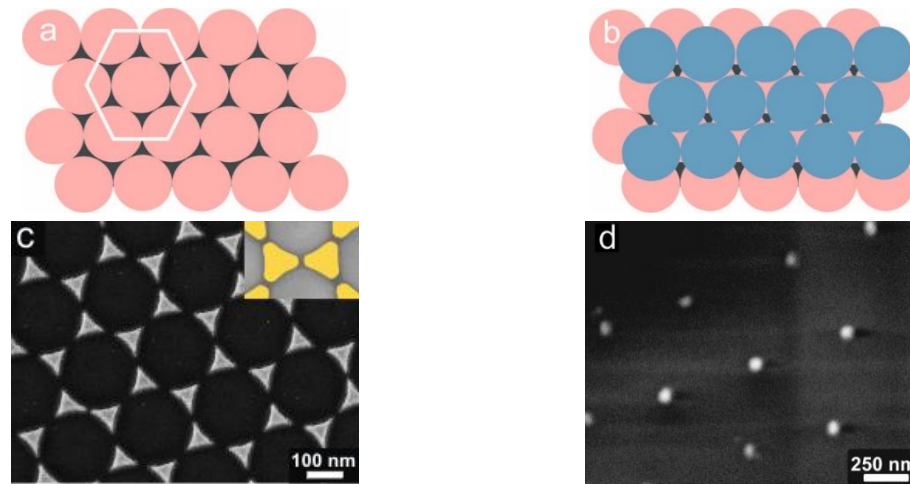


**Figure 5.16** Schematic illustration of a) monolayer and b) bilayer microsphere masks and c), d) SEM images of structures obtained after metal deposition and PS spheres lift-off.

Other type of plasmonic nanoantenna arrays were successfully created by combining self-assembly of polystyrene microspheres, plasma etching and metal sputter coating [235]. Gold “nanocorals” (i.e. corrugated non-close-packed anisotropic structures) were created by gold sputtering on array composed of structures shown on Figure 5.9c-d. B-and-s structures with very long necks (Figure 5.14c) were used as a mask to obtain a hexagonal array of gold bow-tie nanoantennas with controllable gap sizes, by sputtering gold layer onto it. Lift-off the spheres resulted in a planar truncated triangle nanoantenna array. These structures were created in cooperation with Faculty of Nuclear Sciences and Physical Engineering (Czech Technical University in Prague). They were successfully tested as SERS-active substrates for  $\rho$ -aminothiophenol (at submicromolar concentrations). For details see Ref. [235].

Figure 5.17 shows other examples of arrays with nonspherical building blocks. In these cases, spin-coating of spheres, plasma modification of the PS mono- and double layers (with hcp or square arrangement) and Au evaporation were applied. For multilayers (3D colloidal crystals) the upper layers act as a shadow mask for the etching of the lower layer [144, 236].

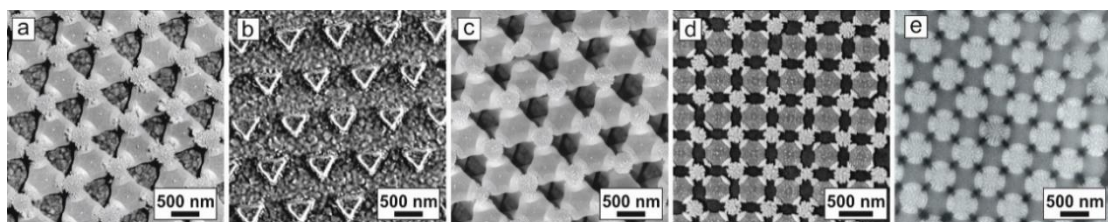


**Figure 5.17** SEM images of multiple kinds of patterns fabricated on nanocrystalline diamond films. Plasma etched monolayer of PS spheres a) after Au evaporation, b) after lift-off the PS spheres. Plasma etched PS mono/multilayers after Au evaporation with c) hcp and d), e) square lattice.



With angle-resolved evaporation, it is possible to achieve even more complex nanostructures (rings, crescents, split-rings, asymmetric double split-rings, dimers, etc.) [144, 237, 238].

### 5.3.3 Surface roughness

Spin-coating is a common method to produce uniform monolayers on smooth surfaces. In Chapter 8 is demonstrated that is not limited to smooth substrates only. Employment of spin-coating on rough polycrystalline diamond films is described (for diamond-based photonic crystal fabrication). Examples of plasma etched PS monolayers on diamond thin films with various grain size and surface roughness are demonstrated in Figure 5.18.

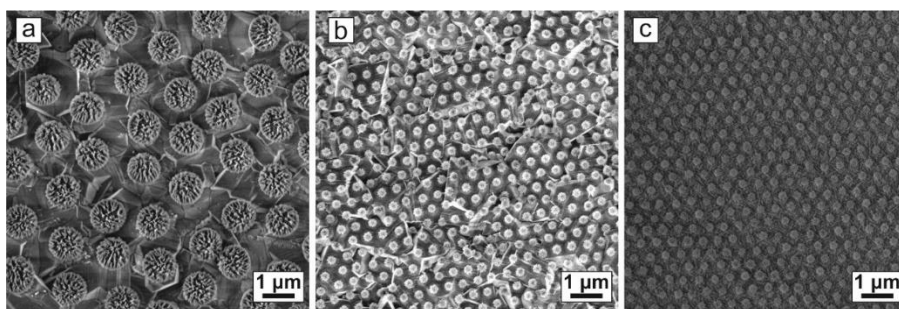


**Figure 5.18 Plasma etched PS spheres on a), b) microcrystalline and c) nanocrystalline diamond film.**

In these cases, two main conditions have to be fulfilled to obtain good mask quality. First, the diamond film must be uniform and homogeneous, since individual diamond grains which are significantly larger than the average grain size lead to local defect formation within the PS monolayer mask. Second, it is essential to choose the proper sphere diameter according to the surface roughness of the diamond films [30].

## 5.4 Conclusion

MSL has been demonstrated to be an efficient, inexpensive, relatively fast and simple way to create a large variety of ordered arrays. It does not require the time-consuming and expensive conventional lithographic masks. Instead of these, it employs self-assembled colloidal crystals as masks and various nanofabrication techniques. Spin-coating was demonstrated as a simple way to create large area monolayers on various substrates (Si, diamond) with various surface roughness (nano- and microcrystalline diamond films). The mask modification was achieved using plasma etching. The degree of anisotropy and surface roughening depended on the plasma system. After anisotropic etching in the CCP-RIE system the PS particles deviate from spherical shape, they were transferred into ellipsoids and surface roughening also occurred. Dual antenna plasma system allowed finer control of the spheres, nearly isotropic etching and low surface roughening was achieved.



## 6. Diamond nucleation and growth

### 6.1 Spontaneous nucleation and growth

This section focuses on the spontaneous nucleation of diamond films in a linear plasma CVD system. Our goal was to get complex information about the early stages of diamond growth on non-treated (i.e. absence of pre-existing diamond seeds) silicon substrates in two orientations: perpendicular (vertical samples) and parallel (horizontal samples) to the linear antennas (plasma sources). The study of deposition on samples in two orientations is especially important for coating complex 3D substrates.

#### 6.1.1 Experimental

##### 6.1.1.1 Sample preparation and deposition parameters

Two kinds of substrates were used: i) non-treated (i.e. clean) and ii) seeded (labelled as “nucleated”) mirror-polished (surface roughness < 1 nm) silicon <100> substrate.

First, all substrates were ultrasonically cleaned. Careful manipulation and thorough cleaning of substrates were indispensable because any mechanical scratches and contamination on the substrate surface could act as energetically favourable nucleation centres. Substrates cleaned using the aforementioned procedure were labelled as “non-treated” (depending on deposition parameters further named as L5, L10, M10 and H10, see Table 6.1). Substrates labelled as “nucleated” (i.e. samples nL5, nL10, nM10 and nH10) were ultrasonically seeded immediately after the cleaning procedure.

The diamond deposition was carried out in a linear plasma CVD system. The Si substrates were placed in the deposition chamber in both vertical (labelled as “VerS”) and horizontal (labelled as “HorS”) positions (Figure 6.1). The sample size was  $1 \times 1 \text{ cm}^2$  for horizontally and  $1 \times 3 \text{ cm}^2$  for vertically oriented substrates. The moveable graphite

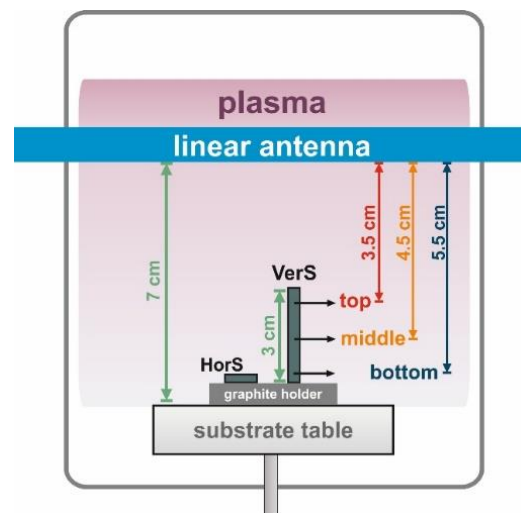


**Figure 6.1** Schematic illustration of the substrate placement in the linear antenna CVD system [81].

water-cooled substrate table was set to a constant distance (7 cm) from the antennas. The vertically oriented substrates were fixed in a graphite holder fabricated for such purposes. The process parameters used for the diamond CVD were as follows: gas pressure of 10 Pa, MW power of 1800 W at each antenna and substrate temperature of  $\sim 450 \pm 20$  °C. The other process parameters (deposition duration, CH<sub>4</sub>/CO<sub>2</sub>/H<sub>2</sub> gas mixture composition) are summarised in Table 6.1.

The deposition durations of 5 and 10 h were chosen based on the following observations: after 5 h of deposition, a sufficient amount of grains was present on the samples to evaluate their surface coverage. The second deposition duration (i.e. 10 h), was chosen in order to obtain high surface coverage but also clearly isolated grains, i.e. to evaluate the samples before they formed a coalesced fully closed diamond film.

**Table 6.1 Summary of sample labelling and characteristic process parameters [81].**

Sample name	Process duration [h]	Ratio of C:O:H atoms	Hydrogen content
L5, nL5*	5	5:8:44	low (L)
L10, nL10	10		
M10, nM10	10	5:8:64	medium (M)
H10, nH10	10	5:8:84	high (H)

\*prefix “n” means “nucleated” (i.e. ultrasonically seeded) samples

### 6.1.1.2 Analytical techniques

Samples were characterised using SEM, AFM and Raman spectroscopy. Vertically oriented samples were measured at three different positions (labelled as “top”, “middle” and “bottom”). The top, middle and bottom measurement positions on the substrate surface were located 3.5, 4.5 and 5.5 cm from the antennas, respectively (Figure 6.1). The film thickness of the seeded samples was determined from cross-sectional SEM images. Statistical analysis (diameter of diamond grains, surface coverage and nucleation density) of the non-treated samples was performed from low magnification (20 kx) SEM images using image processing and analysis software (Atlas, Tescan, Ltd.). For the sake of simplicity, grains were approximated by circles. The planar surface coverage was defined as the ratio of the area covered by diamond grains to the investigated area (expressed in %). The nucleation density was calculated by counting the number of resolved grains in a given area and dividing by this area (expressed in cm<sup>-2</sup>). This calculation method was adequate for our experiments because the grains were easily distinguishable from each other [14].

## 6.1.2 Results

### 6.1.2.1 Spontaneous nucleation on non-treated substrates

Representative top view SEM images of vertically (rows 1–3) and horizontally (row 4) oriented non-treated Si samples after diamond growth at different deposition

parameters are summarised in Figure 6.2 (the insets show higher magnification images). These SEM images demonstrate that deposition occurred on samples in both orientations. The formed grains have “cauliflower-like” character (no emerging faceted crystallites), and on the vertical samples, their average size decreases in the downward direction as the measured position (i.e. top, middle and bottom) gets farther from the plasma source. It can be stated, that the spontaneous grain formation and the following growth process is determined by the distance from the antennas (with increasing distance from the antennas lower plasma densities and temperatures are supposed) [239]. This effect is discernible for all samples independently of the deposition parameters (Figure 6.2, columns 1–4).

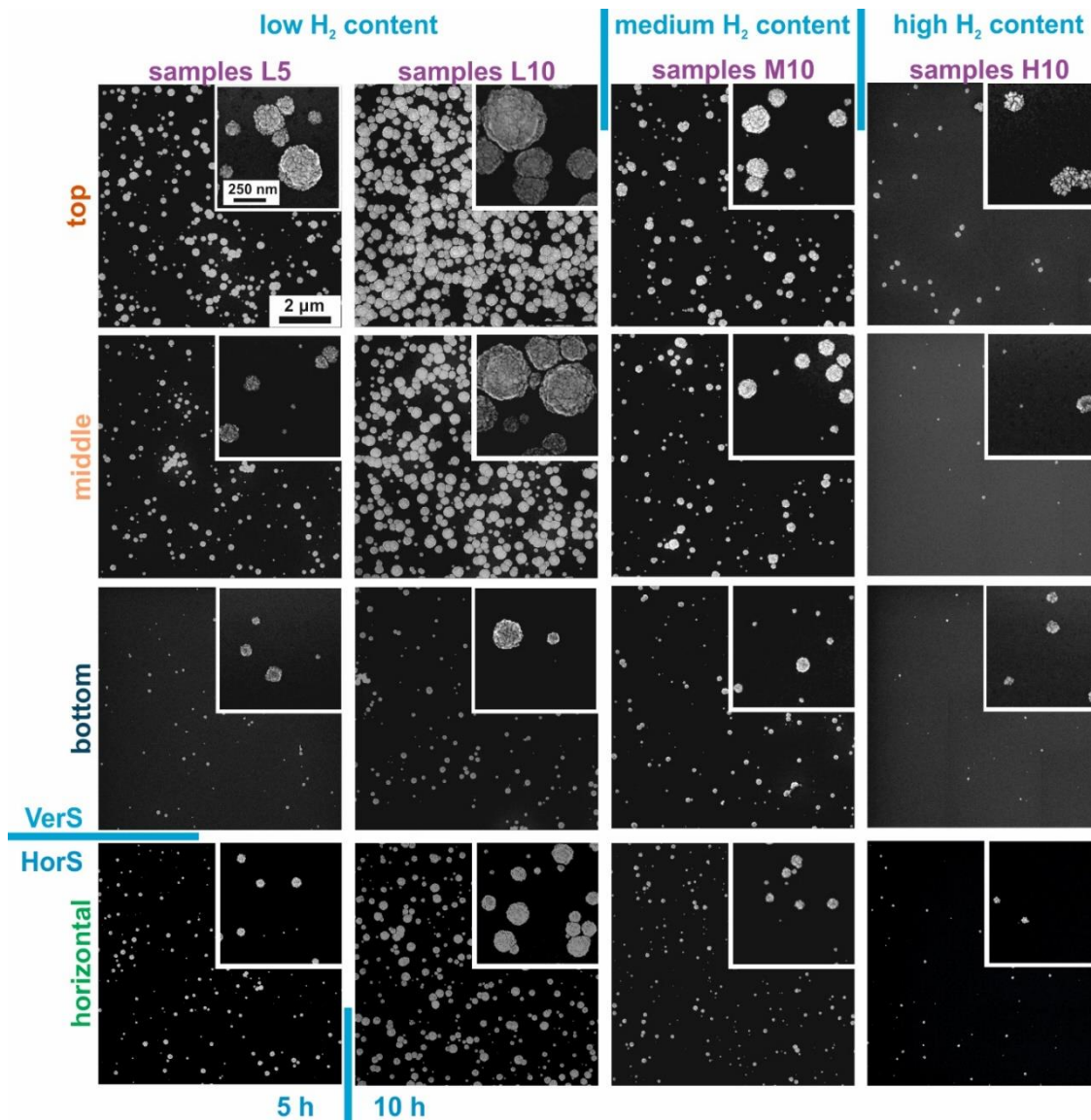


**Figure 6.2** Top view SEM images of the vertically (VerS, rows 1–3) and horizontally (HorS, row 4) oriented non-treated Si substrates after the diamond CVD. First column: low H content, 5 h (sample L5); second column: low H content, 10 h (sample L10); third column: medium H content, 10 h (sample M10); fourth column: high H content, 10 h (sample H10) [81].

As the grains get smaller, the surface coverage decreases, too. For example, the surface coverage of sample L5 (VerS) decreases in the downward direction from 12% to 0.5% (Figure 6.3a). This trend was also observed for the nucleation density. At the top of the sample, the nucleation density was  $4 \times 10^8 \text{ cm}^{-2}$ , while, at the sparsely covered bottom part the nucleation density dropped to  $7 \times 10^7 \text{ cm}^{-2}$  (Figure 6.3b).

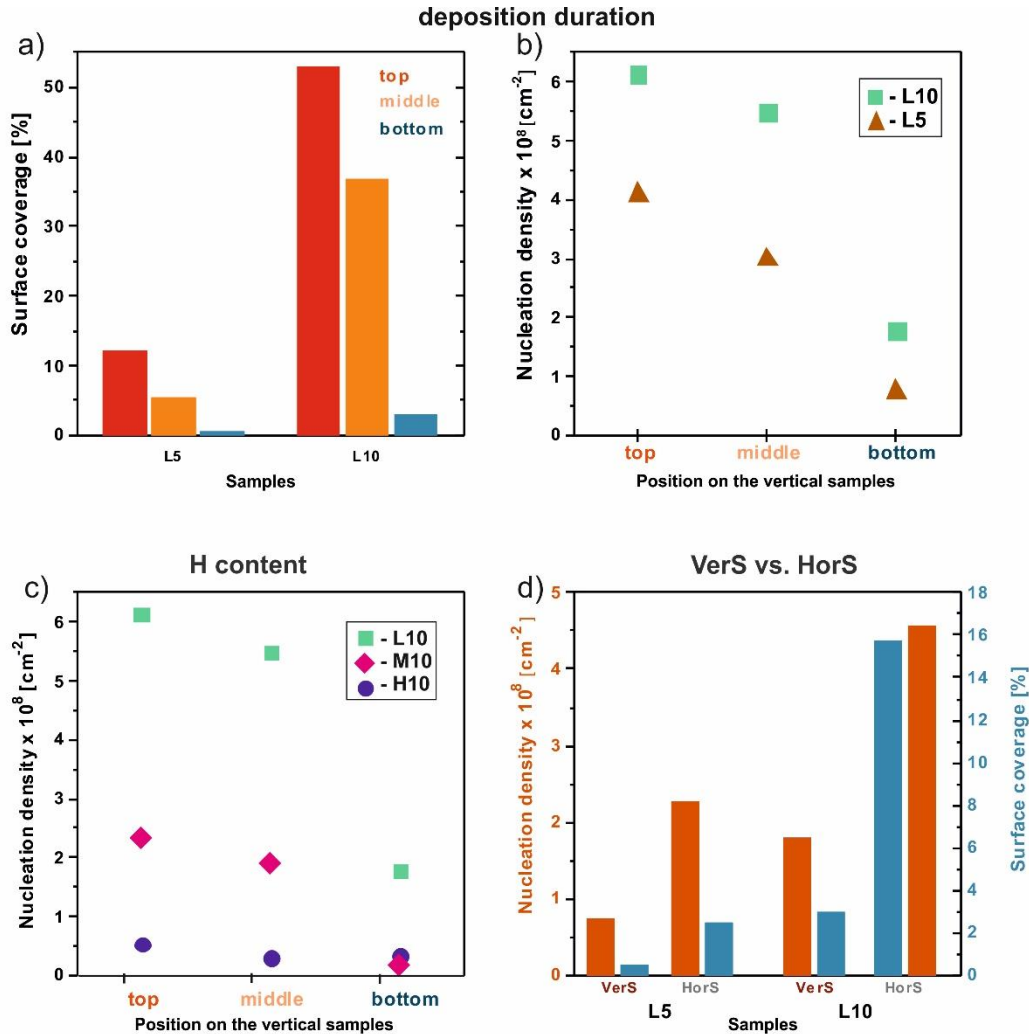


**Figure 6.3** Dependence of a) surface coverage and b) nucleation density on deposition duration (L5 and L10, VerS). c) Dependence of nucleation density on gas mixture (L10, M10, H10) (3 positions on VerS), d) Dependence of nucleation density and surface coverage on sample orientation (VerS vs HorS) at the bottom position [81].

Next, as the deposition duration increased from 5 to 10 h (sample L10), the size of the grains and the surface coverage increased significantly (Figure 6.3a). At the top of L10, the highest surface coverage (53%) and the highest nucleation density ( $N_d \sim 6 \times 10^8 \text{ cm}^{-2}$ ) among all samples and positions were found (Figure 6.3b). As it was expected, in the downward direction not only the number of grains but also their size decreased. Consequently, the bottom of the sample remained a region with poor surface coverage (3%) (Figure 6.3a). The effect of gas composition on the spontaneous nucleation is summarised in Figure 6.3c. The nucleation density and surface coverage decreases with

increasing hydrogen content. It is known that hydrogen-rich plasma suppresses diamond nucleation because the etching effect dominates over the growth process. In the case of sample H10 (VerS) the number and size of grains diminished, the small ones were completely etched away and the surface coverage was reduced to 1.2% (top) and 0.1% (bottom). As a result, the nucleation densities decreased by an order of magnitude, from  $6 \times 10^8 \text{ cm}^{-2}$  (L10 top) to  $5 \times 10^7 \text{ cm}^{-2}$  (H10 top). In general, for all gas compositions, the nucleation density monotonically decreases from the top to the bottom position for each individual sample. A further interesting result was that the properties, such as grain size, surface coverage and nucleation density of HorS (located in the bottom position) were not identical with the bottom position of VerS (Figure 6.3d). The deposited features on HorS are more similar to the middle position of VerS (i.e. position situated 1 cm above HorS). This finding should be attributed to effects such as temperature gradient in the z-direction, different mobilities of growth species on the VerS and HorS surfaces, local gas flow, etc. Similar observations were made on the seeded (pre-treated) samples (section 6.1.2.2).

Figure 6.4 shows AFM analyses of vertically oriented samples grown at low hydrogen content for 5 and 10 h. Local width and height size maxima of formed features (clusters) are plotted in Figure 6.4a.

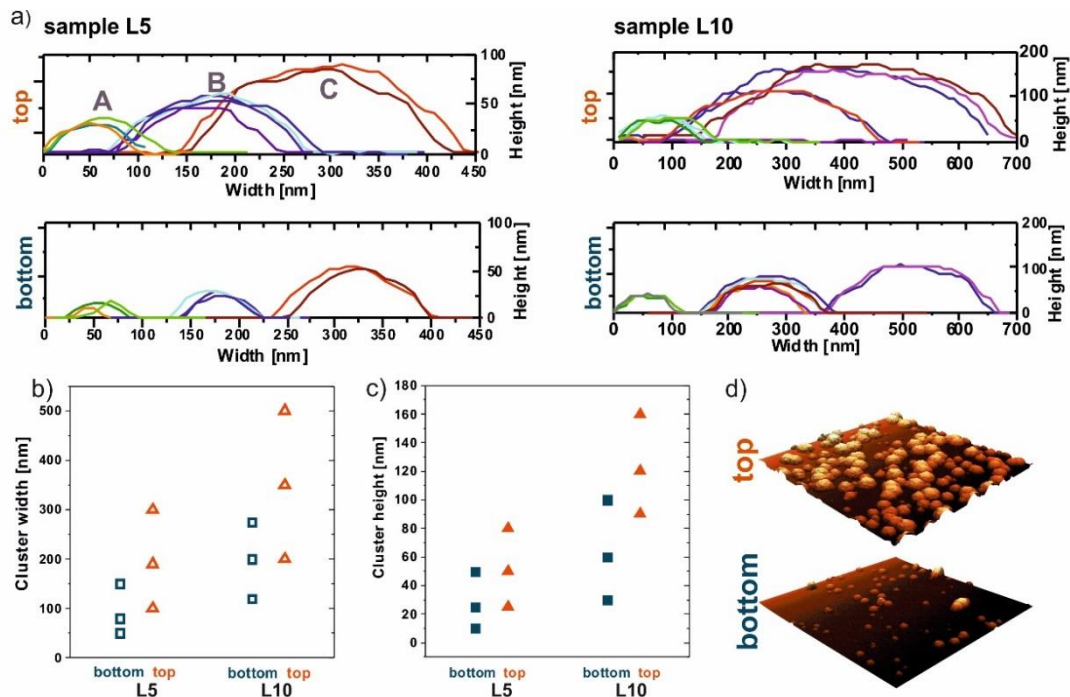


**Figure 6.4** AFM analyses of vertically oriented samples grown at low hydrogen content for 5 and 10 h. a) Width and height size distributions of formed features (clusters) for samples L5 and L10 evaluated at top and bottom positions. Averaged local maxima of b) widths and c) heights of features (clusters) formed for samples L5 and L10 evaluated at top and bottom positions. d) Representative AFM image of sample L5 ( $5 \times 5 \mu\text{m}^2$ ) [81].



As it can be seen, the size (width and height) distributions reveal three different maxima. For example, the sample L5 at the top position contains three maxima - group A: width 100 nm, height 25 nm; group B: width 200 nm, height 50 nm; group C: width 300 nm, height 80 nm. For better comparison, the extracted averaged width/height maxima are summarized in Figure 6.4b-c, which clearly confirms the polymodal distribution for each sample and position. Moreover, these data indicate that the lateral growth rate seems to be almost 3–4 times higher than the vertical one, independently of the measurement position. For illustration, the 3D surface topography of sample L5 measured at the top and bottom positions is shown in Figure 6.4d. The polymodal distribution appeared at varied gas compositions and sample orientations (HorS). It was most apparent for samples L5 and L10. For higher H content (samples M10, H10) this phenomenon was hardly observable because only very small clusters appeared after the CVD process (the etching of nuclei dominated over the growth process).

### 6.1.2.2 Diamond deposition on ultrasonically seeded substrates

Simultaneously with the experiments described above, the same study was performed on the nucleated (seeded) substrates

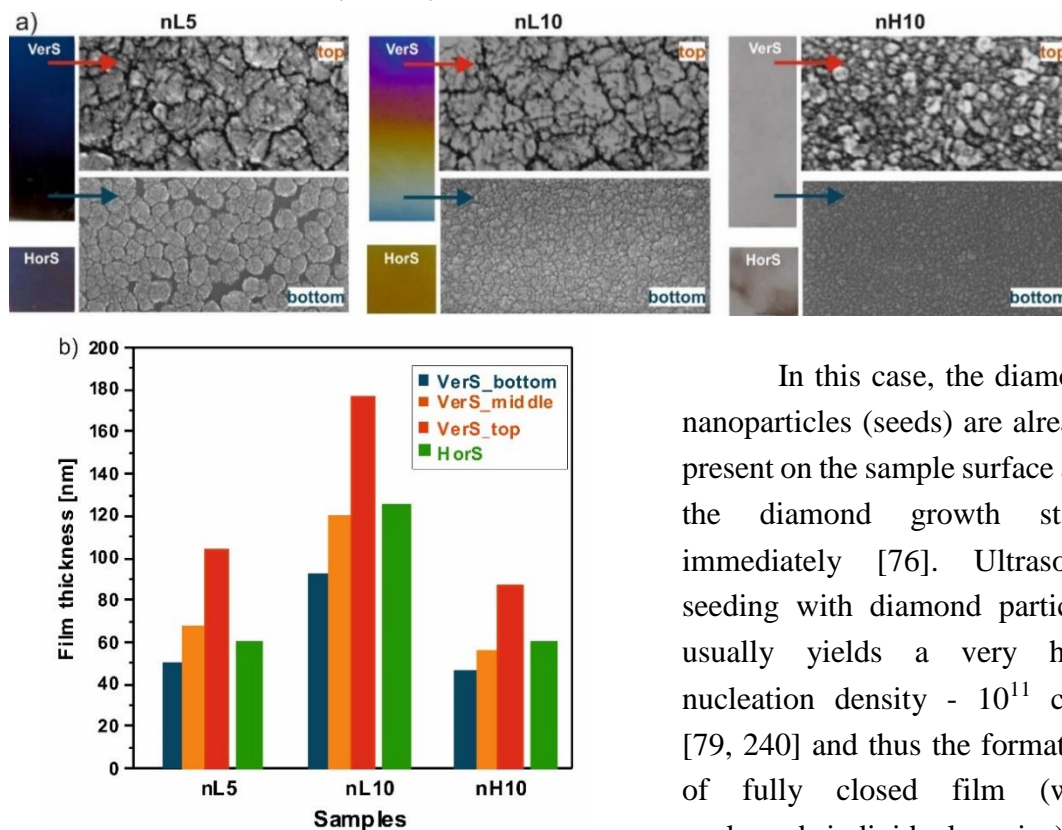


**Figure 6.5 a) Optical images of the samples, and SEM images taken at the top and bottom positions of vertically oriented nucleated samples, grown at different durations (nL5 and nL10) and gas compositions (nL10 and nH10) and b) corresponding film thicknesses [81].**

In this case, the diamond nanoparticles (seeds) are already present on the sample surface and the diamond growth starts immediately [76]. Ultrasonic seeding with diamond particles usually yields a very high nucleation density -  $10^{11} \text{ cm}^{-2}$  [79, 240] and thus the formation of fully closed film (with coalesced individual grains) is much faster in comparison to diamond growth on non-treated substrates. Figure 6.5a shows photographs (HorS and VerS) and SEM images (VerS at the top

and bottom positions) of seeded samples after the diamond deposition. After 5 h deposition (sample nL5 VerS) the diamond film contains voids at the bottom part of the VerS, the size of grains was approximately 60 nm. The top part of the sample was already covered by a fully closed film. Increased deposition duration (10 h) resulted in a fully closed nanocrystalline diamond film over the whole substrate.

The thickness of the diamond films was determined from cross-sectional SEM images. As expected, the film thickness on the horizontal samples was almost constant over the whole sample. They revealed a homogeneous colour that by understanding of light interference with thin and smooth films indicates constant thickness (Figure 6.5a, small samples). Moreover, a fully closed film was observed for all HorS (SEM images not shown here). In contrast, the growth homogeneity was z-position dependent for vertically oriented samples. For example, the VerS nL5 and nL10 are characterised by iridescent colour (Figure 6.5, optical photograph). Changes in colours arise from interference fringes due to the varying thickness of the diamond film along the sample. Almost two times thicker film was measured on the top than on the bottom of the samples (located farther from the antennas), independently of deposition parameters Figure 6.5b). These trends are in good agreement with the surface coverage observed in the case of spontaneous nucleation. Such inhomogeneities were attributed to the vertical temperature gradient and distribution of growth species in the plasma volume [241–243].

As mentioned in the section 6.1.2.1, the film properties of horizontally placed samples were similar to the middle part of the vertically oriented samples. This statement is also well illustrated by the colour of the horizontally oriented, and the middle position of the vertically oriented sample nL10 (photographs in Figure 6.5a). It was also confirmed by film thickness measurements (Figure 6.5b). The film thickness of HorS was comparable to the thickness of VerS at the middle positions.

### 6.1.2.3 Raman spectroscopy measurements

The carbon phases of formed grains on both non-treated and nucleated (seeded) substrates were determined using Raman spectroscopy. The Raman spectrum observed at the top position (Figure 6.6a, red) of the non-treated sample after short 5 h growth reveals four features: the characteristic diamond peak at  $1326\text{ cm}^{-1}$ , a weak band at  $1360\text{ cm}^{-1}$  (D-band known as the defect-band), hardly detectable transpolyacetylene-like groups at  $1480\text{ cm}^{-1}$  and a broad G-band ( $\text{sp}^2$  carbon bonds) at  $1580\text{ cm}^{-1}$  [244].

The diamond peak is also resolvable at the bottom position (Figure 6.6a, blue), but the Raman spectrum is very noisy due to the low density of grown diamond clusters (SEM images in Figure 6.2, column 1). Moreover, the diamond peak is broadened and shifted to a lower wavenumber ( $1326\text{ cm}^{-1}$ ) compared to the bulk diamond  $1332\text{ cm}^{-1}$ . The linewidth broadening and redshift were observed for all non-treated samples, independently of the deposition parameters (L10, M10, H10). Both these features could be attributed to the phonon-confinement effects characteristically present for nanostructured materials [245]. In the case of nanodiamonds, the phonon-confinement

model says that the diamond peak shifts to lower values, as the size of nanodiamonds decrease. For example, Yoshikawa et al. predicted that the diamond peak could have a redshift of  $\sim 13 \text{ cm}^{-1}$  in energy and a linewidth broadening larger than  $50 \text{ cm}^{-1}$  as the diamond particle size dropped down to a few nanometres [246]. However, the redshift effect is more complex and it can also be influenced by induced stress at the interface between the substrate and the diamond due to different thermal expansion coefficients [247]. In contrast to this, no redshift of the diamond peak ( $1331 \text{ cm}^{-1}$ ) was measured on the nucleated (with fully closed diamond film and larger diamond crystals) samples (Figure 6.6c).

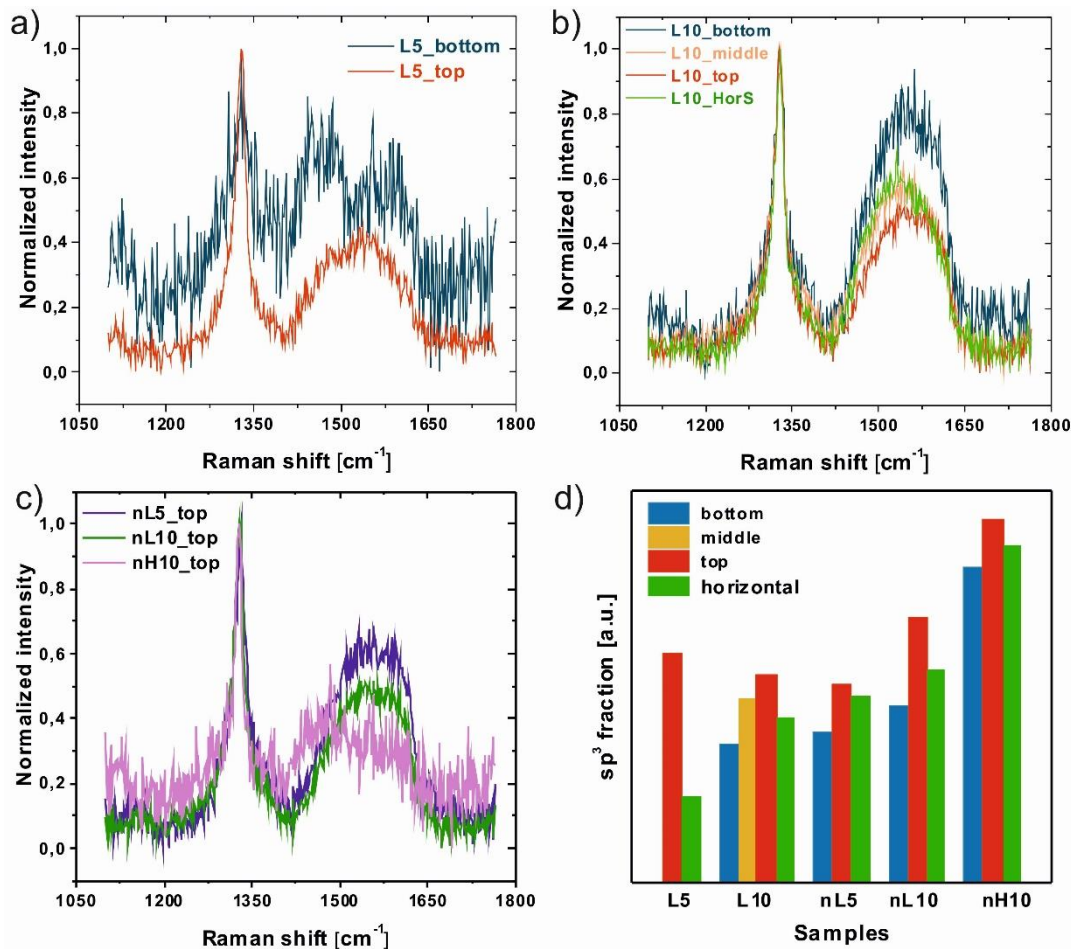


**Figure 6.6** Normalised spectra of non-treated Si samples exposed to a) short (5h) and b) long (10h) deposition durations at low H content. c) Normalised Raman spectra of nucleated VerS after the diamond growth at various parameters measured at the top position of VerS. d) Comparison of non-treated (L5, L10) and nucleated (nL5, nL10, nH10) samples in terms of  $sp^3$  fraction. The  $sp^3$  fraction is the ratio of  $A_{\text{diam}}/A_{\text{all}}$ , i.e. diamond peak area to sum of all areas (i.e. G-band, D-band, etc. including diamond peak area) calculated from the Raman spectra [81].

After longer (10 h) deposition, the Raman spectra (Figure 6.6b) become more resolvable for all measurement positions, due to the increased spontaneous nucleation density and proportional enlargement of grown grains. The decreasing intensity of the



G-band compared to the diamond peak intensity (bottom to top position) confirms an increased  $sp^3$  fraction, calculated as the ratio of the diamond peak area ( $A_{\text{diam}}$ ) to the sum of all areas ( $A_{\text{all}}$ ) within the spectral range from 1100 to 1765  $\text{cm}^{-1}$  (Figure 6.6d). The plotted  $sp^3$  fractions represent trends in relative values and they do not reflect the absolute amount of  $sp^3$  (or  $sp^2$ ) phases. The  $sp^3$  fraction increases with the deposition time, due to the enlargement of diamond crystals (on non-treated samples) or the increase of diamond film thickness (on seeded samples) (Figure 6.6c). Such a trend was also observed for the sample deposited at high hydrogen content in the gas mixture (sample nH10) which is attributed to the preferential etching of the  $sp^2$  carbon phases.

Next, for the vertically oriented samples L10, nL5 and nL10, we observed a slower growth at the bottom part (Figure 6.2) and consequently, a lower  $sp^3$  fraction was calculated at the bottom than at the top of the sample (Figure 6.6d). In this case, for the non-treated sample L5 at the bottom position, we were not able to evaluate this fraction due to a strongly noisy Raman spectrum. As a representative case, the relative  $sp^3$  fraction at the middle position of sample L10 is also plotted (Figure 6.6d). Relative  $sp^3$  fractions at the middle position VerS and HorS are similar to each other and correlate with SEM and AFM measurements. Finally, independently of the used deposition parameters all of the grown diamond films reveal a nanocrystalline character without obvious crystal faceting. This type of morphology indicates a dominance of the renucleation process over the columnar growth [60, 248].

### 6.1.3 Discussion

#### 6.1.3.1 Diamond growth in linear antenna microwave plasma system

Our results demonstrated that with optimised deposition parameters, spontaneous diamond nucleation with at least  $N_d \sim 6 \times 10^8 \text{ cm}^{-2}$  (sample L10, top position) can be achieved in a linear antenna microwave plasma system, even on non-treated and non-diamond substrates. Such nucleation density is 4–5 orders of magnitude higher than typically presented for clean Si substrates [68]. Furthermore, it was observed, that diamond grows sufficiently not only on horizontally oriented (HorS) but also on vertically oriented (VerS) samples over a range of several centimetres in the z-direction. However, the distance between the samples and the linear antennas undoubtedly influences the spontaneous nucleation efficiency on the samples. In comparison, conventional microwave CVD systems with plasma focused very close to the substrates ( $< 2 \text{ mm}$ ) operated at much higher pressures ( $> 10^3 \text{ Pa}$ ) and temperatures ( $> 800 \text{ }^\circ\text{C}$ ) are technically incompatible with deposition on substrates of complex geometry, such as screws, cutting inserts, etc.

The plasma volume in the linear antenna system can be divided into three regions, namely the “hot”, “diffusion” and “cold” region. Radicals and ions are generated around the antennas in the hot plasma region (with high  $T_e \sim 10 \text{ eV}$ ). Then, the growth species diffuse out from the hot region to the substrate holder region (i.e. cold plasma) which is

characterised by low electron temperatures ( $< 3$  eV) [47, 193, 249, 250]. This diffusion process allows deposition at a large distance from the antennas (in our case 7 cm). However, the distribution of ions and radicals varies (atomic hydrogen, oxygen species (OH), growth radicals ( $C_xH_y$ )) in the plasma volume along the z-axis, i.e. their concentrations drop down exponentially in the direction from the antennas to the substrate [193]. Thereby the samples in the vertical orientation are exposed to temperature and plasma density gradients. In other words, the VerS substrates were heated up by plasma in a non-uniform manner, resulting in a lower local temperature and lower growth rate at the bottom of the samples [241, 251]. The temperature gradient along the length of VerS led to a lower mean size of diamond grains on non-treated samples as the vertical position gets farther from the hot plasma region. Similarly, the thickness of fully closed diamond films on nucleated VerS decreased in the z-direction as well. In contrast, the temperature of the HorS was independently controlled (stabilised) by the sample heater, which resulted in a homogeneous temperature distribution and thus homogeneous diamond growth over the whole sample.

#### 6.1.3.2 Effect of gas mixture

Diamond growth is a complex process in which the growth of various carbon phases and their etching take place concurrently [51]. For that reason, enhancement of the spontaneous nucleation requires a careful optimisation of the deposition parameters [248]. The main variable parameters of the CVD process are deposition duration, microwave power, pressure, gas mixture composition and gas flow rate [61]. In this work, we studied the effect of deposition durations and gas mixtures in the linear antenna CVD system. First, we have shown that diamond nucleation and growth are suppressed when the hydrogen concentration in the gas mixture increases over the threshold value (samples H10). Here, the grains grown become smaller and the surface coverage decreases. Atomic hydrogen is proposed as the main factor controlling the diamond growth rate and quality during the CVD process [11]. It chemically reacts with the hydrocarbon gas and creates carbon-containing active growth species, mainly methyl radicals, i.e.  $CH_4 + H = CH_3 + H_2$ . The growth species diffuse onto the substrate surface and form C–C bonds necessary for diamond lattice formation. Moreover, in contrast to molecular hydrogen, atomic hydrogen is more reactive and preferentially etches non-diamond carbon phases ( $sp^2$  and  $sp^1$ ), at least twenty times faster than diamond ( $sp^3$  phases) [47, 50].

In the case of VerS, the concentration of atomic hydrogen in the plasma decreases with increasing distance from antennas [229, 252]. Thus, the chemical production of methyl radicals is lower which consequently reduces the diamond growth rate and surface coverage in the downward direction on VerS. Generally, in low temperature and low pressure plasma, the concentration of atomic hydrogen and its contribution to diamond growth is lower than in focused microwave plasma. Oxygen-containing gaseous phases ( $CO_2$ ) have to be added to the gas mixture to enhance the diamond growth rate and also to etch non-diamond carbon phases more effectively. The oxygen-based species (such as

CO<sub>2</sub>, CO, O<sub>2</sub> or alcohol) partially replace the role of hydrogen, accelerate the carbon saturation, reduce the incubation period, provide additional etching species (OH), thereby having a beneficial effect on the diamond growth rate and quality [47, 62, 253]. Thus, an oxygen-containing gas mixture is crucial for polycrystalline diamond growth in low pressure microwave plasma systems [249].

Low pressure MW plasma enhanced chemical vapour deposition involves a series of gas-phase and gas-surface reactions (growing grains, walls of the reactor) [254]. Furthermore, in the case of side-wall depositions on large substrates (i.e. in our case deposition on VerS) there are new factors involved such as the inhomogeneous distribution of growth species and gas radicals, temperature gradient, shielding effect (bottom part of the sample is shielded by its top part) [255], etc. To fully understand and explain the ongoing processes in the linear antenna microwave plasma, further experimental and theoretical studies are required, e.g. numerical simulations and in-situ plasma diagnosis as a function of process parameters and z-position. However, some analyses are inherently difficult in our experimental setup, e.g. the measurement of temperature distribution using thermocouples. Here, the unwanted interference of microwave radiation with thermocouple wires affects the induced thermocouple voltage, perturbing the measurement [256, 257].

### 6.1.3.3 Nucleation mechanisms

Coming back to the nucleation mechanisms, we can say that the size distribution of the spontaneously grown grains can be interpreted as the fingerprint of the growth process parameters. All the investigated samples showed a polymodal grain size distribution independently of the deposition parameters and substrate orientation. The underlying principle behind these observations is not clear so far. The nucleation/grain formation of diamond involves complex processes and current models are largely speculative. In the initial stage of CVD, the statistical fluctuation in the local adatom concentration results in the formation and decay of diamond clusters. If the fluctuation brings together a sufficient number of atoms and molecules, the cluster exceeds a certain critical size (corresponding to experimental parameters), they become thermodynamically stable nuclei [258]. The appearance of stable nuclei leads to the formation of individually growing crystals by 3D island growth (Volmer-Weber) model [42, 259]. It is a generally accepted fact, that the primary process responsible for diamond nuclei formation is heterogeneous nucleation on the substrate surface. In the case of Si substrates and high enough temperatures, the nucleation occurs on the  $\beta$ -SiC intermediate layer (1–10 nm), when the carbon concentration on the substrate surface reaches its saturated value [63, 76, 258]. In our case, we did not detect the presence SiC phases which can be explained by the low temperatures used in our experimental setup. However, it has to be stressed out that some studies revealed that gas-phase nucleation of diamond is also possible [250, 260–263]. Although, the number of diamond particles formed in the gas phase is certainly very small (compared to the heterogeneous nucleation at a surface),

they can reach the surface of the sample and increase the surface nucleation density, especially closer to linear antennas [42]. For low pressure diamond deposition, Hwang et al. suggested a non-classical crystallisation model, the so-called “charged cluster model” [264]. The model says that gas-phase nucleation (i.e. spontaneous generation of nanometre-sized negatively charged diamond nuclei), can occur under certain conditions. It should be noted that nanometre-sized (3–5 nm) diamonds are more stable than graphite [265]. According to this theory, the particles generated in the gaseous phase behave like colloidal particles (i.e. they can move freely due to Brownian motion) and become the building units of the thin films. The stability of the particles is ensured by the capillary effect and the negative charge. After landing, they tend to accommodate their structure to the surface structure (i.e. diamond or non-diamond phase) on which they land [266]. In the case of Si substrates, which have low charge transfer, the particles maintain their diamond structure and the deposition occurs through electrostatic self-assembly or colloidal crystallisation [267].

Based on the abovementioned model, the polymodal distribution of grain sizes and the provided studies, we assume that the observed size variation of the grains can be partially attributed to nuclei formation in the gas-phase. These particles arrive at the substrate and grow until another diamond particle falls on them, or they are etched by atomic hydrogen (or an oxygen species). In our case, the polymodal distribution of the grains was observed on the whole substrate surface. Assuming that the gas phase nucleation is not dependent on the local temperature of the substrate, then the substrate temperature affects the growth or etching of the landed diamond particles, so the size of observed grains is smaller in the downward direction where the temperature is lower. Finally, we can neglect any damaging of formed nuclei via ion bombardment due to the low pressure plasma range [193]. So, gas-phase spontaneous diamond nucleation seems to be more prominent due to specific process parameters in the linear antenna microwave plasma system, i.e. substrate is located at a large enough distance from the hot plasma region, there is a larger mean free path due to the low pressure and the plasma is operated in pulsed mode.

#### 6.1.4 Conclusion

In this chapter, the spontaneous nucleation and early stages of diamond growth on non-treated and seeded Si substrates were studied at low pressure in a linear antenna CVD system. Particular emphasis was placed on i) the sample orientation (vertical and horizontal) and ii) z-distance from the plasma source (top, middle and bottom position) of the vertically oriented samples and iii) different deposition parameters (deposition duration and hydrogen concentration in the gas mixture).

Spontaneous diamond nucleation was enhanced for specific gas chemistries and the nucleation densities were as high as  $10^8 \text{ cm}^{-2}$  which is 4–5 orders of magnitude higher than the spontaneous nucleation densities presented for Si in most CVD deposition

systems (focused microwave plasma, hot filament, etc.). The nucleation behaviour and subsequent diamond growth are strongly dependent on the  $z$ -distance from the plasma source (i.e. linear antennas) which was attributed to the varying densities of active species and the temperature decrease in the  $z$ -direction. The grain population exhibited polymodal size distribution on the whole substrate surface for both substrate orientations which indirectly indicates that besides the spontaneous heterogeneous nucleation on the substrate surface, homogeneous nucleation in gaseous phase also contributes to the diamond growth. Our findings confirm that the linear CVD plasma system can be routinely utilised for growing diamond on 3D substrates with complex geometry within the range of a few centimetres.

The above-demonstrated fabrication strategy was published in *Diamond and Related Materials* [81].

## 6.2 Three-dimensional diamond growth on a porous template

In the previous section it was demonstrated that low-pressure operation of the linear CVD plasma system allows diamond deposition also on 3D substrates. This finding was utilized for the fabrication of a porous diamond-based composite membrane, which was achieved by depositing diamond film on a 3D template (i.e.  $\text{SiO}_x$  fibre mat).

### 6.2.1 Experimental

Silica ( $\text{SiO}_x$ ) nonwoven three-dimensional nanofibre mats were produced using needleless electrospinning on a Nanospider device (Technical University of Liberec). These hydrophobic mats were used as substrates.

First,  $\text{SiO}_x$  fibre mats were treated in oxygen plasma (100 W power, 60 Pa gas pressure, 50 sccm oxygen flow rate, 60 s time) to get hydrophilic surfaces. Next, the substrates were seeded with diamond nanoparticles. After drying, the chemical vapour deposition of diamond films was carried out in a linear plasma CVD system (Figure 6.7).

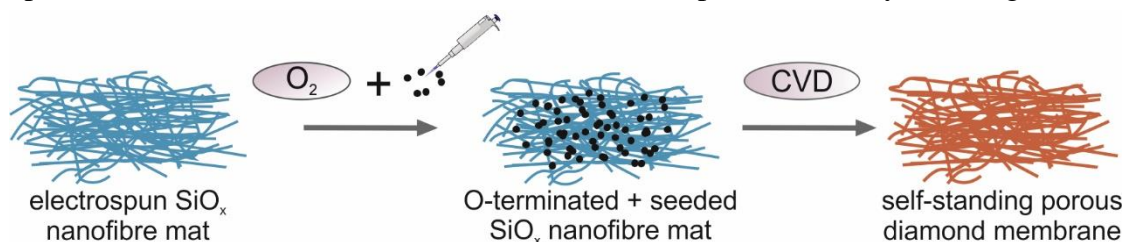


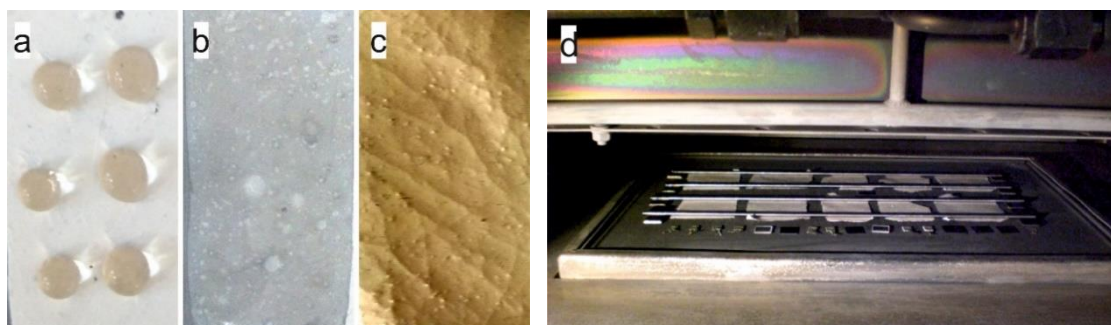
**Figure 6.7 Schematic view of the fabrication steps for the self-standing porous diamond membrane.**

The low-pressure operation of this system makes it suitable for diamond deposition on 3D substrates (i.e.  $\text{SiO}_x$  mat) as shown in section 6.1. The CVD parameters were as follows: gas mixture  $\text{H}_2:\text{CH}_4:\text{CO}_2=150:5:20$  sccm, MW power 2 kW, gas pressure 10 Pa, deposition time 60 h, temperature 550 °C.

Samples were characterised using scanning electron microscopy and Raman spectroscopy.

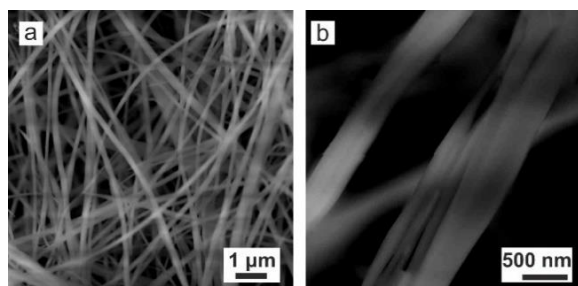
## 6.2.2 Results and discussion

From photographs (Figure 6.8a) it is evident that  $\text{SiO}_x$  nanofibers have a very strong hydrophobic character, which prevents the penetration of the water-based dispersion into the nanofibre layer during the seeding procedure. After oxygen plasma treatment the fibre mat becomes wettable (Figure 6.8b).



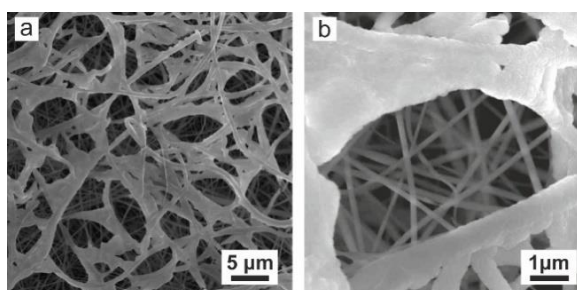
**Figure 6.8** Optical photographs of a  $\text{SiO}_x$  nanofiber mat a) without oxygen treatment (hydrophobic surface), b) after oxygen treatment (hydrophilic surface), c) after the CVD process, d) fibres before deposition inside the CVD system.

Figure 6.9 shows a SEM image of the highly porous structure of the  $\text{SiO}_x$  nanofiber mat after electrospinning. The mats comprise of randomly oriented sub-micron diameter fibres with a smooth surface. This porous 3D structure served as a template for the subsequent diamond deposition.



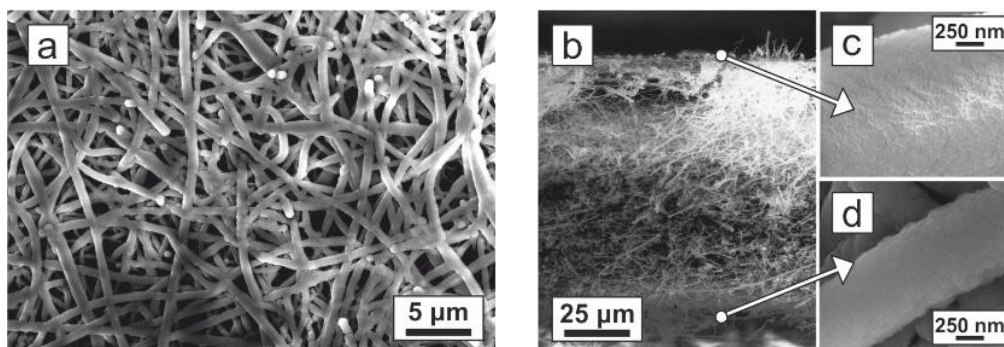
**Figure 6.9** Surface morphology of a cross-linked  $\text{SiO}_x$  fibre mat at different magnifications.

Figure 6.10a-b points out the importance of the oxygen plasma treatment and subsequent nucleation step in the fabrication process. These processes ensure homogeneous coating. The diamond nanoparticles act as seeds for the diamond deposition. However, the nucleation dispersion could not penetrate below the upper layer due to highly hydrophobic character of  $\text{SiO}_x$  mat. Consequently, the diamond film was observed on the upper layers only.



**Figure 6.10** Non-oxidized  $\text{SiO}_x$  fibres after diamond film deposition.





**Figure 6.11** a) Top view, b) cross-section view SEM images and the detailed view of the c) top and d) bottom part of  $\text{SiO}_x$  fibre mats after the diamond growth.

The photographs (Figure 6.8c) and SEM images (Figure 6.11) show the oxygen treated and nucleated nanofibre mat after the CVD process. The deposition system ensured excellent diamond film homogeneity over large areas ( $18 \text{ samples in size of } 3 \times 4 \text{ cm}^2$ ) along the horizontal direction (Figure 6.8d). The cross-section (Figure 6.11b) with details from the top (Figure 6.11c) and bottom (Figure 6.11d) of the  $\text{SiO}_x$  mat reveals hermetic coating also in the vertical direction, i.e. the fibres were covered by the diamond film in the whole volume. Very small morphological changes between the top and bottom part of the  $\text{SiO}_x$  mat ( $> 100 \mu\text{m}$ ) indicate similar film quality on both of its sides given by the low-pressure operation of the system. High seeding density was achieved by opposite dipole of diamond particles [268] and  $\text{SiO}_x$  fibres. Another advantage of the linear plasma CVD system is that it enables two-sided deposition on the fibre mat.

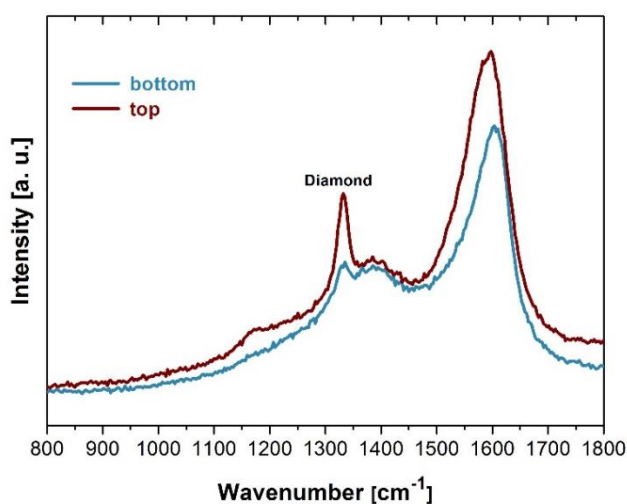


**Figure 6.12** Raman spectrum of the top and bottom of a diamond coated  $\text{SiO}_x$  mat.

The diamond character of the films was investigated using Raman spectroscopy with an excitation wavelength of 325 nm. The Raman spectra dominated by the diamond characteristic peak centred at  $1332 \text{ cm}^{-1}$  (Figure 6.12). This confirms that three-dimensional porous self-standing diamond-based composite membranes were obtained.

It is also evident that the primary structure of the fibrous material remained unchanged, the individual fibres in the mat served as templates for the diamond deposition. The fibre diameter, average pore size and spacing was defined by the electrospinning process. Their surface terminations (with hydrogen and oxygen plasma treatment) lead to controllable surface wettability (hydrophilic, hydrophobic surface).

### 6.2.3 Conclusion

Our experiments demonstrated that templated growth using chemical vapour deposition of polycrystalline diamond films on randomly oriented SiO<sub>x</sub> fibre mats is a simple, low-cost and effective way to produce self-standing porous membranes. The diamond film replicated the initial microstructure of the fibres. The fibre diameter, average pore size and spacing was primarily predefined by the electrospinning process. The final pore size can also be tuned using the diamond thickness. In summary, we can conclude that linear plasma CVD system is a suitable system for large area porous diamond structure growth. The originality of the preparation procedure is confirmed by our utility model [269].

The created porous membrane seems to be a promising material suitable for bone tissue engineering or regenerative medicine [5, 270]. In-vitro biocompatibility and bioactivity studies (e.g. Saos-2 cells) are in progress in collaboration with Institute of physiology of the Czech Academy of Sciences.

## 6.3 Polymer-based nucleation of diamond films

This section focuses on the influence of polymer coatings on the nucleation and growth of diamond films using microwave plasma enhanced chemical vapour deposition. Silicon substrates were coated with three types of polymer: i) poly(1-phenylethene) (commonly known as polystyrene, PS), ii) poly(lactic-co-glycolic acid) (PLGA) and iii) polyvinyl alcohol (PVA). All of these polymers are widely used and easily commercially available in different forms (e.g. nano/microspheres, granules, fibres, etc.). We used PS in the form of microspheres, PVA in the form of thin films and PLGA in the form of microspheres as well as thin films (mono- and multilayers). Besides these experiments, the diamond growth from PLGA and PVA polymer composites containing diamond nanoparticles was also studied. The obtained results are compared with reference samples: i) clean and ii) ultrasonically seeded Si substrates.

### 6.3.1 Experimental

#### 6.3.1.1 Materials and sample preparation

Ultrasonically cleaned silicon (100) wafers of size 1 × 1 cm<sup>2</sup> were used as substrates, which were treated in oxygen plasma to achieve hydrophilic surfaces. Then were coated by polymers in different forms. The complex description of used materials is summarised in Table 6.2 and Table 6.3.



**Table 6.2 Materials used for study of diamond nucleation from polymer coatings [77].**

Material	Molecular formula	Specification	Dispersion composition	Form on the sample
PS	$(C_8H_8)_n$	aqueous dispersion (5 wt%) of PS with diameter of 940 nm (microParticles GmbH, Germany)	PS:methanol 1:2	monolayer of microspheres
PLGA	$(C_6H_8O_4 \cdot C_4H_4O_4)_n$	Degradex, PLGA microspheres with diameter of 1 $\mu$ m, freeze dried (Phosphorex, Inc., USA)	1.2 mg of PLGA in 80 $\mu$ l DI <sup>a</sup> (15 wt%)	monolayer of microspheres
PLGA	$(C_6H_8O_4 \cdot C_4H_4O_4)_n$	PLG 8531 grade copolymer granules of L-lactide and Glycolide in a 85/15 molar ratio (Purasorb)	20 mg of PLGA in 1 ml DCM <sup>b</sup> (20 wt%)	thin film (mono- or multilayer)
PVA	$(C_6H_4O)_n$ or $[-CH_2CHOH-]_n$	poly(vinyl alcohol) hydrolysed powder, mol wt 89,000-98,000 (Sigma Aldrich, Germany)	150 mg pf PVA in 30 ml DI <sup>a</sup> (5 wt%)	thin film
DNPs <sup>c</sup>	-	ultra-dispersed detonation diamond powder, (NanoAmando Aqueous Colloid: Dispersed Buckydiamond with a median diamond grain size of 4.8 $\pm$ 0.6 nm)	~10 wt% of diamond nanoparticles (dispersed in DI <sup>a</sup> )	thin film with nanoparticles

<sup>a</sup> deionised water, <sup>b</sup> dichloromethane, <sup>c</sup> diamond nanoparticles

Note to the data in Table 6.2, the aqueous dispersion of PS microspheres was diluted in Triton X-100/methanol solution (1:400) at a ratio of 1:2. The PLGA granules were dissolved in dichloromethane and the PVA granules in deionised water using magnetic stirring for 1 h.

**Table 6.3 Polymer composites used for diamond nucleation [77].**

Nucleation method	Polymer	Dispersion composition
I. polymer + DNPs	PLGA or PVA	3 ml of polymer solution (5 wt%) + 5 mg of dry DNPs
II. polymer + (DNPs in DI)	PVA	5 wt% of polymer solution (PVA in DI) + 10 wt% of DNPs in DI by different ratio (3:1, 1:1, 1:3)

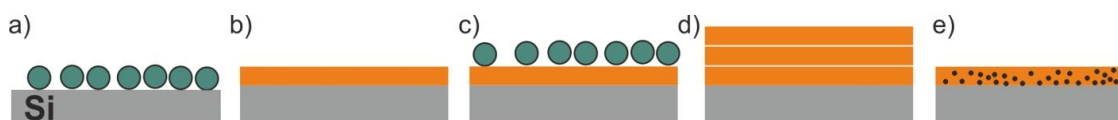


**Figure 6.13 Schematic illustration of polymer coatings used for diamond nucleation: a) monolayer of microspheres, b) polymer monolayer, c) combination of monolayer and microsphere array, d) multilayer and e) polymer composite monolayer containing diamond nanoparticles [77].**

The polymers (both microspheres and thin films) were applied onto the Si substrates using spin-coating. Approximately 50  $\mu$ l of polymer dispersion was dropped onto the substrate surface. The parameters for spin-coating were optimised for specific polymer dispersions (i.e. for microspheres to obtain hexagonal-close-packed monolayer and for thin polymer films to achieve homogeneous coverage over the whole substrate surface). The rotation speed was varied in the range 1000–8000 rpm and process duration within 1–3 min. The following combinations of polymers were studied: monolayer of polymer microspheres, bilayer (i.e. combination of microspheres and thin polymer layers) and multilayers (i.e. thicker polymer film) obtained by multistep spin-coating. The applied polymer coatings are schematically illustrated in Figure 6.13.

In the case of polymer composites, two strategies were employed. In the first strategy (labelled as I. in Table 6.3) diamond nanoparticles were directly dispersed in polymer solution (PLGA or PVA). In the second one (labelled as II.) DNPs were first dispersed in deionised water and then mixed with a PVA polymer solution at different ratios (3:1, 1:1 and 1:3). PVA was chosen because it is water-soluble, and has excellent film forming and emulsifying adhesive properties. For PLGA experiments it was not possible to use water-based DNP dispersion because the solvent (DCM) of PLGA is not miscible with water. Furthermore, PLGA degrades in the presence of water.

Simultaneously with the diamond growth on polymer coated Si substrates, reference samples were used as well: i) clean Si substrates (i.e. ultrasonically cleaned and oxygen plasma treated substrates) and ii) Si substrates standardly nucleated using ultrasonic seeding with DNPs [73].

The diamond growth process was carried out in focused plasma CVD system (see section 4.1.1). The deposition process parameters for the experiments with microspheres and polymer layers were as follows: gas mixture 1% CH<sub>4</sub> in H<sub>2</sub>, gas pressure of 5 kPa, MW power of 2.5 kW, deposition duration up to 1 h and temperature ~ 800 and ~ 650 °C (for set 2 and set 3, respectively). Deposition parameters for the experiments with polymer composites were as follows: gas pressure of 3 kPa, MW power of 2.5 kW, process duration 2 h and substrate temperature about 300 °C.

The samples were characterised using scanning electron microscopy and Raman spectroscopy ( $\lambda = 442$  nm). Statistical analysis of diamond clusters (e.g. surface coverage, distribution) was determined from low magnification (5–20 kx) SEM images using image processing and analysis software (Atlas, Tescan, Ltd.).

## 6.3.2 Results and discussion

### 6.3.2.1 Microspheres and polymer layers

In the first set of experiments, monolayers of PS or PLGA microspheres were studied. Figure 6.14a shows the surface morphology of a Si substrate covered by a hcp monolayer of PS microspheres with a diameter of 940 nm. After diamond CVD, the PS microspheres were etched away, only fingerprints of the original microspheres were observed, which preserved the periodicity of their initial ordering (Figure 6.14b). Diamond growth was not observed, even when deposition parameters were varied (the temperature varied from 400 to 900 °C and methane concentrations from 0.5 to 5%). Similar results were obtained for PLGA microspheres with a diameter of 1  $\mu$ m. In comparison, for the ultrasonically seeded Si substrate, standard deposition parameters (2% CH<sub>4</sub> in H<sub>2</sub>, 900 °C, 30 min) resulted in the growth of a thin fully closed polycrystalline diamond film consisting of very small grains (<100 nm, Figure 6.14) [271].

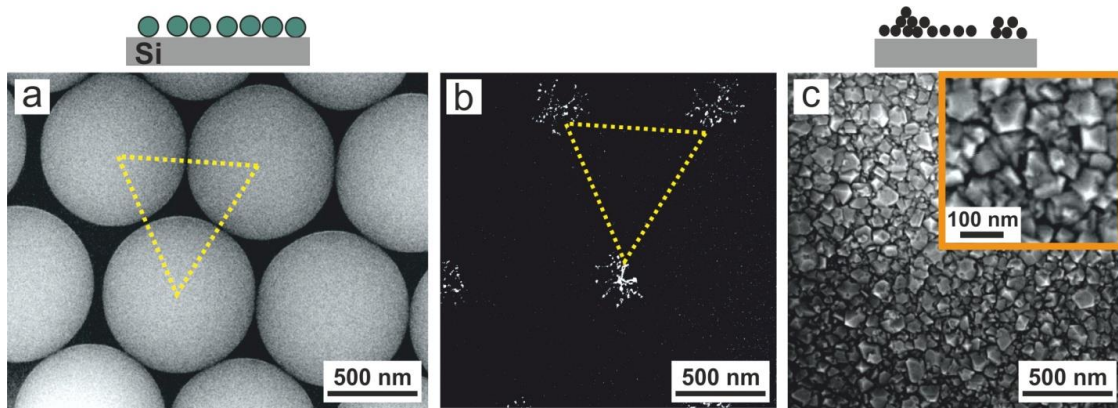


**Figure 6.14** SEM images of a monolayer of PS (940 nm) microspheres a) before and b) after the diamond CVD. The yellow triangles illustrate the initial and preserved periodicity of the microspheres before and after the diamond CVD. c) Surface morphology of diamond film grown on the reference (ultrasonically seeded with DNPs) sample [77].

These results reveal that the etching of polymer microspheres is too fast and PS does not promote the diamond growth. As soon as the deposition process starts, the diameter of the spheres is reduced and the close-packed monolayer becomes non-close-packed. Then reactive species from plasma penetrate into the gaps between the spheres and their etching further accelerates because the etching occurs in all directions. In the next set of experiments, polymer films were studied, which seem to be more resistant to plasma etching.

First, a 250 nm thin PLGA polymer film was used. After the diamond CVD, randomly distributed diamond clusters with a diameter of  $\sim 300$  nm were observed on the Si surface. However, the surface coverage was nearly the same as for the clean Si substrate ( $\sim 12\%$ ) (Figure 6.15a-b). For the clean Si, the appearance of isolated diamond crystallites is attributed to spontaneous nucleation (see section 6.1) [79, 81, 248].

For all the samples, the diamond character of deposited clusters was confirmed using Raman measurements, which exhibited a sharp diamond peak located at  $1331\text{ cm}^{-1}$  (Figure 6.15d).

Surface coverage increased nearly five times (up to  $\sim 61\%$ ) when the thin PLGA polymer layer (250 nm) was covered by an additional layer of PLGA microspheres (Figure 6.15c). This observation indicates that applying thicker PLGA layers increases the number of active centres, while thicker PLGA layers could promote diamond growth either as a source of carbon or via the transformation of polymer to  $\text{sp}^3$  carbon phases. Moreover, a thicker polymer film equalises the ratio between two competitive processes, i.e. polymer etching and diamond growth. Therefore, the next set of experiments focused on investigating the dependence of nucleation on the polymer film thickness. In addition, to minimise the spontaneous nucleation observed in the first experiments (Figure 6.15a), the deposition temperature was decreased to  $650\text{ }^\circ\text{C}$ .

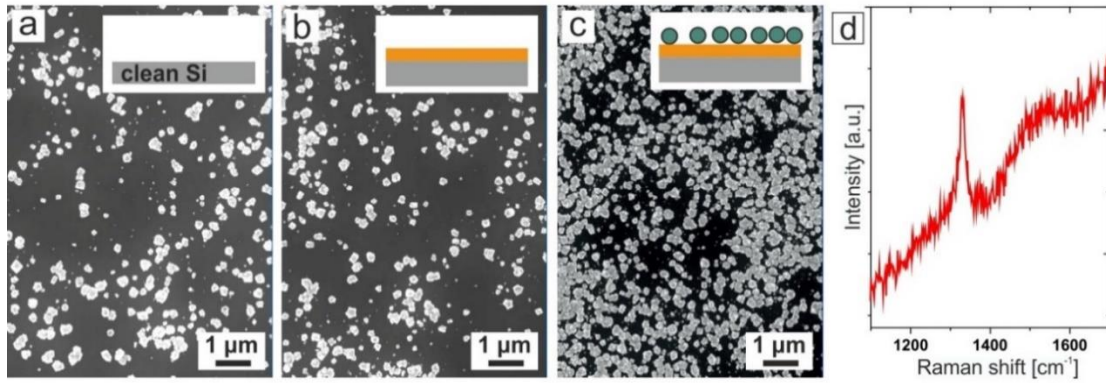


**Figure 6.15** Surface morphology of samples after the diamond CVD of a) clean Si substrate, b) Si sample covered by c) thin PLGA layer and c) thin PLGA layer and PLGA microspheres. d) Representative Raman spectrum of diamond grains grown on sample covered by thin PLGA layer (deposition parameters were as follows: 1% CH<sub>4</sub> in H<sub>2</sub>, 800 °C, 1 h) [77].

Figure 6.16 shows the surface morphology of Si substrates coated with one, two and three PLGA layers and a reference sample, after the diamond CVD. The thickness of polymer films was evaluated to ~ 250 nm, ~ 500 nm and ~ 750 nm for one, two and three layers, respectively. After the diamond CVD, the surface of the clean Si substrate (not shown here) and the Si substrate coated with the polymer monolayer (Figure 6.16a) remained nearly featureless. For both these samples, the spontaneous nucleation was suppressed and the thin polymer layer did not promote any diamond nucleation and growth.

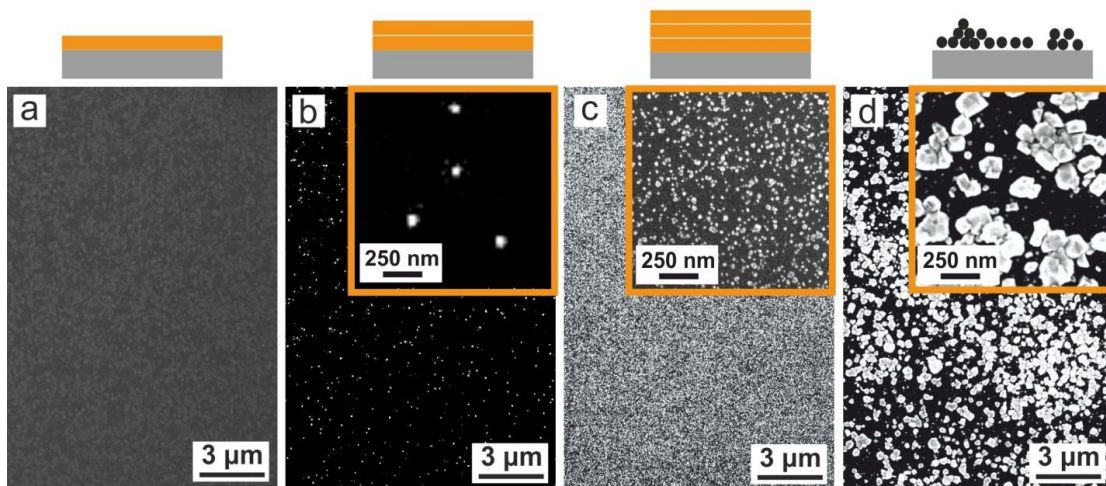


**Figure 6.16** Surface morphology of samples coated with polymer layers of different thicknesses after the diamond CVD. Si substrate covered by a) one, b) two and c) three PLGA polymer layers. d) Reference (ultrasonically seeded with DNPs) Si substrate (deposition parameters were as follows: 1% CH<sub>4</sub> in H<sub>2</sub>, 650 °C, 1 h) [77].

The two times thicker PLGA film resulted in the growth of sparsely distributed and isolated diamond clusters ~ 70 nm in size (Figure 6.16b). Further increase of the PLGA film thickness to ~ 750 nm (i.e. three layers) led to the formation of the most

densely distributed diamond clusters (Figure 6.16c). The size of the clusters was ~ 30 nm, which is much smaller than in the case of the reference sample (Figure 6.16d). The reason for this size difference is probably the longer incubation period, which precedes the nucleation process for the sample covered with PLGA polymer. The diamond character of formed clusters was confirmed using Raman spectroscopy (not shown here). Raman spectra revealed features similar to the previous experiments (Figure 6.15d).

Diamond growth from a polymer layer is a complex issue which generally involves two competing processes – i) diamond growth from the additional source of carbon contained in polymer chains and ii) polymer melting, decomposing and full etching by atomic hydrogen. It was demonstrated that the equilibrium between these processes is sensitive to the diamond deposition parameters. During the early stages of growth, the concentration of carbon in the close vicinity of the Si substrate surface is higher (from polymer as the solid source), which can enhance the formation of diamond nuclei or polymer transformation into the  $sp^3$  bonded carbon phase (i.e. diamond phase). A similar transformation was observed for polycarbyne polymers [85–87].

Additionally, the polymer film thickness plays a crucial role. An adequately thick polymer layer (750 nm for PLGA) provided a denser distribution of diamond clusters (i.e. nucleation centres) than typically used ultrasonic seeding with DNPs. Finally, such densely packed clusters with small diameter allowed the deposition of fully closed ultrathin diamond coatings (< 100 nm) suitable for optical applications [88].

### 6.3.2.2 Polymer composites

In the last set of experiments, Si substrates were covered with PLGA and PVA polymer composites containing diamond nanoparticles (Figure 6.17). The direct dispersion of diamond nanoparticles in a polymer solution (first strategy) resulted in the formation of large and sparsely distributed diamond clusters. For the PLGA polymer composite, the size of clusters varied from 400 to 800 nm in diameter (Figure 6.17a). In the case of PVA composite, the clusters were smaller (100–500 nm, Figure 6.17b). The higher degree of agglomeration of DNPs in PLGA than in PVA dispersion is mainly attributed to a different solvent being used (Table 6.2). In the second strategy, the PVA granules were first dispersed in deionised water and only then mixed with the polymer solution. In this case, the formed diamond clusters were smaller (30–50 nm) and they became more homogeneously distributed (Figure 6.17c and d). During the initial stage of the diamond growth from polymer composites, some processes taking place could be the same as in the case of the previously discussed pure polymer layers. However, in this case, the polymer acts as the carrier matrix for the diamond nanoparticles which primarily promote the diamond growth.



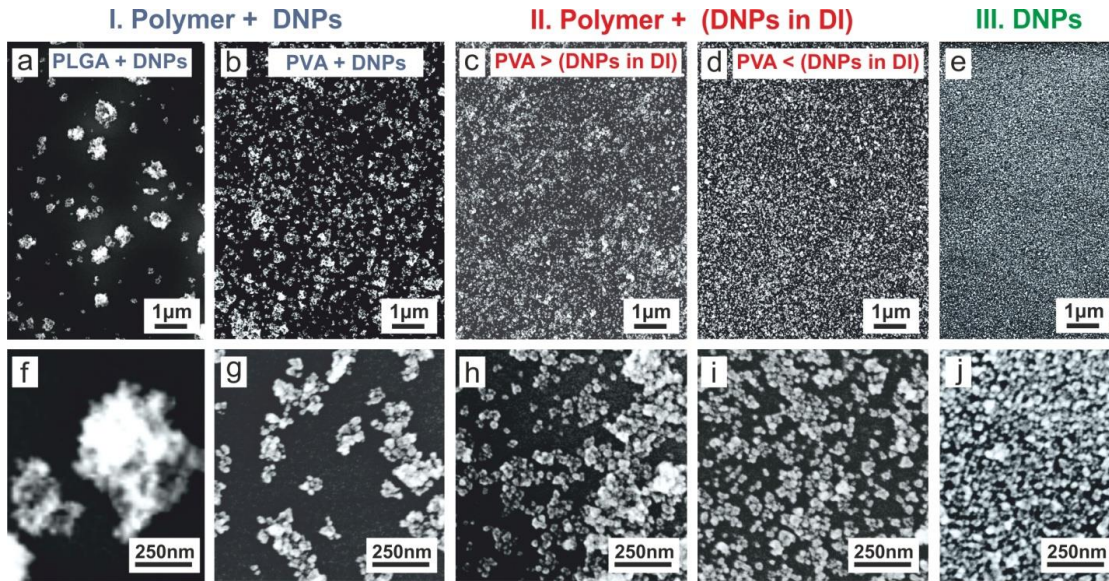


**Figure 6.17** Surface morphology of samples covered by polymer composites after diamond CVD: a-b) PLGA and PVA solution mixed with DNPs; c-d) PVA solution mixed with DNPs dispersed in deionised water at a ratio of c) 3:1 and d) 1:3; e) reference Si substrate (ultrasonically seeded with DNPs). f-j) SEM images taken at higher magnification for the corresponding substrates (deposition parameters were as follows: 1% CH<sub>4</sub> in H<sub>2</sub>, 300 °C, 2 h) [77].

Further, it was observed that the morphology and density of grown crystals are influenced by the mixing ratio of the polymer solution and deionised water with diamond nanoparticles (labelled as “DNPs in DI”). By decreasing the mixing ratio of PVA to “DNPs in DI” the agglomeration of nanoparticles was lower and the dispersion led to a more homogeneous distribution of diamond on the substrate. The ratio of 3:1 PVA to “DNPs in DI” resulted in a less homogeneous distribution of diamond clusters and the agglomerates were larger in size up to 200 nm (Figure 6.17c). For the opposite ratio (i.e. 1:3), the diamond CVD led to the formation of more homogeneously distributed diamond clusters on the Si surface without any larger agglomerates (Figure 6.17d). This surface morphology is similar to the reference sample nucleated using ultrasonic seeding with diamond nanoparticles (Figure 6.17e). The nucleation method based on the PVA composites with diamond nanoparticles has been already successfully utilised for diamond growth on a fragile 3D GaN membranes [248].

### 6.3.3 Conclusion

We presented a simple and low-cost polymer-based nucleation process as an alternative to the standard nucleation methods used for initialising diamond growth. Three different forms and three types of polymers (polystyrene, poly(lactic-co-glycolic acid) and polyvinyl alcohol) were studied including microspheres, thin films and composites. It was shown that thin polymer layers (< 250 nm) or microsphere (diameter of ~ 1 μm) monolayers did not contribute to diamond nucleation and growth in a broad window of

process parameters. However, using thicker continuous polymer films ( $> 750$  nm) or a combination of thin film/microsphere arrays unambiguously led to a homogeneous diamond growth. In the case of polymer/DNPs composites, the PLGA resulted in a high degree of DNPs clustering. On the other hand, the PVA based composite enabled a better distribution of DNPs with a comparable nucleation density to the standard ultrasonic seeding. In summary, we showed that the optimised polymer-based nucleation process has a high enough nucleation density and is usable for deposition of fully closed ultrathin diamond coatings ( $< 100$  nm) on mechanically soft, fragile or unstable substrates.

The above-demonstrated fabrication strategy was published in Journal of applied polymer science [77].



## 7. Structuring of polycrystalline diamond thin films

This chapter is devoted to the fabrication of diamond structures using various approaches (both top-down and bottom-up). Structuring using i) maskless plasma etching and ii) self-assembled monolayer of polystyrene sphere masks (i.e. microsphere lithography) is demonstrated.

### 7.1 Diamond film deposition and characterisation

Deposition of micro- (MCD) and nanocrystalline (NCD) diamond films was carried out on seeded silicon substrates (in sizes of  $1 \times 1 \text{ cm}^2$ ) in focused plasma CVD system. The deposition parameters for MCD films were as follows: MW power 3 kW, pressure 7 kPa, 5%  $\text{CH}_4$  in  $\text{H}_2$ , 1.5%  $\text{CO}_2$  in  $\text{H}_2$ , temperature 890 °C, deposition duration 2 h. NCD films were grown at the following deposition parameters: MW power 3 kW, pressure 7 kPa, 2%  $\text{CH}_4$  in  $\text{H}_2$ , 1%  $\text{N}_2$  in  $\text{H}_2$  and 2.5 h of deposition duration. These parameters resulted in the growth of MCD and NCD films with thicknesses of  $\sim 1 \mu\text{m}$ . Samples were characterised using scanning electron microscopy, atomic force microscopy, Raman spectroscopy ( $\lambda = 325 \text{ nm}$ ) and profilometre.

#### 7.1.1 Micro- and nanocrystalline diamond films

Figure 7.1 shows the surface morphology of micro- and nanocrystalline diamond films.

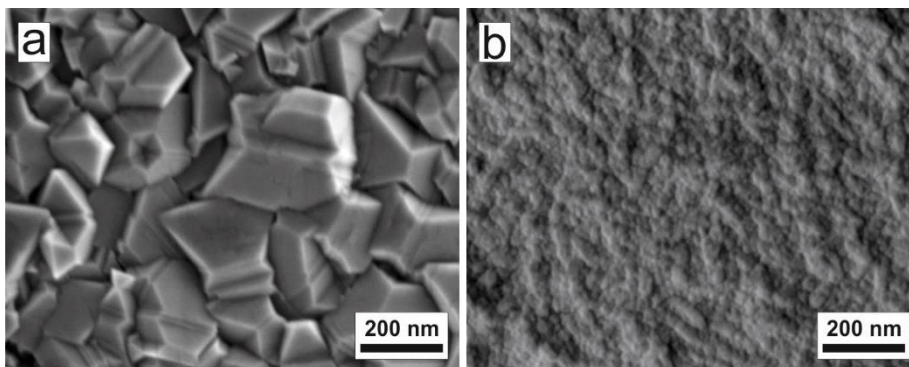
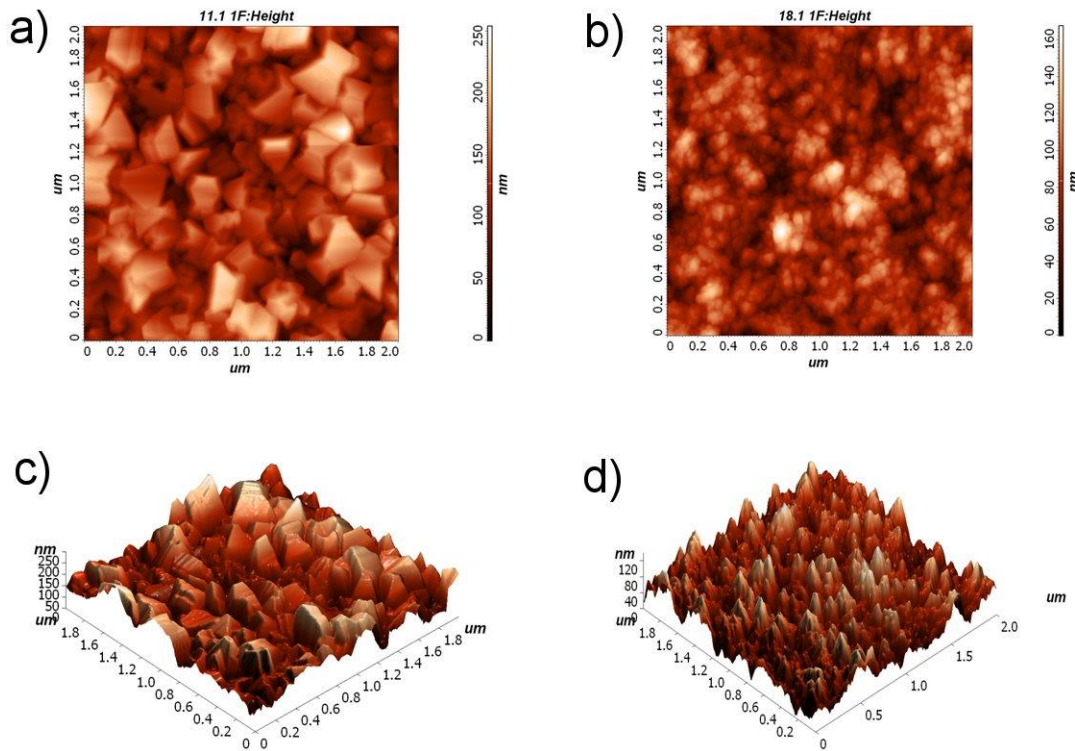


Figure 7.1 SEM images of a) micro- and b) nanocrystalline diamond films [272].

The MCD film consists of large, well-faceted crystals in sizes from 400 to 600 nm. Crystal faceting resulted in higher root-mean-square surface roughness (RMS)  $\sim 40 \text{ nm}$ . In contrast to MCD, the NCD film reveals smaller grains ( $< 50 \text{ nm}$ ) and its

surface is flatter (RMS < 22 nm). Figure 7.2 shows the 3D topography of diamond films provided using atomic force microscopy.



**Figure 7.2** AFM images of a) micro- and b) nanocrystalline films with their 3D image representations (c, d) [272].

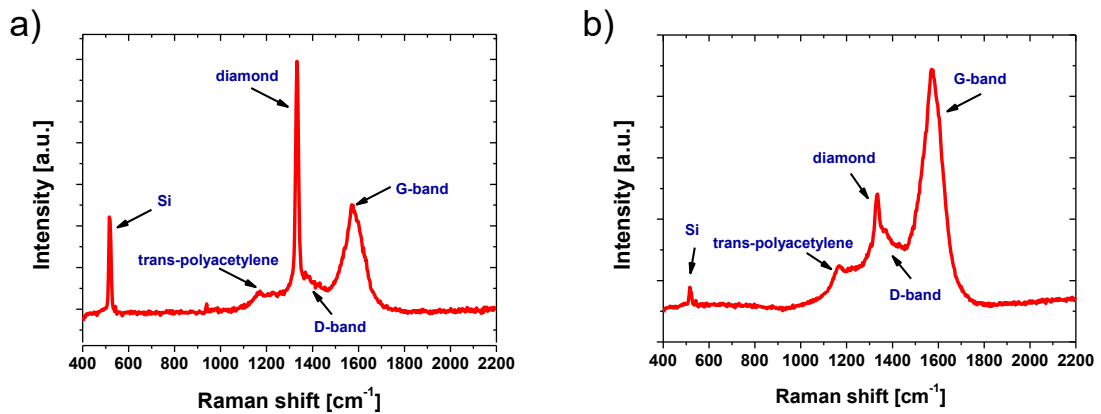


**Figure 7.3** Raman spectra of a) micro- and b) nanocrystalline films [272].

Raman spectra of micro- and nanocrystalline films are shown in Figure 7.3. They clearly confirm the diamond character for both films. For the microcrystalline film, the spectrum is dominated by a sharp peak located at  $1332\text{ cm}^{-1}$ , which is the characteristic line for the phonon mode of the  $\text{sp}^3$  crystalline diamond phase. The two broad bands located at frequencies  $1370$  and  $1500\text{ cm}^{-1}$  are attributed to the D-band (defects) and G-band (graphite) which represent the non-diamond carbon ( $\text{sp}^2$ ) phases [273]. The broad

band at  $950\text{ cm}^{-1}$  belongs to the 2<sup>nd</sup> order of Si. The weak band centered at  $1150\text{ cm}^{-1}$  corresponds to trans-polyacetylene-like groups at grain boundaries [274, 275]. In NCD films, the crystals are much smaller, and more  $\text{sp}^2$  carbon phases are present at grain boundaries. Therefore, the intensity of the G-band increases substantially and the intensity of the diamond peak decreases, but nevertheless is still resolvable.

## 7.2 Maskless surface structuring of diamond films

The maskless surface structuring was carried out in a CCP-RIE system. Half of the sample was covered by Si substrate to evaluate the etching rates (using profilometre measurements). Four different gas mixtures were used for etching the diamond films: i) pure oxygen plasma, ii) 4%  $\text{CF}_4$  in  $\text{O}_2$ , iii) 4%  $\text{SF}_6$  in  $\text{O}_2$  and iv) 4% Ar in  $\text{SF}_6$ . The other process parameters were kept constant for all samples: RF power of 100 W, pressure of 12 Pa and etching duration of 10 min [175].

### 7.2.1 Reactive ion etching in $\text{O}_2$ and $\text{CF}_4/\text{O}_2$ gas mixtures

The surfaces of MCD and NCD diamond films etched in pure oxygen plasma are shown in Figure 7.4a-b. The single diamond crystals, which were “damaged” by the process, can be clearly distinguished in the top view images of the MCD film. Due to observed nanorods, it seems to be better to display surface morphology of MCD film on the angle view images. After etching, the MCD and NCD films are similar, both are characterised by small diamond nanorods close to each other. The only difference between them is related to the surface roughness (when studied over a large area) due to the high initial roughness of MCD films before the etching process (large diamond crystals). It is apparent that etching by  $\text{O}_2$  led to the formation of diamond needle-like structures (so-called whiskers). The formation of these nanorods has multiple reasons. The basic one is connected with the vertical acceleration of ions towards the substrate and physical sputtering also taking place besides chemical etching. Moreover, it is well-known that oxygen etches  $\text{sp}^2$  carbon bonds much faster than  $\text{sp}^3$  diamond bonds [276], which also results in the formation of needle-like structures along grain boundaries. Furthermore, needles can also be formed within the grains at intrinsic defects in the crystals or in specific grains depending on their orientation [103]. In NCD films, the presence of more  $\text{sp}^2$  carbon bonds at grain boundaries correspond to an even more apparent formation of needle-like structures [107].

It has to be emphasized that a small amount of  $\text{CF}_4$  (4%  $\text{CF}_4$  in  $\text{O}_2$ ) have a strong influence on the surface morphology (Figure 7.4c-d). In comparison to the previously etched sample (in pure oxygen plasma), the surface of the MCD film is much flatter, with sharp needles or walls found at grain boundaries. A similar effect could also be observed from the top view image of the NCD film. However, in the case of NCD, this effect is not so apparent. Formation of needles or thin walls at the edge of grains is due to defects and  $\text{sp}^2$  carbon bonds, which had different etching rates than diamond bonds.

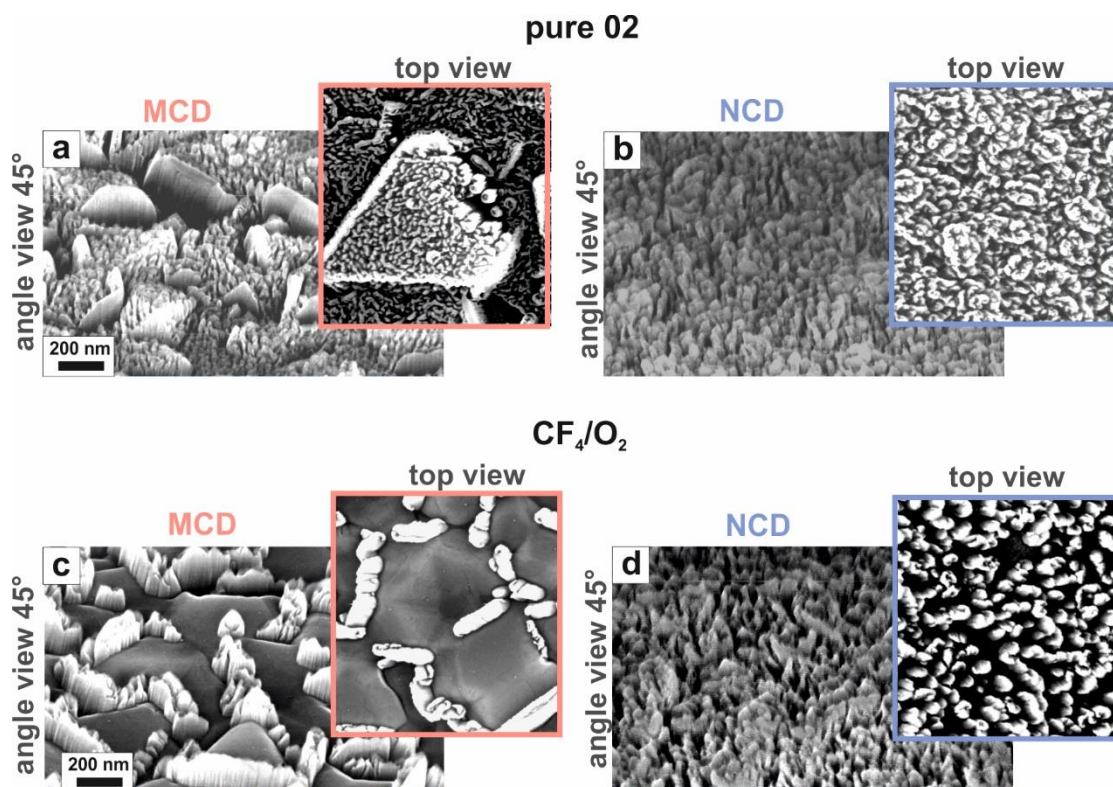


**Figure 7.4** Angle view SEM images of the surface morphology of MCD (left) and NCD (right) diamond films etched in a, b) pure oxygen plasma and c, d) 4% CF<sub>4</sub> in O<sub>2</sub>. Insets show top view images [277].

### 7.2.2 Reactive ion etching in SF<sub>6</sub> and Ar gas mixtures

The addition of a small amount of SF<sub>6</sub> (4%) into O<sub>2</sub> gas resulted in a similar surface morphology as in the case of pure oxygen plasma (Figure 7.5a-b). The surface is roughened both for MCD and NCD film, but with shorter nanorods. In addition, oxygen and sulfur hexafluoride (SF<sub>6</sub>), when mixed together, create the oxyfluoride ion (OF<sup>-</sup>). The oxyfluoride ion is a powerful etching agent for diamond. It is particularly good at breaking the carbon-carbon molecular bonds of the diamond and removing the molecule rapidly [278].

As it was already shown, application of little amount of SF<sub>6</sub> caused roughening of diamond during the etching due to a micromasking effect. That is, small regions on the surface appeared to be masked by impurities of some type that led to spire-like (whiskers) formations. This led to a significant increase in surface roughness during the etching. When enough SF<sub>6</sub> was added the area of micro-masking regions were minimized and the surface roughness did not change significantly during the process [279].

Adding 4% Ar into SF<sub>6</sub> gas also minimised the micro-masking effect and achieved high surface smoothness (Figure 7.5c-d). The SEM images of samples showed smooth surfaces without presence of any nanorods or whiskers. In comparison to the previous samples, using Ar/SF<sub>6</sub> resulted in a lateral-like etching, where the diamond crystals were etched not only vertically from top to bottom, but also in a horizontal direction.



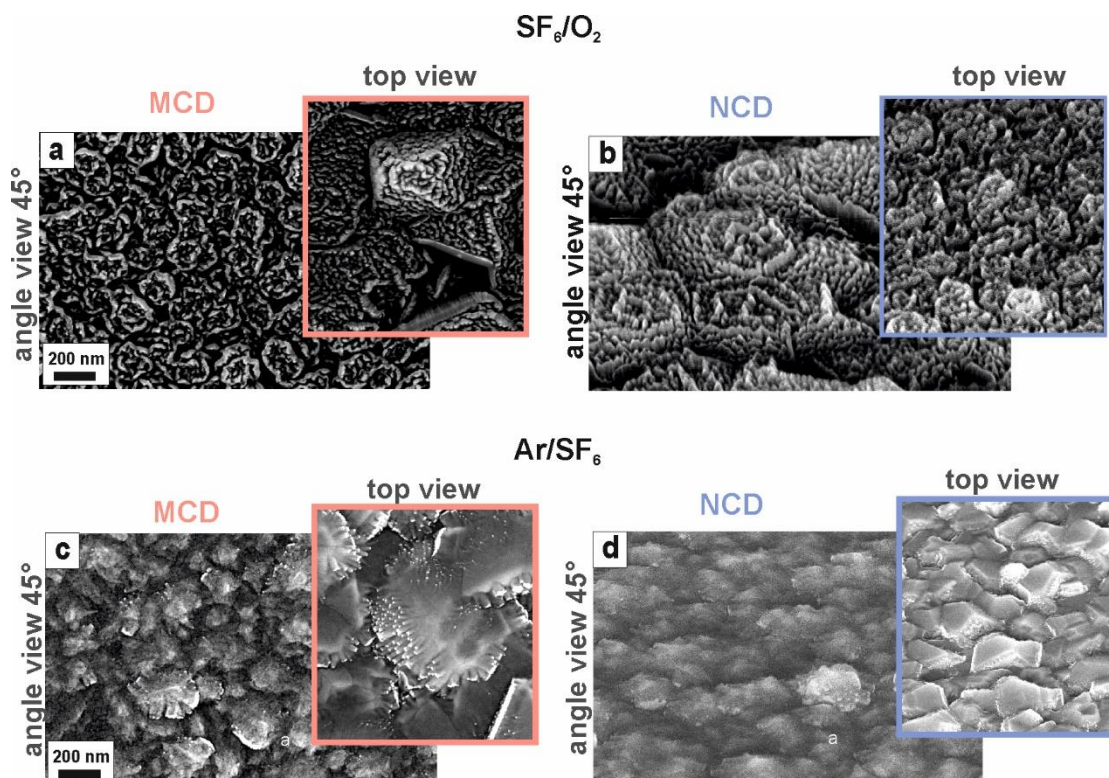


Figure 7.5 Angle view SEM images of the surface morphology of micro- (left) and nanocrystalline (right) diamond films etched in a, b) 4% of  $\text{SF}_6$  in  $\text{O}_2$  and c, d) 4% of Ar in  $\text{SF}_6$ . Insets show top view images [277].

### 7.2.3 Etching rates of diamond films

Figure 7.6 summarises the etching rates for NCD films. In the case of oxygen plasma, the etching rate was 27 nm/min. After adding 4%  $\text{CF}_4$  to the oxygen plasma, the etching rate increased to 29 nm/min. The lowest etching rate (13 nm/min) was found for the gas mixture of 4%  $\text{SF}_6$  in oxygen. For the  $\text{Ar}/\text{SF}_6$  gas mixture, the etching rate was 20 nm/min. For further insight into the etching process, the self-bias voltage induced during the etching process is also plotted (Figure 7.6, orange). Self-bias voltage was  $-61$  V for  $\text{O}_2$  plasma, it achieved the highest value of  $-65$  V for  $\text{CF}_4/\text{O}_2$  plasma, while for  $\text{SF}_6/\text{O}_2$  and  $\text{Ar}/\text{SF}_6$  plasma the self-bias voltage was  $-60$  and  $-61$  V, respectively.

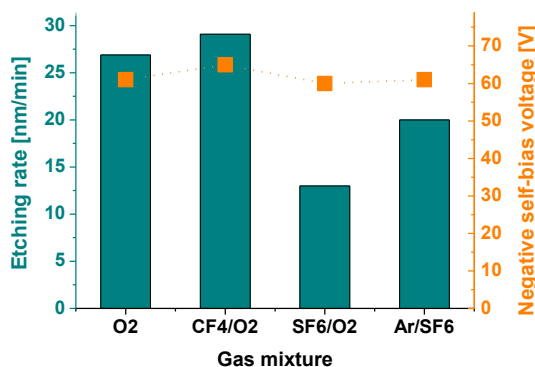


Figure 7.6 Etching rate (columns on the left-side of the y-axis) and negative self-bias voltage (orange rectangles on the right-side of the y-axis) as the function of gas mixtures used for the etching of NCD films [277].

The formation of nanowhiskers is not a trivial process. It is often influenced by several sub-effects. First, sharp nanocones or nanowhiskers can be formed due to local inhomogeneities localised either along grain boundaries (as a consequence of the differences in  $sp^2$  vs  $sp^3$  carbon bonds) or they are randomly spread within the grains due to intrinsic defects and impurities. The third kind of whiskers is regularly formed in specific grains which depend on crystallographic orientation [103].

For the MCD film, the primary diamond grains form a basic microscopic pattern. It is known that a higher concentration of  $sp^2$  carbon atoms is preferentially localised at grain boundaries [280]. Taking into account the fact that oxygen etches  $sp^2$  carbon bonds much faster than  $sp^3$  carbon bonds, the grains become microscopically visible due to the edges. Similar selectivity in etching of  $sp^2/sp^3$  bonds was observed for atomic hydrogen [31].

The decrease of whisker features with increasing concentration of  $CF_4$  in  $O_2$  plasma can be attributed to the lateral etching of diamond by  $CF_4$  gas mixtures. Adding even a small amount of  $CF_4$  was found to smooth (polish) the diamond surface [103, 111]. Furthermore,  $CF_4$  makes the diamond surface not only flatter but also increases the etching rate [281]. This is in good agreement with our observation when the etching rate slightly increased from 27 nm/min for the oxygen to 29 nm/min for the  $CF_4/O_2$  gas mixture (Figure 7.6). Combining effects of faster etching and flattening, the individual grains should be homogeneously etched within their whole surface except at grain boundaries. As mentioned above, higher density of  $sp^2$  carbon bonds and defects is assumed at grain boundaries. Thus, these “non-diamond” phases can disturb the lateral etching at grain boundaries, i.e. they are differently etched than diamond bonds.

However, controversial results were observed when 4%  $SF_6$  was added to the  $O_2$  gas. First, the etching rate reached its lowest value (13 nm/min). This observation is a little bit confusing because a more intensive lateral-like etching effect was initially expected. In a previous study [282] it was shown that addition of  $SF_6$  to the  $Ar/O_2$  gas mixture resulted in a flattening of diamond films etched using electron cyclotron resonance plasma. Previous experimental work and theoretical studies predicted that the addition of  $SF_6$  should enhance the etching rate in comparison to the  $CF_4$  gas mixture. This prediction is based on the fact that  $S_xF_y$  is a heavier molecule than  $CF_x$ , so the  $SF_6$  bombardment effect should obviously be more intensive than the  $CF_4$  one. Moreover, when oxygen and sulfur hexafluoride ( $SF_6$ ) are mixed together, oxyfluoride ions ( $OF^-$ ) are formed which further enhanced (accelerated) the diamond etching [278]. However, this prediction is valid only in some cases. The masking material used was found to be an important parameter which influenced the etching rate of diamond. Using  $SiO_2$  and  $Si_3N_4$  masks resulted in an increased etching rate after the addition of  $SF_6$  to the  $O_2$  gas [282]. Compared to this observation, the etching rate was 2–4 times lower for Al, Ti and Au masks. The main origin of these differences is not clear yet, but the author proposed that the co-deposition of nonvolatile compounds on the diamond surface in the latter case

might be involved. Presently we do not know why the etching rate falls down in our case. One noticeable difference in this study is the fact that we used capacitively coupled plasma while the former study used electron cyclotron resonance plasma.

Finally, the addition of Ar (4%) to SF<sub>6</sub> resulted in surface flattening. For Ar plasmas, it is well known that the etching process is enhanced by physical etching (i.e. sputtering) due to surface bombardment by heavy argon ions. Similar observations were reported for diamond etching in H<sub>2</sub>/Ar plasma [107, 276]. In this case, the diamond etching consisted of physical and chemical processes. The former one involved sputtering and graphitisation of the top diamond layer by energetic ions. For this process, ion energy and ion species are the dominant process factors. The latter one was based on the preferential etching of graphitised or amorphous carbon by reactive hydrogen atoms/ions [107]. Depending on the primary structure of diamond film, the process can tend to form conical/whisker structures which have to correlate with the original film structure [283]. It can be assumed that this tendency is significantly influenced or even disturbed by argon bombardment. As the surface nanofeatures are formed the incoming Ar ions can very effectively graphitise these nanofeatures which are suddenly and preferentially removed by the chemical process. Thus, the diamond film is flattened due to the suppression of the perpendicular etching that was observed for O<sub>2</sub> or CF<sub>4</sub>/O<sub>2</sub> plasmas.

The above described experimental results were published in *Advanced Science, Engineering and Medicine* [277].

### 7.3 Structuring of diamond films using MSL: top-down strategy

In this section, top-down (post-growth) structuring of polycrystalline diamond films using the technique of microsphere lithography is presented.

#### 7.3.1 Experimental

Schematic illustration of the main technological steps of the diamond structuring is shown in Figure 7.7.

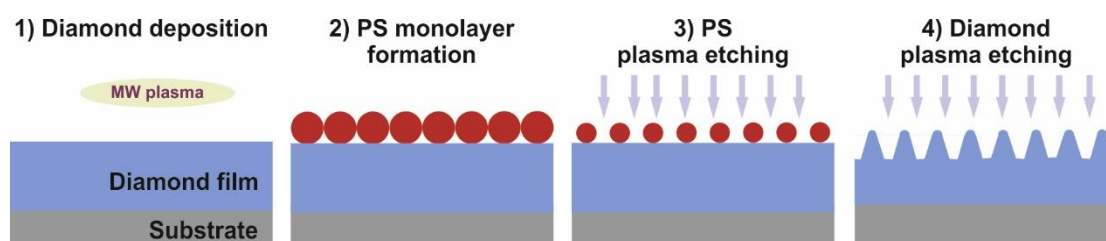


Figure 7.7 Schematic drawing of diamond film structuring using a PS microsphere array [272].



- 1) **Diamond deposition:** Two types of diamond films (MCD and NCD) were grown in a focused plasma CVD system on a  $1 \times 1 \text{ cm}^2$  silicon substrate. SEM, AFM images and Raman spectra of the diamond films are shown in the sections 7.1.1.
- 2) **PS monolayer formation (mask preparation):** A hexagonally close-packed monolayer of PS spheres was achieved at the water-air interface using the standard Langmuir-Blodgett method. The initial diameter of the PS microspheres was  $1.5 \text{ }\mu\text{m}$ . Details of the mask preparation can be found in ref. [284].
- 3) **PS plasma etching (mask modification):** The preparation of the hexagonally close-packed monolayer was followed by its reactive ion etching. The modification of PS microspheres was performed in a CCP-RIE system. The etching parameters were as follows: RF power of 100 W, pressure of 12 Pa,  $\text{O}_2$  flow rate of 50 sccm, etching duration of 7 min, self-bias voltage of  $-57 \text{ V}$ .
- 4) **Diamond plasma etching:** The prepared samples were subsequently treated in the CCP-RIE system again. Two different gas mixtures were used: i) pure  $\text{O}_2$  and ii)  $\text{O}_2$  flow rate 50 sccm (for 2 min) and  $\text{O}_2/\text{CF}_4$  flow rate 40/10 sccm (for 8 min). The other etching parameters were as follows: RF power of 100 W, gas pressure of 12 Pa,  $\text{O}_2$  flow rate of, self-bias voltage of  $-57 \text{ V}$ .  
The plasma parameters for the etching of PS microspheres and diamond films were chosen based on studies described in sections 5.3.1 and 7.2 [142, 277].

### 7.3.2 Results and discussion

The plasma treatment of PS monolayers occurred homogeneously over the whole sample. The close-packed arrays were converted into a non-close-packed template preserving the periodicity ( $1.5 \text{ }\mu\text{m}$ ) of the initial microsphere array [142]. The surface morphology of diamond films after their plasma etching is represented in Figure 7.8.

Hillock-like structures with a period of  $\sim 1.5 \text{ }\mu\text{m}$  were observed. Their height was estimated from AFM images as  $\sim 600$  and  $\sim 800 \text{ nm}$ , for MCD and NCD films, respectively. The fabricated hillock-like features were better recognised (i.e. their geometrical border is better defined) for NCD films. This is attributed to the nanocrystalline character itself. In the case of MCD films, the fabricated structures reveal no sharp edges probably corresponding to the different etching rates for each crystal facet of the diamond. It means that  $\langle 111 \rangle$  facets were etched with different rates than  $\langle 100 \rangle$  oriented diamond crystals, etc. [285]. The MCD film consists of randomly oriented and well-faceted crystals and the surface roughness is higher for thicker films. From this point of view, the NCD film does not reveal such inhomogeneities at the microscopic scales, i.e. grain size and surface roughness does not vary markedly with the film thickness.

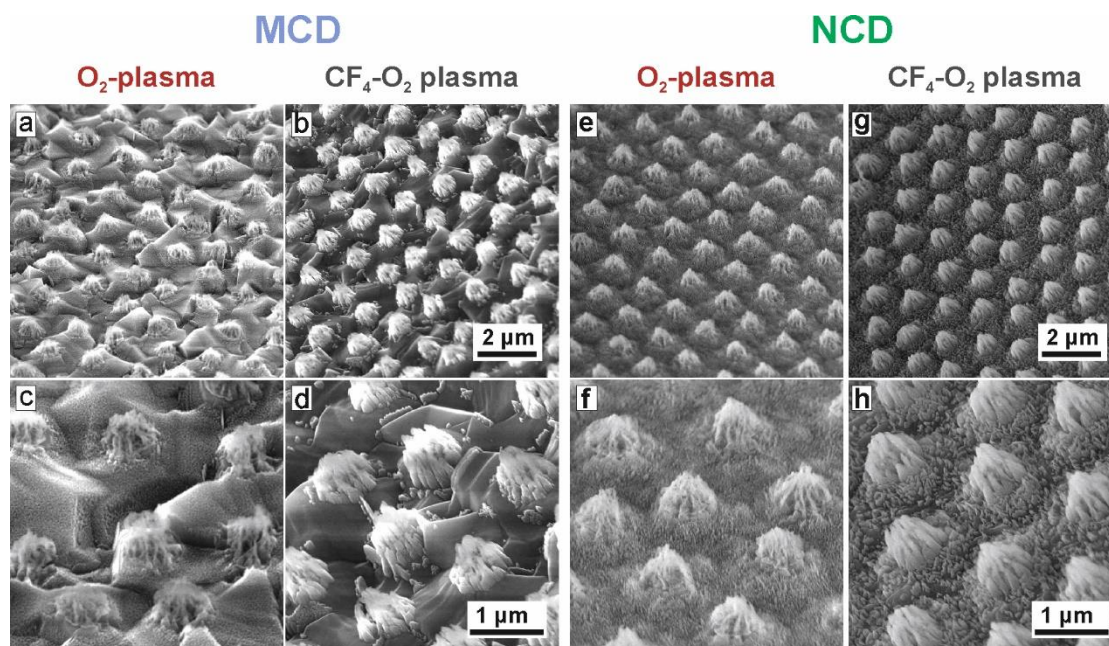


**Figure 7.8** Tilted-angle view (45°) SEM images of etched MCD (columns 1, 2) and NCD (columns 3, 4) diamond films prepared using a PS microsphere (1.5 μm) mask by etching in oxygen plasma (a, c, e, f) and with the addition of CF<sub>4</sub> (b, d, g, h) (bottom row- enlarged images) [272].

The properties of the surface of the etched MCD and NCD films in pure oxygen plasma (columns 1 and 3, Figure 7.8) are in good agreement with our previous studies (see section 7.2) [277]. Reactive ion etching in oxygen plasma led to the formation of needle-like diamond structures (so-called whiskers). The main reason for this effect is that ions are vertically accelerated towards the substrate and besides chemical etching also physical sputtering takes place. Moreover, it is well-known, that oxygen etches sp<sup>2</sup> diamond phases much faster than sp<sup>3</sup> carbon phases [101], resulting in the formation of needle-like structures. In NCD films more sp<sup>2</sup> carbon phases at grain boundaries correspond to the formation of whiskers [286]. The addition of CF<sub>4</sub> into O<sub>2</sub> resulted in the flattening of the diamond surface.

The above-demonstrated fabrication strategy was published in *Acta Polytechnica, Journal of Advanced Engineering* [272].

#### 7.4 Structuring of diamond films using MSL: bottom-up strategy

In this section, the selective deposition of periodically ordered diamond structures films (pre-growth diamond structuring) is demonstrated using the technique of microsphere lithography.

### 7.4.1 Experimental

Figure 7.9 represents the schematic drawing of the selective area deposition of periodically ordered diamond arrays employing a plasma treated seeding layer and structured PS microspheres.

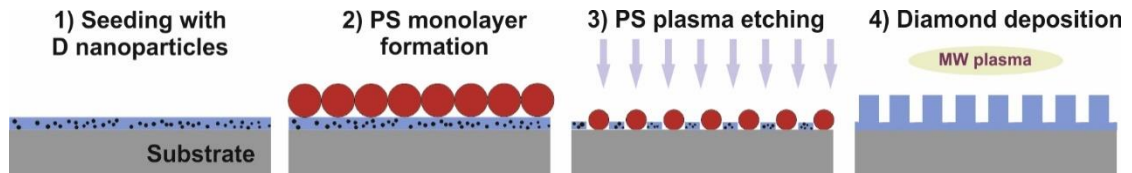


**Figure 7.9** Schematic drawing of selective area deposition of periodic diamond structures [271].

- 1) and 2) **Seeding and PS monolayer formation:** First, silicon substrates were ultrasonically cleaned and seeded. Then, the PS monolayer was deposited on the Si substrates using the Langmuir-Blodgett method [284]. The initial diameter of the PS microspheres was varied: 250, 470 and 940 nm.
- 3) **Plasma etching (mask modification):** Reactive ion plasma treatment was used to i) reduce the initial diameter of the PS microspheres and to ii) remove diamond nanoparticles from the non-masked areas. The plasma treatment was performed in a CCP-RIE system.  
Etching parameters were as follows: oxygen flow rate of 50 sccm, RF power of 100 W, pressure of 12 Pa, self-bias voltage of  $-57$  V. Etching duration: 30 s (for PS of 250 nm), 1 min (for PS 470 nm) and 2 min for PS 940 nm.
- 4) **Diamond deposition:** The diamond deposition was carried out in a focused plasma CVD system at the following process parameters: microwave power of 2500 W, pressure of 4 kPa, gas mixture of 0.5%  $\text{CH}_4$  in  $\text{H}_2$ , substrate temperature of 700–750 °C, deposition duration of 6 h. The low methane concentration was chosen to minimise undesirable spontaneous nucleation (see section 6.1).

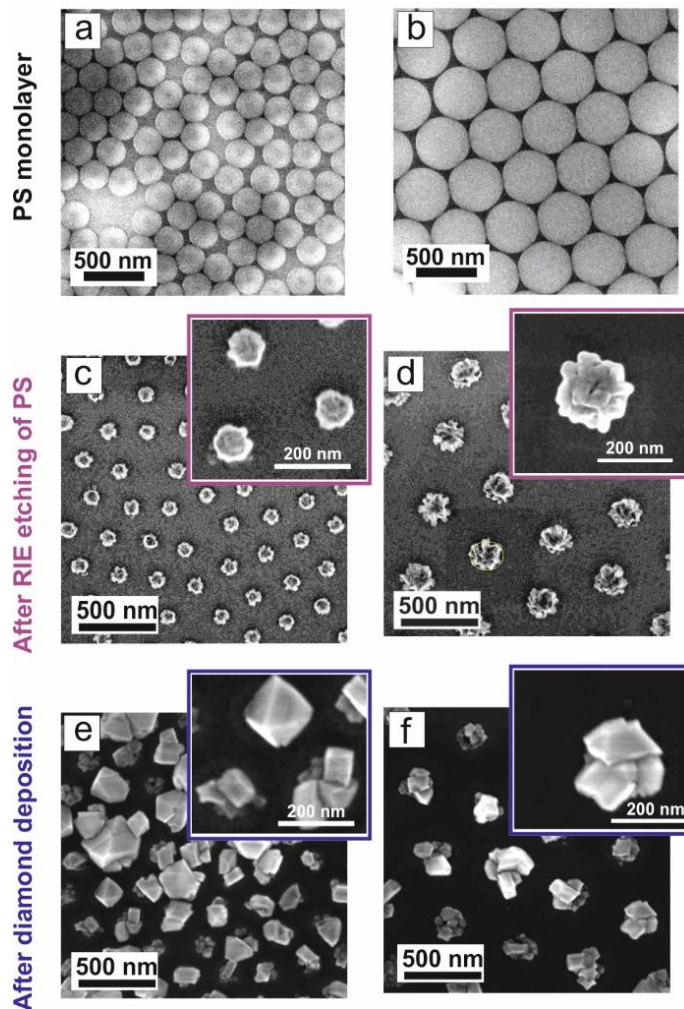
In the second set of experiments, the MW power and pressure was increased to 3 kW and 7 kPa respectively, to obtain higher growth rates. The methane content was raised to 2%  $\text{CH}_4$  in  $\text{H}_2$ . The temperature was  $900 \pm 40$  °C. The deposition time varied from 15 to 150 min. These parameters resulted in the growth of microcrystalline diamond film. In the case of nanocrystalline diamond films, after 5 min of deposition at the same parameters, 1% of  $\text{N}_2$  (the ratio of  $\text{CH}_4/\text{H}_2$  remained the same, i.e. 2%) was added into the gas mixture.

Samples were characterised using scanning electron microscopy, atomic force microscopy and Raman spectroscopy.

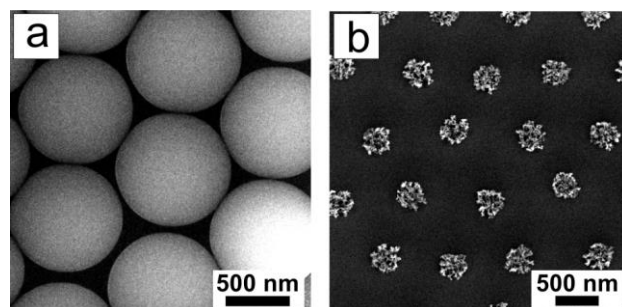
## 7.4.2 Results and discussion

Figure 7.10 shows top view SEM images of the microsphere monolayers after the i) mask preparation, ii) plasma treatment and iii) diamond features after the CVD process. The initial diameter of the PS microspheres was 250 and 470 nm (Figure 7.10 a-b). After the reactive ion plasma treatment (for 30 s and 1 min), the diameter of the spheres decreased to 100 and 220 nm (Figure 7.10 c-d). The CVD process resulted in the growth of periodically ordered features (Figure 7.10 e-f). For PS 250 nm, we observed distortion of array periodicity for some areas. Better periodical order was achieved for the larger PS diameter of 470 nm.

Next, we have tested the suitability of using larger PS spheres and studied the time evolution of diamond growth. Figure 7.11 shows the PS monolayer before and after 2 min of plasma etching. It was clearly observed that the well-ordered PS microspheres with a diameter of 940 nm decreased down to irregular structures 330–350 nm in diameter. The area between these irregular PS structures reveals a featureless surface, i.e. flat silicon surface.



**Figure 7.10** SEM images of monolayers of PS microspheres (left: 250 nm, right: 470 nm) their morphology after plasma treatment and diamond structures after the CVD process [271].



**Figure 7.11** a) SEM images of PS monolayer of microspheres 940 nm in diameter and b) their morphology after 2 min of plasma treatment [271].



For a better understanding of ordered growth, we exposed these substrates to different process parameters to grow either microcrystalline or nanocrystalline diamond structures. Moreover, the process was done for various durations (15–150 min). Figure 7.12 represents evolutions of surface morphologies within a varied duration. After 15 min, the diameter of formed structures varied from 300 to 500 nm and the z-height was up to 110 nm, as detected using AFM measurements. The structures are well-ordered and follow the template from the initial PS microspheres. Further extension of the process duration from 15 to 30 min resulted in an increase of the structures diameter and higher coverage of the substrate surface. For microcrystalline diamond (Figure 7.12c) the crystal faceting is getting evident. Compared to this, larger structures were observed for nanocrystalline growth parameters. The subsequent growth durations slightly differ for the growth of micro- and nanocrystalline diamond structures. An almost fully closed microcrystalline diamond film was found after 150 min (Figure 7.12g). The nanocrystalline diamond film was nearly closed after 120 min (Figure 7.12h). The faster growth of nanodiamond structures is attributed to the changed gas chemistry (1% N<sub>2</sub>).

Raman spectra (Figure 7.13) clearly confirm the diamond character for both films (see sharp peak located at 1332 cm<sup>-1</sup>).

The presented results clearly confirm that the plasma treatment of PS microspheres decreased not only their diameter but also etched the seeding layer, i.e. diamond nanoparticles, from the Si substrate.

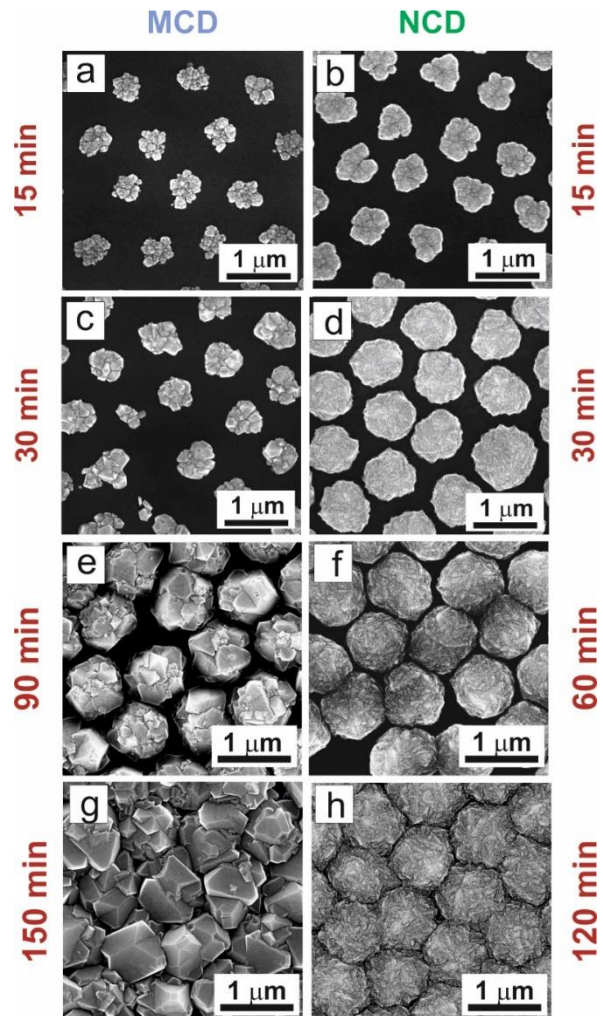


**Figure 7.12 SEM images of microcrystalline and nanocrystalline diamond structures formed after the CVD process [271].**

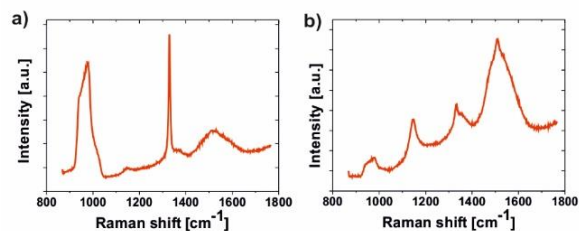


**Figure 7.13 Representative Raman spectra of a) microcrystalline and b) nanocrystalline diamond structures formed after 30 min CVD deposition [271].**

During the CVD process, the PS microspheres are etched away and diamond crystals are formed from the remaining diamond nanoparticles. The diamond structures grew within areas predefined by the primary PS array.

It has been shown in section 6.3 that diamond growth can be initiated by a polymer layer [77, 83] and even transformation from polymer to diamond can be achieved [287]. To understand the role of PS microspheres in diamond growth we realized a set of experiments omitting the seeding step. Figure 7.14 shows the surface morphology of silicon substrates after micro- and nanocrystalline diamond growth for 30 min.

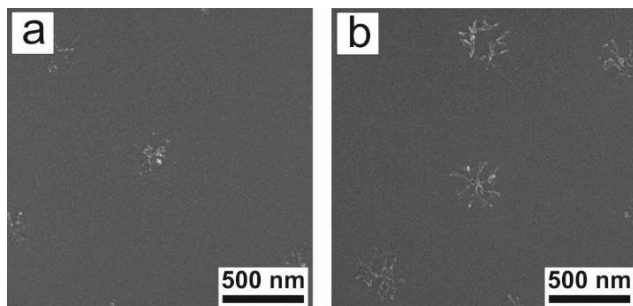


**Figure 7.14 SEM images of reference samples after a) microcrystalline and b) nanocrystalline diamond growth for 30 min. (The seeding step was omitted and the Si substrate was directly covered with a monolayer of PS microspheres (940 nm), plasma treated for 2 min and exposed to appropriate CVD process parameters.) [271]**

In this case, no diamond nanoparticles were spread over the Si substrate. The surface morphology of plasma treated PS (940 nm) is shown in Figure 7.14 after 30 min of growth, we did not observe any development of diamond structure. Only a fingerprint of the remaining PS microspheres was observed. This study implies that we can exclude any significant contribution from the PS microspheres to the diamond growth. The diamond crystal character is primarily

influenced by the gas mixture. In hydrogen-rich plasma, microcrystalline diamond crystals grow. Prolonged deposition time resulted in the enlargement and faceting of crystals. Adding nitrogen to the gas mixture amplifies re-nucleation mechanism leading to the growth of nanocrystalline diamond [14, 288]. In this case, prolonging the deposition duration did not result in the enlargement of diamond crystals. Moreover, no crystal facets were resolvable in our SEM measurements.

Figure 7.15 shows cross-section views of micro- and nanocrystalline diamond structures grown for 150 and 120 min, respectively. In both cases, the growth starts from the remaining diamond nanoparticles on the silicon substrate. These regions are indicated by red lines. For the microcrystalline CVD process, faceted diamond crystals are randomly formed within one structure. During the growth, crystals from one structure start to touch with crystals from the neighbouring structures. This is better recognizable from the top view (Figure 7.12g). It can also be seen that crystal facets also develop on the side of the formed structure. This side crystal faceting partially disturbs the geometrical periodicity. This observation is in good agreement with the van der Drift evolutionary selection growth model [289, 290]. It states that crystals with the highest

growth rate survive. However, this effect will be more observable for closed and thicker diamond films.

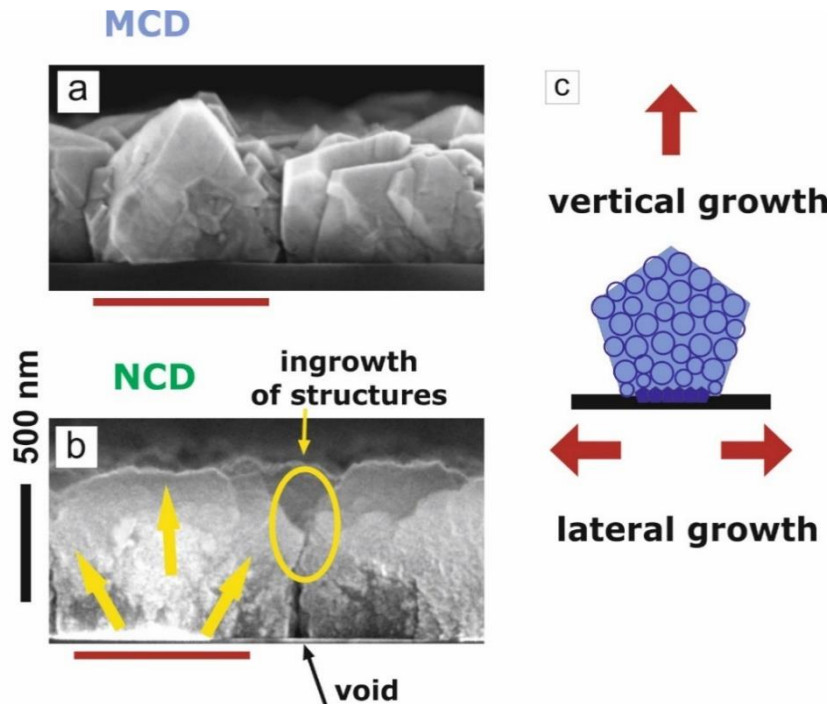


**Figure 7.15** Cross-section view of a) microcrystalline and b) nanocrystalline diamond structures formed after 150 and 120 min CVD process. The initial diameter of the PS microspheres was 940 nm which were plasma treated for 2 min. c) Schematic illustration of growth mechanism [271].

In the case of nanocrystalline diamond growth, only clustered structures consisting of small crystals were observed. As in the previous case, the structure grows in the vertical and lateral direction as indicated by the yellow arrows in Figure 7.15b. After a certain duration, in our case 120 min, the structures start to touch. After the ingrowth of neighbouring structures, only the vertical growth will continue. In this growth type, voids are naturally formed at the substrate side (Figure 7.15b). From a geometrical point of view, nanocrystalline growth follows the initial template created by PS microspheres better. The achieved aspect ratio defined as vertical growth to lateral growth was close to 1:1. This way, we are able to selectively grow diamond structures up to the height of 1  $\mu\text{m}$ . It is expected, that optimising this technology will further increase the aspect ratio.

The results about fabrication of photonic crystals using microsphere lithography were published in *Physica Status Solidi (b)* [271].

## 7.5 Conclusion

In summary, structuring of diamond film was demonstrated: i) without a mask using reactive ion plasma etching and ii) with self-assembled masks using the technique of microsphere lithography.



First, two types of diamond were grown in a focused plasma CVD system, and their morphology was controlled by the used gas mixture. The microcrystalline diamond films (large, well-faceted crystals 400 to 600 nm in size) were grown from a  $\text{CO}_2 + \text{CH}_4 + \text{H}_2$  gas mixture while nanocrystalline diamond films (grains < 50 nm) were grown from a  $\text{N}_2 + \text{CF}_4 + \text{H}_2$  gas mixture.

First, the surface structuring was carried out in a CCP-RIE plasma system without a mask. Four different gas mixtures were used for etching the diamond films (pure oxygen plasma, 4% of  $\text{CF}_4$  in  $\text{O}_2$ , 4% of  $\text{SF}_6$  in  $\text{O}_2$  and 4% of Ar in  $\text{SF}_6$ ). It was found that pure oxygen and oxygen with a small amount of  $\text{SF}_6$  lead to the formation of homogeneously distributed needle-like structures. The  $\text{CF}_4/\text{O}_2$  and Ar/ $\text{SF}_6$  gas mixtures, however, resulted in surface flattening due to the suppression of the perpendicular etching.

These results (influence of gas mixture, etching rate) were useful in the fabrication of diamond nanostructures using the technique of MSL. First, a top-down strategy was demonstrated. A self-assembled, hexagonally closed-packed PS microsphere array was used as the masking material. The PS monolayer was treated in plasma to predefine the final geometry of diamond structures. During the subsequent plasma etching (pure oxygen,  $\text{CF}_4/\text{O}_2$  gas mixture), the primary PS mask was removed and hillock-like structures with a period of  $\sim 1.5 \mu\text{m}$  were achieved for both MCD and NCD films.

Next, a bottom-up strategy was demonstrated, i.e. diamond nanostructures were grown from pre-defined periodic arrays using a microwave plasma CVD process. Ultrasonically seeded silicon substrates were covered with a PS self-assembled monolayer, which was then plasma treated. The plasma treatment was used not only for structuring the PS microspheres but also for removing the seeding layer. The etching process duration was chosen with regard to the desired periodic structures, i.e. final diameter of the PS microspheres and gap between them. Based on the results achieved with the non-seeded samples we proposed that the PS microspheres do not play any significant role in the diamond growth. Diamond structures grew according to the process parameters used, while vertical growth slightly dominated over lateral one. Arrays of nanocrystalline diamond showed better periodicity than arrays of microcrystalline diamond. This can be related to the different growth mechanisms.

We have demonstrated that microsphere lithography is a promising technique for the structuring of diamond thin films. The presented fabrication setups represent a simple and cheap way of diamond film plasma etching and selective area deposition of periodically ordered diamond structures. It is believed that such diamond structures fabricated over large areas will find application in various fields such as sensorics, biomedicine, electrochemistry, optics (see Chapter 8), etc. [291, 292].

## 8. Fabrication of a diamond photonic crystal using MSL

In this chapter, the fabrication of a diamond-based photonic crystal (PhC) with hexagonal lattice on a quartz substrate is presented using microsphere lithography. We extend the applicability of spin-coating to rough polycrystalline diamond film and discuss the fabrication challenges especially focusing on the diamond film surface roughness and PS microspheres diameter. The desired dimensions of the structure are given by computer simulations. Finally, we compare the simulated and measured transmission spectra of the fabricated diamond-based PhC tuned for extraction/coupling of the 1.31  $\mu\text{m}$  wavelength.

### 8.1 Experimental

#### 8.1.1 Spin-coating on rough polycrystalline diamond films

First, several experiments were performed to demonstrate the applicability of spin-coating on polycrystalline diamond films with various morphological properties. In this case, the high diamond film surface roughness is the main obstacle to achieve a high quality hexagonal close-packed monolayer mask.

Three series (labelled as A, B and C) of diamond thin films were deposited with varying growth durations (1, 6 and 12 h) in focused plasma CVD system. The other growth parameters were as follows: MW power 3 kW, pressure 6 kPa, 1%  $\text{CH}_4$  in  $\text{H}_2$ , temperature 750  $^\circ\text{C}$ . Next, monolayers of PS spheres (with diameters of 0.5 and 1  $\mu\text{m}$ ) were created on diamond films using spin-coating technique with optimised process variables. Besides these, dispersion with a very low concentration of PS spheres was drop-casted onto other diamond films to compare the size of the spheres and diamond grains.

#### 8.1.2 Diamond photonic crystal design and fabrication

##### 8.1.2.1 PhC design and simulation

A two-dimensional diamond-based air-hole-type PhC on a quartz substrate with hexagonal lattice symmetry was designed. The desired dimensions of the PhC, i.e. thickness of diamond film ( $h$ ), lattice constant ( $a$ ), diameter ( $d$ ), and depth of holes ( $w_h$ ), were estimated by simulations using rigorous-coupled wave-analysis (RCWA) technique implemented in software RSoft DiffractMOD.

### 8.1.2.2 PhC fabrication

The proposed PhC was fabricated through seven technological steps. Their schematic illustration is shown in Figure 8.1. The desired dimensions of the structure were chosen based on the results of the simulations.

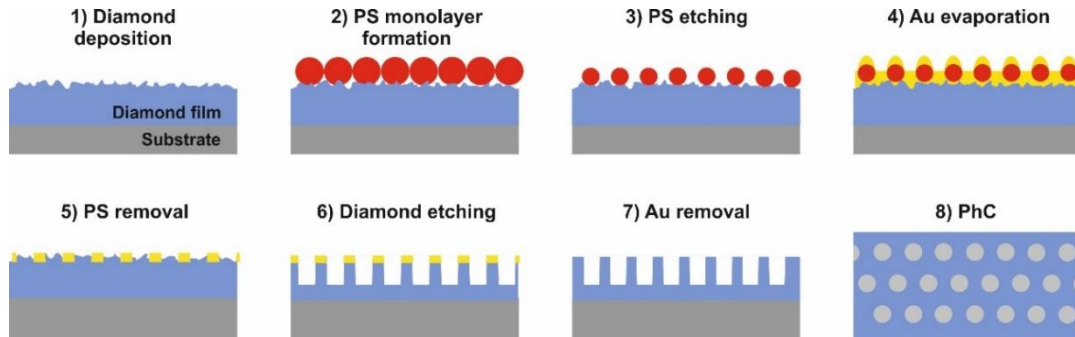


**Figure 8.1 1-7) Sequential schematic cross-sectional drawings of diamond-based photonic crystal fabrication process using microsphere lithography. 8) Schematic top view of the final structure [30].**

- 1) **Diamond nucleation and deposition:** Ultrasonically cleaned mirror-polished quartz (JGS1) of size  $1 \times 1 \text{ cm}^2$  was used as substrate. It was nucleated using ultrasonic seeding with diamond nanoparticles. Polycrystalline diamond film was grown in a focused plasma CVD system. The deposition parameters were as follows: 3 kW, 6 kPa, 1%  $\text{CH}_4$  in  $\text{H}_2$ ,  $750 \text{ }^\circ\text{C}$ , 1 h.
- 2) **PS monolayer formation (mask preparation I):** After the growth process, the diamond film was treated in oxygen plasma to achieve hydrophilic surface. Next, a monolayer of polystyrene microspheres was formed using three-step spin-coating process. The polystyrene particles were purchased from microParticles GmbH as a 10 wt% in dispersion with standard deviation  $\sim 0.03 \text{ }\mu\text{m}$ . The initial diameter of the PS microspheres was  $a = 1080 \text{ nm}$ , which defined the lattice constant of the photonic structure.
- 3) **PS etching (mask modification):** Reactive ion etching was applied to reduce the PS microspheres' initial diameter to the desired one. The modified (i.e. non-close-packed) monolayer acts as a physical mask for further processing. The plasma treatment was performed in linear antenna plasma system in oxygen plasma (300 W, 100 Pa, 100 sccm  $\text{O}_2$ , 20 min).
- 4) **Au evaporation (mask preparation II):** Thin Au film (60 nm) was evaporated onto the modified sphere array.
- 5) **PS removal:** After gold deposition, the PS mask was removed by caution ultrasonication in toluene.
- 6) **Diamond etching:** The air holes in diamond films were created using RF plasma etching (Plasmalab System 100, Oxford Plasma Technology). The holes depth was determined by process parameters:  $\text{O}_2:\text{CF}_4 = 45:2$ , 100 W, 7 Pa, 10 min.
- 7) **Au removal:** The final diamond PhC structure was obtained by a chemical etching of the Au film in Potassium Iodide solution.

Samples were characterised using scanning electron microscopy, atomic force microscopy, Raman spectroscopy ( $\lambda = 442$  nm) and reflectance measurements. The transmission measurements were performed at normal incidence to the substrate in the wavelength range of 300–2000 nm using UV/VIS/NIR spectrophotometer (Shimadzu UV-3101PC) at 300 K.

## 8.2 Results and discussion

### 8.2.1 Spin-coating on rough surfaces

Spin-coating seems to be a promising method to fabricate periodic arrays from PS spheres over large area substrates, specifically with flat surfaces. However, in the case of rough surfaces, the diameter of the spheres has to be appropriately chosen. To investigate the essential issues of spin-coating on rough surfaces, polycrystalline diamond films were deposited with various deposition duration (1, 6 and 12 h). Their surface morphology was characterised using SEM (Figure 8.2, row 1) and AFM measurements (not shown here). The evaluated data are summarised in Table 8.1.

**Table 8.1 Properties of diamond films and PS spheres [30].**

Sample Name	Diamond film						Spheres
	Deposition duration [h]	Thickness [nm]	Grain size [nm]	RMS [nm]	Peak-to-valley roughness [nm]	PTV description	Diameter [ $\mu\text{m}$ ]
A0.5	1	~ 100	< 100	15	~ 50	low	0.5
A1							1
B0.5	6	~ 550	~ 500	35	~ 280	medium	0.5
B1							1
C0.5	12	~ 1100	> 800	60	~ 500	high	0.5
C1							1

The diamond films with varying thickness exhibit grains of varying size having pyramidal, terrace-like and twinned shapes. Increasing the film thickness (i.e. enlarging the well-faceted grains) influences the peak-to-valley (PTV) value (10 $\times$  increased) more markedly than the standardly used surface RMS roughness (4 $\times$  increased). Thus, the PTV value of the rough surfaces is more important factor for the MSL technique when choosing the appropriate sphere size. Taking into account the highest observed PTV value (~ 500 nm for sample C) of the diamond films and the required hole diameter of the PhCs (> 400 nm) for IR region, two different sphere diameters were used, i.e. comparable to the PTV value (~ 0.5  $\mu\text{m}$ ) and approximately two times larger (~ 1  $\mu\text{m}$ ). First, these spheres were drop-casted onto the diamond films to demonstrate the size difference between the diamond grains and the diameter of the spheres (Figure 8.2, rows 2 and 3). It should be noted that differently magnified SEM images were chosen to better illustrate their size ratio.

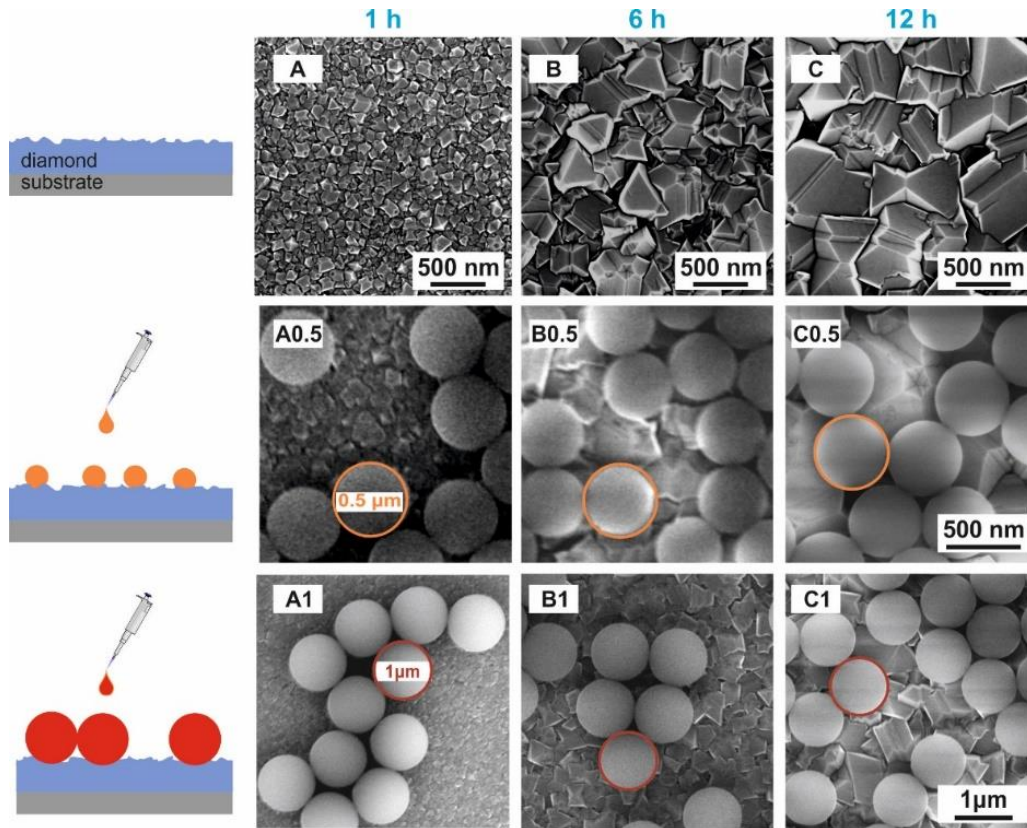


**Figure 8.2** SEM images of diamond films having various surface roughness without (row 1) and with drop-casted PS spheres (0.5  $\mu\text{m}$  – row 2 and 1  $\mu\text{m}$  – row 3) [30].

Second, the diamond films were covered by compact monolayers of spin-coated PS spheres (Figure 8.3). The diamond film with low PTV (sample A) was smooth enough to be coated by a monolayer of hexagonal close-packed spheres with both diameters 0.5  $\mu\text{m}$  (Figure 8.3, sample A0.5) and 1  $\mu\text{m}$  (Figure 8.3, sample A1). Compact PS monolayers were also achieved for sample B with a medium PTV. However, larger diamond grains already interrupted the hcp symmetry of the 0.5  $\mu\text{m}$  sphere array and PS monolayer was split into smaller fractions (Figure 8.3, sample B0.5). Using the four times larger spheres (1  $\mu\text{m}$ ) than the PTV of the diamond film (280 nm) still led to a close-packed monolayer (Figure 8.3, sample B1). However, the spheres were already not in the same z-plane because they followed the surface roughness of the diamond film. In the case of the diamond film with the highest PTV (sample C), a non-compact arrangement of the spheres was observed (Figure 8.3 sample C0.5 and C1). The small spheres (0.5  $\mu\text{m}$ ) fall down from the large facets ( $> 800$  nm) and fill the space among the diamond grains. The monolayer of the large spheres (1  $\mu\text{m}$ ) involved many defects. Such highly disordered arrays are already not suitable for the fabrication of PhCs, which require ordered structures. However, it is important to note that such arrays can still be useful, e.g. for fabrication of photonic glass [23] and other nanohole-based disordered nanostructures for biosensors [293], plasmonics [294] or advanced light trapping in thin solar cells [295].

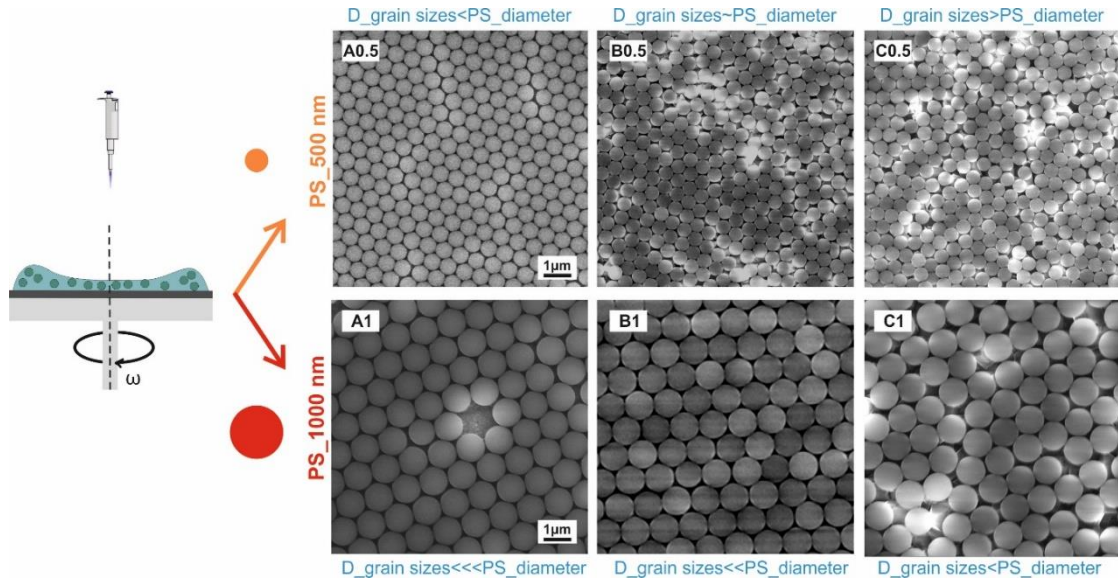


**Figure 8.3 SEM images of spin-coated monolayers of PS spheres (with diameter 0.5 and 1  $\mu\text{m}$ ) on diamond films with varying surface roughness [30].**

## 8.2.2 Fabrication of diamond photonic crystal

### 8.2.2.1 Design and simulation

As demonstrated above, the MSL technique using PS spheres in the range of 0.5–1  $\mu\text{m}$  is suitable for fabrication of periodic structures on rough diamond surfaces with PTV up to  $\sim 300$  nm. The thickness of the diamond film deposited on quartz substrate has to be  $> 100$  nm to achieve a high-quality fully closed diamond film. However, the different thermal expansion coefficients between diamond and quartz need to be taken into account as well. Diamond film thickness has to be  $< 400$  nm to avoid the diamond film cracking or peeling off during the post-deposition cooling process. Within this thickness range (100–400 nm) the diamond film PTV is standardly below 300 nm. In this meaning, all the demands for the realisation of the diamond PhC on quartz substrate working in the NIR region are fulfilled. As an example, a diamond PhC tuned for the extraction/coupling of 1.31  $\mu\text{m}$  wavelength (2<sup>nd</sup> telecommunication window) was fabricated.

The cross-sectional sketch of the air-hole type diamond PhC with hexagonal lattice on quartz substrate is shown in Figure 8.4b. In order to simplify the optical characterisation of the fabricated structures, the waveguides were designed to support only a fundamental TE mode at 1.31  $\mu\text{m}$ . The lattice constant  $a$  was chosen to be 1  $\mu\text{m}$  (based on the results reported in Section 8.2.1), the exact value  $a = 1080$  nm was dictated by the available polystyrene spheres. The hole diameter was  $d = 750$  nm. As a refractive index, a dispersion of a bulk diamond from index database (considering no optical losses) was used. The hole depth was set to be equal to the thickness of the diamond film (i.e.  $w_h = h$ ).



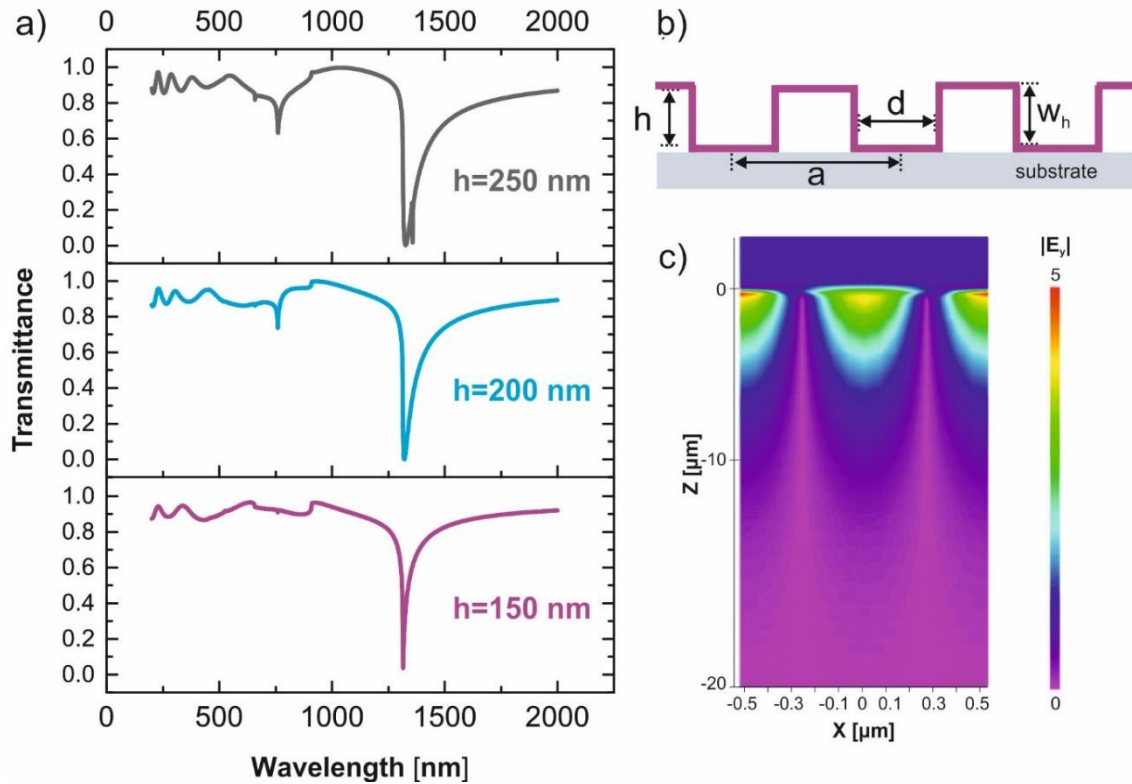


**Figure 8.4 a) Simulated transmission spectra of the PhC structure for different thicknesses of the diamond film: 250, 200, 150 nm. b) Schematic cross-section of the simulated PhC ( $h$  – diamond film thickness,  $a$  – lattice constant,  $d$  – diameter of holes, and  $w_h$  – depth of holes), c) Amplitude of the  $E_y$  electric field component of the vertically extracted TE leaky mode having vacuum wavelength of 1.31  $\mu\text{m}$  for the PhC with  $h = 200$  nm (XZ cross-section of the RCWA computational cell) [30].**

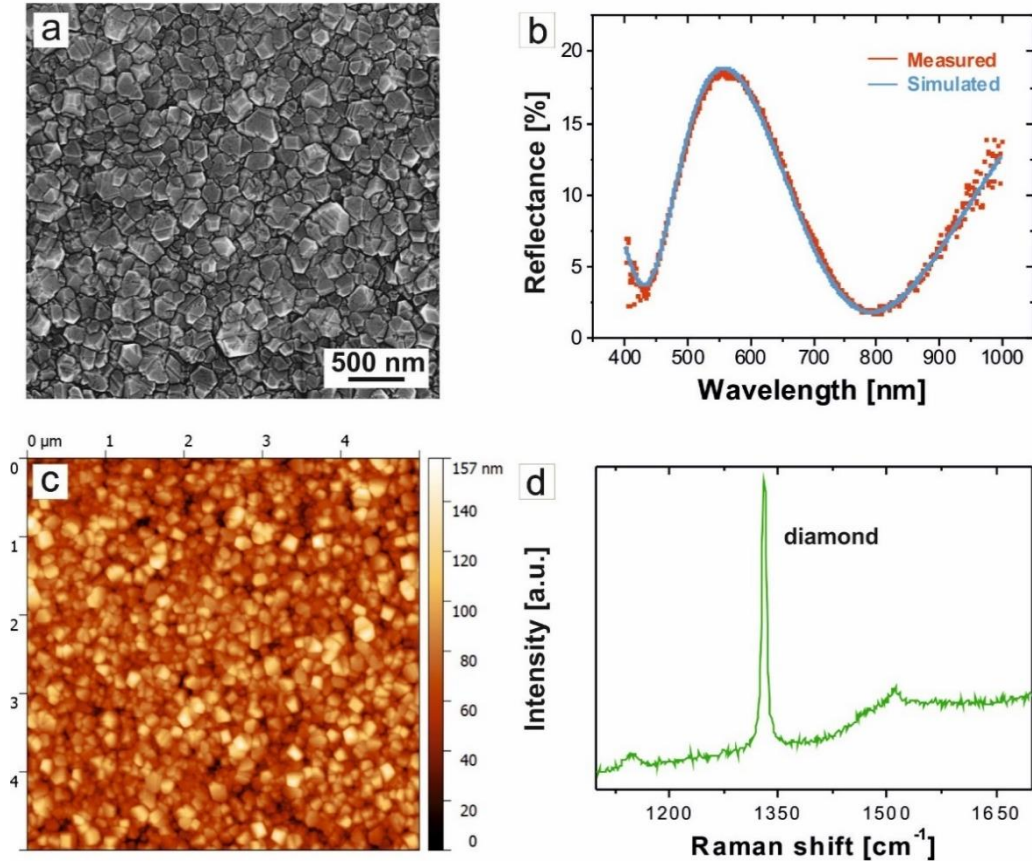
Figure 8.4a compares simulated transmission spectra of the PhC structure for different thicknesses of the diamond film. These simulations indicate that increasing the film thickness from 150 to 250 nm only negligibly shifts the spectral position of the leaky mode at 1.31  $\mu\text{m}$ . This was a useful finding because the technological control over the diamond thickness was not so crucial. What changes with the diamond layer thickness is only the spectral width of the leaky resonance, i.e. it gets slightly narrower by decreasing the thickness (Figure 8.4a) until it disappears for very thin layers (below approximately 80 nm). Finally, we would like to note that the resonance at around 750 nm, present in the transmission spectra plotted in Figure 4a, is a higher order leaky mode with much lower coupling efficiency than the leaky mode with the wavelength of 1.31  $\mu\text{m}$ .

Figure 8.4c shows the electric field distribution of the vertical TE leaky mode (at 1.31  $\mu\text{m}$ ) within the structure with  $h = 200$  nm. Due to the relatively large wavelength with respect to the thickness of the film, the mode spans largely into the quartz substrate. This also means that the mode is less sensitive to the losses inside the diamond film.



### 8.2.2.2 Fabrication process

The surface morphology and topography (SEM and AFM images) of the as-grown fully closed 150 nm thick polycrystalline diamond film is shown in Figure 8.5a-c. The film thickness was determined by curve fitting of the measured reflectance spectrum (Figure 8.5b). The average diamond grain size was in the range of 150–200 nm with a PTV value of  $\sim 157$  nm.



**Figure 8.5** a) Top view SEM image, b) Reflectance spectrum (measured and simulated), c) AFM image ( $5 \times 5 \mu\text{m}^2$ ) and d) Raman spectrum of the deposited polycrystalline diamond thin film on quartz substrate [30].

The Raman spectrum (Figure 8.5d) is dominated by a sharp peak located at  $1332 \text{ cm}^{-1}$  which is the characteristic line for the diamond phase ( $\text{sp}^3$  hybridisation).

Figure 8.6a reveals that the optimised spin-coating process resulted in self-assembly of PS microspheres to the compact monolayer with hexagonal close-packed ordering. After employing the isotropic etching process, the initial diameter of the spheres was reduced to 750 nm without sphere distortion and translation, which led to a non-close-packed PS array.

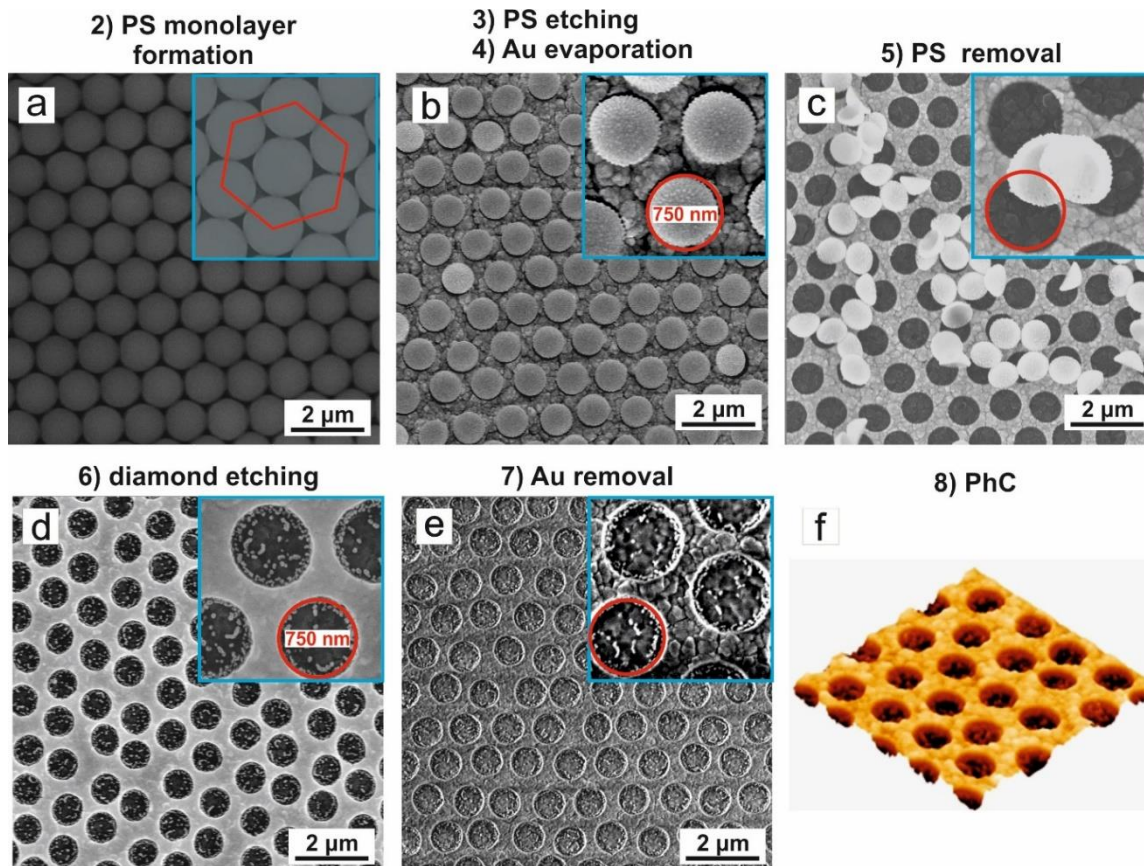


**Figure 8.6 Monolayer of polystyrene microspheres (1080 nm) a) on diamond film, b) after plasma etching and Au evaporation and c) during removal of PS mask. Array of holes in diamond film d) after plasma etching of diamond and e) after removal of Au mask. f) AFM image ( $5 \times 5 \mu\text{m}^2$ ) of the final diamond-based photonic structure [30].**

Figure 8.6b shows the decreased PS spheres after Au evaporation. Next images represent sample during PS removal (Figure 8.6c), after diamond plasma etching (Figure 8.6d) and Au mask removal (Figure 8.6e). Process steps like metal evaporation, lift-off, plasma and chemical etching were previously optimised and successfully used for fabrication of diamond PhC structures using EBL on small areas [8]. The outputs resulting from with the combination of MSL technique allowed us to fabricate diamond PhCs over large areas with sufficient control over the size (i.e. diameter and depth) and the shape of the holes according to the fabrication design. The AFM image of the final hexagonal air-hole-type PhC structure is shown in Figure 8.6f.

### 8.2.3 Transmission measurements

In order to examine the optical properties of the fabricated diamond-based 2D photonic structure, transmittance measurements at a normal angle of incidence were performed. Figure 8.7a compares a measured transmission spectrum to the simulated one.

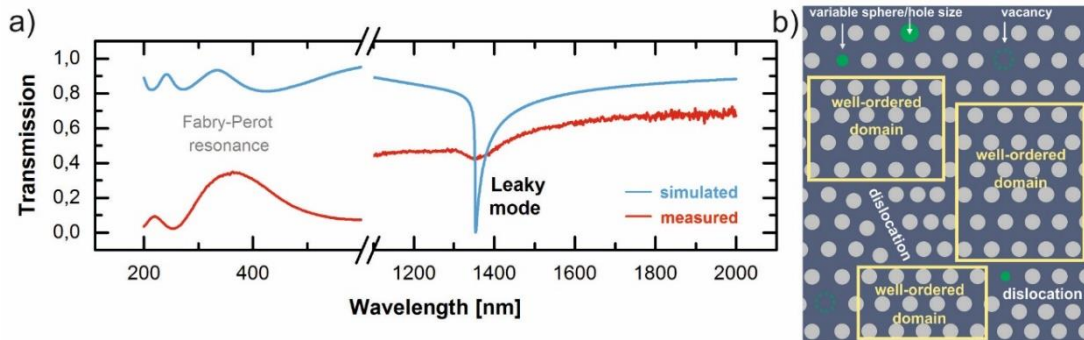


**Figure 8.7** a) Simulated and measured transmission spectra of the final polycrystalline diamond-based photonic structure. b) Illustration of the ordered and disordered domains in the PhC [30].

The simulated spectrum was obtained by tuning the input structure parameters to achieve the best agreement with the measured transmission spectrum. The PhC parameters used in the simulation are:  $a = 1080$  nm,  $h = w_h = 150$  nm,  $d = 750$  nm. In the short wavelength part (200–600 nm) of the spectra, broad peaks are visible due to Fabry-Perot resonances inside the thin diamond film. The small mismatch in the period of the oscillations is attributed to the surface roughness of the diamond film (neglected in the simulations). However, the measured leaky mode position agrees well with the position of the leaky mode in the simulated spectrum. The main difference between the two spectra is the absolute value of the transmission efficiency. The minimum of the measured leaky mode (at 1352 nm) is much shallower than the deep minimum in the simulated spectra. Furthermore, the full width at half maximum (FWHM) of the simulated leaky mode is about  $13$   $\text{cm}^{-1}$ . In case of the measured sample, the observed leaky mode is five times broader (FWHM =  $65$   $\text{cm}^{-1}$ ). These differences between the real and the simulated sample could be caused by i) optical losses (scattering, absorption) present in the real sample and ii) not perfect periodicity of the photonic structure due to the disorder in the PS monolayer mask. Based on our experience with polycrystalline diamond PhCs having similar optical properties as those studied here, but fabricated by the combination of electron beam lithography and reactive ion etching, the latter reason seems to be the more relevant. Narrower and deeper leaky modes were obtained for nearly perfectly uniform diamond PhC lattice produced using EBL and RIE [8, 296]. It should also be noted that the measured position of the leaky mode minimum is slightly red-shifted to the value of 1352 nm compared to the originally designed one (1310 nm) which we also attribute to the observed disorder in the lattice periodicity.

The PS spheres size variations and the self-assembly process resulted in some local defects (such as vacancies, dislocations, and variable hole sizes) which led to a not perfectly preserved periodicity over large area (Figure 8.7b). Despite these issues, the transmittance measurements clearly confirmed the functionality of the PhC, since it contains sufficient amount of local domains with well-defined lattice constant.

## 8.2.4 Discussion and future prospects

The experiments described above showed that spin-coating and MSL techniques can be applied on rough diamond films almost as precisely as on polished or flat surfaces [216]. However, it was found that for the formation of highly ordered monolayers over a rough diamond surface, two conditions have to be fulfilled. First, the diamond film must be uniform and homogeneous, since individual diamond grains which are significantly larger than the average grain size will lead to local defect formation within the PS monolayer. Second, it is important to choose the appropriate sphere diameter according to the surface roughness of the films. PS spheres are commercially available from tens of nanometres up to hundreds of micrometres in diameter allowing flexibility in the manufacturing process. Akinoglu et al. [297] reported that the spheres size has to be several times larger than the surface roughness. However, there are many different roughness parameters (root-mean-square, arithmetical mean deviation of the assessed profile, peak-to-valley, etc.) and it is important to specify and take into account the most appropriate one. As we showed, for polycrystalline diamond films, the PTV value is more suitable than the RMS value for choosing the correct sphere diameter for diamond-based periodic structure fabrication. Certainly, diamond films can be grown with varying morphological properties (grain size, shape, and film thickness) and thus with varying PTV roughness. Obviously, ultranano- or nanocrystalline diamond films can be processed more precisely than microcrystalline films [19]. However, the decrease of grain size generally reduces the optical quality of the diamond film [298]. These two features (grain size vs optical quality) also had to be compromised in the fabrication process of diamond-based optical devices (e.g. photonic crystals), especially for highly sought after diamond films/structures with optically active colour centres [9, 299, 300]. It should also be noted that the film (diamond) thickness seems to be not a critical parameter in the design/fabrication of PhCs working at an exact wavelength in the NIR region, i.e. the diamond CVD is allowed some leeway in the film thickness.

Generally, the main issue with MSL is that self-assembly tends to produce structural defects. The presence of some defects (dislocations, vacancies, disordered areas, multilayers, etc.) among microspheres is almost inevitable [301]. This is especially true in the case of rough surfaces - as shown above for the diamond samples B and C (Figure 8.3) – with higher peak-to-valley values. The properties of the monolayer are influenced by several parameters. The first crucial factor affecting the quality of the monolayer is the PS spheres size distribution. The vast amount of spheres that a dispersion contains cannot possibly be perfectly monodisperse in size and shape (typical size deviation is less than 5%). The spheres size variation results in disorder in the hcp lattice due to the additional stress within the monolayer. A single larger or smaller sphere amongst many in an array was enough to give rise to point defects (Figure 8.3A1) [21]. Defect formation can also be attributed to preparation technique. On one hand, spin-coating is easy to use, fast, and cheap [302]. On the other hand, the quality of the monolayer depends on many factors when using

this technique: i) the dispersion parameters (concentration, diameter of spheres, presence of surfactant, deposited volume of dispersion, etc.), ii) the spin-coating process parameters (rotation speed, acceleration and duration) and iii) the sample surface wettability (e.g. atomic surface termination with oxygen (hydrophilic surface) vs hydrogen (hydrophobic surface), etc.) [207, 303]. These parameters need to be tailored for each sphere size and substrate type (i.e. various material and surface roughness).

Another way to create microsphere monolayers is self-assembly at a water-air interface (e.g. Langmuir-Blodgett method). Even this approach could provide a better quality pattern with a lower number of structural defects [304, 305], it also depends on many parameters (e.g. temperature, surface pressure, humidity, deposition speed, etc.) whose optimisation is even more complex and time consuming than that of the spin-coating process.

In general, once the monolayer preparation is optimised, the fabrication process is well reproducible even on large areas [306]. Then, these highly ordered patterns can be further processed to produce a range of nanostructures with different dimensions (lattice constant, diameter of holes/columns). Furthermore, we showed that the ordered spheres templates can be applied also to rough diamond surfaces. The successful employment of MSL on rough diamond films with their unique properties opens the road to the large scale production of highly durable, chemically inert, and biocompatible scalable structures for photonics, plasmonics, sensorics, etc.

### 8.3 Conclusion

We demonstrated the design, simulation, fabrication and characterisation of a 2D diamond photonic crystal. As a proof of concept, a hexagonal array of cylindrical air holes ( $d = 750$  nm) was created in polycrystalline diamond film ( $h = 150$  nm). For fabrication, a dual mask system - self-assembled, hexagonally arranged polystyrene microsphere monolayer and evaporated metal film - were used. Besides these treatments, plasma and chemical etching processes were utilised to create the diamond PhC on macroscopic areas. Due to a small disorder in the lattice periodicity, the position of the leaky mode minimum was red-shifted to the value of 1352 nm but the slight broadening of the mode still covers the required 1310 nm wavelength. The critical issues related to the fabrication process with the consequent deviations between the experimentally measured and the simulated transmittance spectra of diamond PhC were described. We have proven that MSL, as a technologically simple and cheap technique, can generate various size-tuneable periodic structures over a large area even on rough diamond surfaces with respect to the peak-to-valley values of the film.

The results about fabrication of photonic crystals using microsphere lithography were published in journal *Materials & Design* [30].

# **SUMMARY**



## 9. Summary of the thesis

The experimental results presented in this thesis may be divided conceptually into two main parts: i) nucleation and growth, ii) structuring of polycrystalline diamond films.

### *I. Diamond nucleation and growth*

The first half of the experimental part (Chapter 6) was devoted to alternative methods used to initiate diamond nucleation and growth, which, unlike commonly used nucleation methods, are suitable for treating substrates with complex geometry or soft/unstable substrates.

First, spontaneous nucleation and early stages of diamond growth were studied on non-treated (i.e. absence of pre-existing diamond seeds) silicon substrates in a linear antenna microwave plasma system using different deposition parameters (varying duration and hydrogen content in the CH<sub>4</sub>/H<sub>2</sub>/CO<sub>2</sub> gas mixture) (see section 6.1). Simultaneously, the same study was performed on nucleated (ultrasonically seeded in a dispersion of deionised water and ultradispersed detonation diamond powder) silicon substrates. Our results demonstrated that with optimised parameters, spontaneous diamond nucleation with at least  $6 \times 10^8 \text{ cm}^{-2}$  nucleation density can be achieved. Such nucleation density is 4–5 orders of magnitude higher than is typical for non-treated Si substrates in most CVD deposition systems (focused microwave plasma, hot filament). Two orientations of samples were used: i) horizontal (HorS) and ii) vertical (VerS), which confirmed that the system can be routinely utilised for growing diamond on 3D substrates with complex geometry within the range of a few centimetres. However, the scanning electron and atomic force microscope images revealed variation in the topographical properties of samples depending on their orientations and z-position on VerS. Independently of the deposition conditions, the grain size and density (for non-treated samples) and film thickness (for seeded samples) decreased in the downward direction – as the measured position got farther from the plasma source. This was attributed to the varying densities of active species and the temperature decrease in the z-direction. Moreover, for both non-treated and seeded samples, the density and size of diamond grains as well as the diamond film thickness grown on HorS were similar to the size/density/thickness on VerS at the z-position 1 cm higher than the HorS vertical position. The grain population exhibited a polymodal size (width and height) distribution for both the vertical and horizontal orientations, which indirectly indicates that besides the spontaneous heterogeneous nucleation on the substrate surface, homogeneous nucleation in the gaseous phase also contributed to the diamond growth.

These results were utilised for the fabrication of diamond-based porous composite membranes by growing diamond on a porous three-dimensional template in a linear plasma CVD system (section 6.2). The prepared membranes were flexible as well as sufficiently thick and robust to be self-standing. Thus it was demonstrated, that the



utilised approach successfully overcomes common problems associated with porous structures, i.e. mechanical and thermal instability (e.g. brittleness of carbon foams, thermal instability of polymer fibres). Furthermore, diamond-based membranes are promising compared to other types of similar membranes (e.g. polymer-based). For example, they can survive more aggressive conditions (e.g. high working temperatures, hostile chemical environment, radiation). We believe that these porous structures will find applications in various areas such as tissue engineering, filtration, separation, sensorics, etc. In-vitro biocompatibility and bioactivity studies (e.g. Saos-2 cells) are in progress.

Next, great effort was dedicated to developing an innovative, simple and low-cost polymer-based nucleation method, where the polymer serves as a carrier matrix for embedded diamond nanoparticles (DNP) or as a primary carbon source for the transformation of  $sp^2$  to  $sp^3$  phases (see section 6.3). The silicon substrates were coated with three types of polymers: i) polystyrene (PS), ii) polylactic-co-glycolic acid (PLGA) and iii) polyvinyl alcohol (PVA). They were applied in different forms using spin-coating, i.e. microspheres (PS, PLGA), monolayers (PLGA), multilayers (PLGA, PLGA/PS) and composites with embedded diamond nanoparticles (PLGA, PVA). It was shown that thin polymer layers ( $< 250$  nm) or microsphere (diameter of  $\sim 1$   $\mu\text{m}$ ) monolayers did not contribute to the diamond nucleation and growth in a broad window of deposition process parameters. However, using thicker continuous polymer films ( $> 750$  nm) or a combination of thin film/microsphere arrays unambiguously led to homogeneous diamond growth. In the case of PVA/DNP composites, the nucleation density was comparable to standard ultrasonic seeding. In summary, we showed that the optimised polymer-based nucleation process has a high enough nucleation density to be usable for the deposition of fully closed ultrathin diamond coatings ( $< 100$  nm) on mechanically soft, fragile or unstable substrates.

## ***II. Structuring of diamond films***

Since several applications of diamond films require structured surfaces, the second half of the experimental part was devoted to diverse nano- and microfabrication approaches.

First, maskless plasma etching was used to study the effect of etching parameters on the surface morphology of diamond films (section 7.2). It was found, that etching in pure oxygen or oxygen with a small amount of  $\text{SF}_6$  leads to the formation of homogeneously distributed needle-like structures. However, using  $\text{CF}_4$  as the additive makes the diamond surface smoother as a consequence of lateral-like etching. These findings were utilised in the fabrication of diamond structures using the technique of microsphere lithography. MSL was demonstrated as a versatile, promising, low-cost (regarding equipment and operation) and material independent fabrication technique (Chapter 5). Its potential fabrication steps were studied individually, then they were combined to create periodic arrays of nanostructures.

First, a series of experiments was done to produce masks from submicron sized (200–1000 nm) polystyrene spheres using spin-coating. Key process parameters (e.g. spin speed, acceleration and dispersion concentration) were systematically studied and optimised to achieve a close-packed monolayer over large areas. It was shown, that high-quality masks (i.e. with tolerable defect densities) can be quickly formed on large area smooth hydrophilic surfaces. Then the mask preparation using spin-coating was extended to surfaces with various roughness (nano- and microcrystalline diamond films). The advantages (simplicity, low cost, repeatability, etc.) and disadvantages (numerous variables, defect formation, etc.) of the method were also pointed out.

The subsequent steps after the mask preparation were also demonstrated (e.g. plasma etching, deposition of metal or diamond film and lift-off process). Special emphasis was given to the modification of microsphere arrays using plasma etching. A wide variety of geometrical patterns was obtained using two different reactive ion plasma systems: capacitively coupled RF plasma and dual (RF + MW) plasma. We found the appropriate parameters to achieve the desired: i) size, ii) shape (spherical, oblate spheroid, pyramidal, ball-and stick structures) and iii) surface roughness of the polystyrene spheres. The most critical parameters affecting the abovementioned properties are RF power, etching duration and gas mixture.

Next, the acquired experience with MSL was utilised for the structuring of diamond thin films, i.e. the creation of various periodic structures. Both top-down and bottom-up strategies were demonstrated. The top down strategy was used for the preparation of diamond hillock-like structures (section 7.3). A four-step fabrication process was applied: diamond deposition (focused plasma CVD), mask preparation (from PS spheres with an initial diameter of 1.5  $\mu\text{m}$ ), mask modification and plasma etching of diamond using different plasma chemistries.

The selective area deposition of periodically ordered diamond nanostructures was demonstrated using the bottom-up strategy (section 7.4). Ultrasonically seeded silicon substrates were covered with a monolayer of polystyrene microspheres (with an initial diameter of 250, 470 and 940 nm). The self-assembled PS spheres were employed as a mechanical mask for the reactive ion etching of the seeding layer. Diamond columns were successfully grown from the pre-defined arrays using focused plasma CVD.

We have proven that MSL, as a technologically simple and cheap technique, can generate various size-tunable periodic structures. The successful employment of MSL on rough diamond films with their unique properties opens the road to the large-scale fabrication of highly durable and chemically inert scalable structures. We assume that such diamond structures fabricated over large areas will find application in various fields such as sensorics, biomedicine, electrochemistry, optics, etc.

In order to prove this assumption, a diamond-based photonic crystal slab was fabricated using MSL (Chapter 8). A two-dimensional hexagonal array of air holes ( $a = 1080$  nm,  $d = 750$  nm) was created in polycrystalline diamond film

( $h = 150$  nm). The PhC was designed to have a leaky mode in the near-infrared wavelength region at  $1.31 \mu\text{m}$  which is an important telecommunication window. In the fabrication procedure, a monolayer of plasma-treated polystyrene microspheres combined with a metal layer were utilised as masks. The challenges of spin-coating on rough diamond surfaces were discussed in detail. The PS spheres size variations and the self-assembly process resulted in some local defects (such as vacancies, dislocations and variable hole sizes) which led to a not perfectly preserved periodicity over a large area. Consequently, the position of the leaky mode minimum was red-shifted to the value of  $1352$  nm but the slight broadening of the mode still covered the required  $1310$  nm wavelength, which clearly confirmed the functionality of the photonic crystal.

Most of the described results were presented at national and international conferences and published in peer reviewed journals during the doctoral study.

### ***Suggestions for future work***

The findings of this thesis opened new pathways for future research, which should be pursued. Below, a few ideas are given:

#### ***Spontaneous nucleation:***

- plasma diagnostic measurements (e.g. electron temperature, plasma density, atomic hydrogen concentration) during the diamond deposition using the Langmuir probe technique, optical emission spectrometry, etc.
- temperature gradient measurement along the z-axis in the plasma volume (e.g. using thermocouples)
- study of diamond nucleation from a theoretical point of view (to develop a model simulating the processes at the early stages of deposition)

#### ***Polymer-based nucleation:***

- using other types of polymers to initiate diamond nucleation and growth, e.g. polymer spheres, films or fibres made from various materials

#### ***Nanostructuring using microsphere lithography:***

- nanostructure fabrication using masks of bi- and multilayers of spheres
- using spheres i) of various materials (e.g.  $\text{SiO}_2$ , PMMA), ii) beyond the most common size range (200–1000 nm), iii) on different kinds of substrates (e.g. material, surface roughness)
- photonic crystal (array of columns) fabrication using the bottom-up strategy (selective area deposition), based on the results described in section 7.4.
- fabrication of disordered structures (e.g. photonic glass)

#### ***Porous diamond structure fabrication:***

- study of the applicability of membranes in various areas such as tissue engineering, biomedicine (templated cell growth, filtration), civil engineering, sensorics (e.g. gas sensors)

---

## References

1. Inagaki, M. and Kang, F., "Introduction," *Materials Science and Engineering of Carbon: Fundamentals*, Elsevier, ISBN 978-0-12-800858-4: 1–15, 2014, doi:10.1016/B978-0-12-800858-4.00001-2.
2. Hu, M., Bi, N., Li, S., Su, T., Hu, Q., Ma, H., and Jia, X., "Synthesis and characterization of boron and nitrogen co-doped diamond crystals under high pressure and high temperature conditions," *CrystEngComm* 19(31):4571–4575, 2017, doi:10.1039/C7CE00709D.
3. Krueger, A. and Lang, D., "Functionality is key: recent progress in the surface modification of nanodiamond," *Adv. Funct. Mater.* 22(5):890–906, 2012, doi:10.1002/adfm.201102670.
4. Krauss, A.R., Auciello, O., Gruen, D.M., Jayatissa, A., Sumant, A., Tucek, J., Mancini, D.C., Moldovan, N., Erdemir, A., Ersoy, D., Gardos, M.N., Busmann, H.G., Meyer, E.M., and Ding, M.Q., "Ultrananocrystalline diamond thin films for MEMS and moving mechanical assembly devices," *Diam. Relat. Mater.* 10(11):1952–1961, 2001, doi:10.1016/S0925-9635(01)00385-5.
5. Nistor, P.A. and May, P.W., "Diamond thin films: giving biomedical applications a new shine," *J. R. Soc. Interface* 14(134):20170382, 2017, doi:10.1098/rsif.2017.0382.
6. Schroder, T., Mouradian, S.L., Zheng, J., Trusheim, M.E., Walsh, M., Chen, E.H., Li, L., Bayn, I., and Englund, D., "Quantum nanophotonics in diamond," *J. Opt. Soc. Am. B-Opt. Phys.* 33(4):B65–B83, 2016, doi:10.1364/JOSAB.33.000B65.
7. Zaitsev, A.M., "Optical properties of diamond: a data handbook," Springer Science & Business Media, ISBN 978-3-540-66582-3, 2001.
8. Ondič, L., Varga, M., Hruška, K., Fait, J., and Kapusta, P., "Enhanced extraction of silicon-vacancy centers light emission using bottom-up engineered polycrystalline diamond photonic crystal slabs," *ACS Nano* 11(3):2972–2981, 2017, doi:10.1021/acsnano.6b08412.
9. Cajzl, J., Nekvindová, P., Macková, A., Malinský, P., Sedmidubský, D., Hušák, M., Remeš, Z., Varga, M., Kromka, A., Böttger, R., and Oswald, J., "Erbium ion implantation into diamond - measurement and modelling of the crystal structure," *Phys. Chem. Chem. Phys. PCCP* 19(8):6233–6245, 2017, doi:10.1039/c6cp08851a.
10. Gicquel, A., Hassouni, K., Silva, F., and Achard, J., "CVD diamond films: from growth to applications," *Curr. Appl. Phys.* 1(6):479–496, 2001, doi:10.1016/S1567-1739(01)00061-X.
11. Lee, S.-T., Lin, Z., and Jiang, X., "CVD diamond films: nucleation and growth," *Mater. Sci. Eng. R Rep.* 25(4):123–154, 1999, doi:10.1016/S0927-796X(99)00003-0.

12. Wang, C.X. and Yang, G.W., “Thermodynamics of metastable phase nucleation at the nanoscale,” *Mater. Sci. Eng. R Rep.* 49(6):157–202, 2005, doi:10.1016/j.mser.2005.06.002.
13. Singh, J., “Nucleation and growth mechanism of diamond during hot-filament chemical vapour deposition,” *J. Mater. Sci.* 29(10):2761–2766, 1994, doi:10.1007/BF00356830.
14. Williams, O.A., “Nanocrystalline diamond,” *Diam. Relat. Mater.* 20(5–6):621–640, 2011, doi:10.1016/j.diamond.2011.02.015.
15. Prelas, M.A., Popovici, G., and Bigelow, L.K., “Handbook of industrial diamonds and diamond films,” CRC Press, ISBN 978-0-8247-9994-6, 1997.
16. Remes, Z., Kozak, H., Rezek, B., Ukraintsev, E., Babchenko, O., Kromka, A., Girard, H.A., Arnault, J.-C., and Bergonzo, P., “Diamond-coated ATR prism for infrared absorption spectroscopy of surface-modified diamond nanoparticles,” *Appl. Surf. Sci.* 270:411–417, 2013, doi:10.1016/j.apsusc.2013.01.039.
17. Kriele, A., Williams, O.A., Wolfer, M., Hees, J.J., Smirnov, W., and Nebel, C.E., “Formation of nano-pores in nano-crystalline diamond films,” *Chem. Phys. Lett.* 507(4–6):253–259, 2011, doi:10.1016/j.cplett.2011.03.089.
18. Seelmann-Eggebert, M., Meisen, P., Schaudel, F., Koidl, P., Vescan, A., and Leier, H., “Heat-spreading diamond films for GaN-based high-power transistor devices,” *Diam. Relat. Mater.* 10(3–7):744–749, 2001, doi:10.1016/S0925-9635(00)00562-8.
19. Ižák, T., Domonkos, M., Babchenko, O., Varga, M., Rezek, B., Jurka, V., Hruška, K., and Kromka, A., “Technological aspects in fabrication of micro- and nano-sized carbon based features: nanorods, periodical arrays and self-standing membranes,” *J. Electr. Eng.* 66(5):282–286, 2015, doi:10.2478/jee-2015-0046.
20. Wang, C.F., Hanson, R., Awschalom, D.D., Hu, E.L., Feygelson, T., Yang, J., and Butler, J.E., “Fabrication and characterization of two-dimensional photonic crystal microcavities in nanocrystalline diamond,” *Appl. Phys. Lett.* 91(20):201112, 2007, doi:10.1063/1.2813023.
21. Wang, M., ed., “Lithography,” InTech, ISBN 978-953-307-064-3, 2010.
22. Wang, J., Duan, G., Li, Y., Liu, G., and Cai, W., “Wet etching-assisted colloidal lithography: a general strategy toward nanodisk and nanohole arrays on arbitrary substrates,” *ACS Appl. Mater. Interfaces* 6(12):9207–9213, 2014, doi:10.1021/am501326w.
23. Galisteo-Lopez, J.F., Ibisate, M., Sapienza, R., Froufe-Perez, L.S., Blanco, A., and Lopez, C., “Self-assembled photonic structures,” *Adv. Mater.* 23(1):30–69, 2011, doi:10.1002/adma.201000356.
24. Liu, G., Zhou, L., Zhang, G., Li, Y., Chai, L., Fan, Q., and Shao, J., “Fabrication of patterned photonic crystals with brilliant structural colors on fabric substrates using ink-jet printing technology,” *Mater. Des.* 114:10–17, 2017, doi:10.1016/j.matdes.2016.09.102.

25. Liu, G. and Cai, W., “Morphological and structural control of organic monolayer colloidal crystal based on plasma etching and its application in fabrication of ordered gold nanostructured arrays,” *Crystals* 6(10):126, 2016, doi:10.3390/cryst6100126.
26. Zhang, H., Duan, R., Li, F., Tang, Q., and Li, W., “Microscopy evidence of the face-centered cubic arrangement of monodisperse polystyrene nanospheres,” *Mater. Des.* 28(3):1045–1049, 2007, doi:10.1016/j.matdes.2005.09.024.
27. Zhang, J., Li, L., Liu, D., Zhang, J., Hao, Y., and Zhang, W., “Multi-layer and open three-dimensionally ordered macroporous TiO<sub>2</sub>–ZrO<sub>2</sub> composite: diversified design and the comparison of multiple mode photocatalytic performance,” *Mater. Des.* 86:818–828, 2015, doi:10.1016/j.matdes.2015.07.166.
28. Domonkos, M., Izak, T., Stolcova, L., Proska, J., and Kromka, A., “Fabrication of periodically ordered diamond nanostructures by microsphere lithography,” *Phys. Status Solidi B* 251(12):2587–2592, 2014, doi:10.1002/pssb.201451172.
29. Ye, X. and Qi, L., “Two-dimensionally patterned nanostructures based on monolayer colloidal crystals: controllable fabrication, assembly, and applications,” *Nano Today* 6(6):608–631, 2011, doi:10.1016/j.nantod.2011.10.002.
30. Domonkos, M., Varga, M., Ondič, L., Gajdošová, L., and Kromka, A., “Microsphere lithography for scalable polycrystalline diamond-based near-infrared photonic crystals fabrication,” *Mater. Des.* 139:363–371, 2018, doi:10.1016/j.matdes.2017.10.076.
31. Pierson, H.O., “Handbook of carbon, graphite, diamond and fullerenes: properties, processing and applications,” Noyes Publications, Park Ridge, N.J., ISBN 978-0-8155-1339-1, 1993.
32. Krüger, A., “Carbon Materials and Nanotechnology,” John Wiley & Sons, ISBN 978-3-527-62961-9, 2010.
33. Shenderova, O.A., Zhirnov, V.V., and Brenner, D.W., “Carbon nanostructures,” *Crit. Rev. Solid State Mater. Sci.* 27(3–4):227–356, 2002.
34. Brown, T.L., ed., “Chemistry: the central science,” 13. ed, Pearson, Boston, Mass., ISBN 978-0-321-91041-7, 2015.
35. Tiwari, S.K., Kumar, V., Huczko, A., Oraon, R., Adhikari, A.D., and Nayak, G.C., “Magical Allotropes of Carbon: Prospects and Applications,” *Crit. Rev. Solid State Mater. Sci.* 41(4):257–317, 2016, doi:10.1080/10408436.2015.1127206.
36. Diudea, M.V. and Nagy, C.L., eds., “Diamond and Related Nanostructures,” Springer Netherlands, Dordrecht, ISBN 978-94-007-6370-8, 2013.
37. Burchfield, L.A., Fahim, M.A., Wittman, R.S., Delodovici, F., and Manini, N., “Novamene: A new class of carbon allotropes,” *Heliyon* 3(2):e00242, 2017, doi:10.1016/j.heliyon.2017.e00242.
38. Georgakilas, V., Perman, J.A., Tucek, J., and Zboril, R., “Broad family of carbon nanoallotropes: classification, chemistry, and applications of fullerenes, carbon dots,



- nanotubes, graphene, nanodiamonds, and combined superstructures,” *Chem. Rev.* 115(11):4744–4822, 2015, doi:10.1021/cr500304f.
39. May, P.W., “Diamond thin films: a 21st-century material,” *Philos. Trans. R. Soc. Lond. Ser. Math. Phys. Eng. Sci.* 358(1766):473–495, 2000, doi:10.1098/rsta.2000.0542.
  40. Balmer, R.S., Brandon, J.R., Clewes, S.L., Dhillon, H.K., Dodson, J.M., Friel, I., Inglis, P.N., Madgwick, T.D., Markham, M.L., Mollart, T.P., and others, “Chemical vapour deposition synthetic diamond: materials, technology and applications,” *J. Phys. Condens. Matter* 21(36):364221, 2009.
  41. Davis, R.F., “Diamond films and coatings: development, properties, and applications,” Noyes Pub., ISBN 978-0-8155-1323-0, 1993.
  42. Liu, H. and Dandy, D.S., “Diamond chemical vapor deposition: nucleation and early growth stages,” Elsevier, 1996.
  43. West, A.R., “Solid state chemistry and its applications,” Second edition, student edition, John Wiley & Sons, Inc, Chichester, West Sussex, ISBN 978-1-119-94294-8, 2014.
  44. cphased.gif (322×356), <https://www.electronics-cooling.com/wp-content/uploads/2002/02/cphased.gif>, Feb. 2018.
  45. Shenderova, O.A. and Gruen, D.M., eds., “Ultrananocrystalline diamond: synthesis, properties, and applications,” William Andrew Pub, Norwich, N.Y, ISBN 978-0-8155-1524-1, 2006.
  46. Angus, J.C., “Diamond synthesis by chemical vapor deposition: the early years,” *Diam. Relat. Mater.* 49:77–86, 2014, doi:10.1016/j.diamond.2014.08.004.
  47. Izak, T., Babchenko, O., Potocky, S., Remes, Z., Kozak, H., Verveniotis, E., Rezek, B., and Kromka, A., “Chapter 13. Low temperature diamond growth,” in: Williams, O. A., ed., *Nanoscience & Nanotechnology Series*, Royal Society of Chemistry, Cambridge, ISBN 978-1-84973-639-8: 290–342, 2014, doi:10.1039/9781849737616-00290.
  48. Pierson, H.O., “Handbook of chemical vapor deposition,” 2nd ed, Noyes Publications, Norwich, NY, ISBN 978-0-8155-1432-9, 1999.
  49. Schwander, M. and Partes, K., “A review of diamond synthesis by CVD processes,” *Diam. Relat. Mater.* 20(9):1287–1301, 2011, doi:10.1016/j.diamond.2011.08.005.
  50. Dischler, B. and Wild, C., eds., “Low-pressure synthetic diamond,” Springer Berlin Heidelberg, Berlin, Heidelberg, ISBN 978-3-642-71994-3, 1998.
  51. Gracio, J.J., Fan, Q.H., and Madaleno, J.C., “Diamond growth by chemical vapour deposition,” *J. Phys. Appl. Phys.* 43(37):374017, 2010, doi:10.1088/0022-3727/43/37/374017.

52. Bachmann, P.K., Leers, D., and Lydtin, H., "Towards a general concept of diamond chemical vapour deposition," *Diam. Relat. Mater.* 1(1):1–12, 1991, doi:10.1016/0925-9635(91)90005-U.
53. Williams, O.A., ed., "Nanodiamond: RSC," Royal Society of Chemistry, Cambridge, UK, ISBN 978-1-84973-639-8, 2014.
54. Park, J.-H. and Sudarshan, T.S., "Chemical vapor deposition," ASM International, Materials Park, Ohio, ISBN 978-1-61503-224-2, 2001.
55. Petherbridge, J.R., May, P.W., and Ashfold, M.N.R., "Modelling of the gas-phase chemistry in C-H-O gas mixtures for diamond chemical vapour deposition," *J Appl Phys* 89, 2001.
56. McHargue, C.J., Jr, J.B.D., Yacamán, M.J., and Gasga, J.R., "Synthesis and properties of advanced materials," Springer Science & Business Media, ISBN 978-1-4615-6339-6, 2013.
57. Collins, A.T., "Synthetic diamond: Emerging CVD science and technology.," *Chem. Vap. Depos.* 1(1):33–33, 1995, doi:10.1002/cvde.19950010109.
58. Kromka, A., Babchenko, O., Izak, T., Varga, M., Davydova, M., Kratka, M., and Rezek, B., "Diamond films deposited by oxygen-enhanced linear plasma chemistry," *Adv. Sci. Eng. Med.* 5(6):509–514, 2013, doi:10.1166/ase.2013.1331.
59. Nebel, C. and Ristein, J., "Thin-Film Diamond I: (part of the Semiconductors and Semimetals Series)," Academic Press, ISBN 978-0-08-054103-7, 2003.
60. Williams, O.A., Nesladek, M., Daenen, M., Michaelson, S., Hoffman, A., Osawa, E., Haenen, K., and Jackman, R.B., "Growth, electronic properties and applications of nanodiamond," *Diam. Relat. Mater.* 17(7–10):1080–1088, 2008, doi:10.1016/j.diamond.2008.01.103.
61. Das, D. and Singh, R.N., "A review of nucleation, growth and low temperature synthesis of diamond thin films," *Int. Mater. Rev.* 52(1):29–64, 2007, doi:10.1179/174328007X160245.
62. Liu, H. and Dandy, D.S., "Studies on nucleation process in diamond CVD: an overview of recent developments," *Diam. Relat. Mater.* 4(10):1173–1188, 1995, doi:10.1016/0925-9635(96)00297-2.
63. Mahalingam, P., Liu, H., and Dandy, D.S., "A model for the nucleation of diamond clusters on Si(111) substrates," *J. Appl. Phys.* 81(4):1966–1977, 1997, doi:10.1063/1.364053.
64. Kromka, A., Rezek, B., Kalbacova, M., Baresova, V., Zemek, J., Konak, C., and Vanecek, M., "Diamond seeding and growth of hierarchically structured films for tissue engineering," *Adv. Eng. Mater.* 11(7):B71–B76, 2009, doi:10.1002/adem.200800384.
65. Cola, B.A., Karu, R., Cheng, C., Xu, X., and Fisher, T.S., "Influence of bias-enhanced nucleation on thermal conductance through chemical vapor deposited

- diamond films,” *IEEE Trans. Compon. Packag. Technol.* 31(1):46–53, 2008, doi:10.1109/TCAPT.2007.906725.
66. Mandal, S., Thomas, E.L.H., Middleton, C., Gines, L., Griffiths, J.T., Kappers, M.J., Oliver, R.A., Wallis, D.J., Goff, L.E., Lynch, S.A., Kuball, M., and Williams, O.A., “Surface zeta potential and diamond seeding on gallium nitride films,” *ACS Omega* 2(10):7275–7280, 2017, doi:10.1021/acsomega.7b01069.
67. Jaccodine, R.J., “Surface energy of germanium and silicon,” *J. Electrochem. Soc.* 110(6):524, 1963, doi:10.1149/1.2425806.
68. Arnault, J.C. and Girard, H.A., “Chapter 10. Diamond nucleation and seeding techniques: two complementary strategies for the growth of ultra-thin diamond films,” in: Williams, O. A., ed., *RSC Nanoscience & Nanotechnology*, Royal Society of Chemistry, Cambridge, ISBN 978-1-84973-639-8: 221–252, 2014, doi:10.1039/9781849737616-00221.
69. Demuynck, L., Arnault, J.C., Speisser, C., Polini, R., and Le Normand, F., “Mechanisms of CVD diamond nucleation and growth on mechanically scratched and virgin Si(100) surfaces,” *Diam. Relat. Mater.* 6(2–4):235–239, 1997, doi:10.1016/S0925-9635(96)00709-1.
70. Ižák, T., Marton, M., Varga, M., Vojs, M., Veselý, M., Redhammer, R., and Michalka, M., “Bias enhanced nucleation of diamond thin films in a modified HFCVD reactor,” *Vacuum* 84(1):49–52, 2009, doi:10.1016/j.vacuum.2009.04.065.
71. Gsell, S., Schreck, M., Bauer, T., Karl, H., Thorwarth, G., Bergmaier, A., Dollinger, G., and Stritzker, B., “The nucleation centers formed during bias-enhanced nucleation of diamond on iridium: structure and stability,” *Diam. Relat. Mater.* 14(3–7):328–334, 2005, doi:10.1016/j.diamond.2004.10.027.
72. Arnault, J.-C., Saada, S., Michaelson, S., Hangaly, N.K., Akhvlediani, R., and Hoffman, A., “Bias enhanced diamond nucleation onto 3C–SiC(100) surfaces studied by high resolution X-ray photoelectron and high resolution electron energy loss spectroscopies,” *Diam. Relat. Mater.* 17(3):377–382, 2008, doi:10.1016/j.diamond.2008.01.032.
73. Varga, M., Ižák, T., Kromka, A., Veselý, M., Hruška, K., and Michalka, M., “Study of diamond film nucleation by ultrasonic seeding in different solutions,” *Cent. Eur. J. Phys.* 10(1):218–224, 2011, doi:10.2478/s11534-011-0078-4.
74. Chu, Y.-C., Tu, C.-H., Jiang, G., Chang, C., Liu, C., Ting, J.-M., Lee, H.-L., Tzeng, Y., and Auciello, O., “Systematic studies of the nucleation and growth of ultrananocrystalline diamond films on silicon substrates coated with a tungsten layer,” *J. Appl. Phys.* 111(12):124328, 2012, doi:10.1063/1.4729798.
75. Buijnsters, J.G., Vázquez, L., Dreumel, G.W.G. van, Meulen, J.J. ter, Enkevort, W.J.P. van, and Celis, J.P., “Enhancement of the nucleation of smooth and dense nanocrystalline diamond films by using molybdenum seed layers,” *J. Appl. Phys.* 108(10):103514, 2010, doi:10.1063/1.3506525.

76. Thomas, E.L.H., Mandal, S., Ashek-I-Ahmed, Macdonald, J.E., Dane, T.G., Rawle, J., Cheng, C.-L., and Williams, O.A., "Spectroscopic ellipsometry of nanocrystalline diamond film growth," *ACS Omega* 2(10):6715–6727, 2017, doi:10.1021/acsomega.7b00866.
77. Domonkos, M., Ižák, T., Kromka, A., and Varga, M., "Polymer-based nucleation for chemical vapour deposition of diamond," *J. Appl. Polym. Sci.* 133(29), 2016, doi:10.1002/app.43688.
78. Babchenko, O., Remes, Z., Izak, T., Rezek, B., and Kromka, A., "Deposition of nanocrystalline diamond films on temperature sensitive substrates for infrared reflectance spectroscopy," *Phys. Status Solidi B* 248(11):2736–2739, 2011, doi:10.1002/pssb.201100119.
79. Kromka, A., Babchenko, O., Potocky, S., Rezek, B., Sveshnikov, A., Demo, P., Izak, T., and Varga, M., "Chapter 9 - Diamond nucleation and seeding techniques for tissue regeneration," in: Narayan, R., ed., *Diamond-Based Materials for Biomedical Applications*, Woodhead Publishing, ISBN 978-0-85709-340-0: 206–255, 2013.
80. Monteiro, O.R. and Liu, H., "Nucleation and growth of CVD diamond films on patterned substrates," *Diam. Relat. Mater.* 12(8):1357–1361, 2003, doi:10.1016/S0925-9635(03)00106-7.
81. Domonkos, M., Ižák, T., Varga, M., Potocký, Š., Demo, P., and Kromka, A., "Diamond nucleation and growth on horizontally and vertically aligned Si substrates at low pressure in a linear antenna microwave plasma system," *Diam. Relat. Mater.* 82:41–49, 2018, doi:10.1016/j.diamond.2017.12.018.
82. Scorsone, E., Saada, S., Arnault, J.C., and Bergonzo, P., "Enhanced control of diamond nanoparticle seeding using a polymer matrix," *J. Appl. Phys.* 106(1):014908, 2009, doi:10.1063/1.3153118.
83. Kromka, A., Potocky, S., Rezek, B., Babchenko, O., Kozak, H., Vanecek, M., and Michalka, M., "Role of polymers in CVD growth of nanocrystalline diamond films on foreign substrates," *Phys. Status Solidi B* 246(11–12):2654–2657, 2009, doi:10.1002/pssb.200982272.
84. Kromka, A., Babchenko, O., Kozak, H., Hruska, K., Rezek, B., Ledinsky, M., Potmesil, J., Michalka, M., and Vanecek, M., "Seeding of polymer substrates for nanocrystalline diamond film growth," *Diam. Relat. Mater.* 18(5–8):734–739, 2009, doi:10.1016/j.diamond.2009.01.023.
85. Sun, Z., Shi, X., Tay, B.K., Wang, X., Zheng, Z., and Sun, Y., "Low pressure polymer precursor for synthesis of diamond at low temperature," *J. Mater. Sci. Lett.* 16(11):933–935, 1997, doi:10.1023/A:1018504608907.
86. Nur, Y., Duygulu, Ş., Pitcher, M.W., and Toppare, L., "The electrochemical synthesis of poly(methylcarbyne) for diamond film coatings," *J. Appl. Polym. Sci.* 124(5):3626–3632, 2012, doi:10.1002/app.34805.
87. Huang, C.-L., Peng, S.-Y., Wang, Y.-J., Chen, W.-C., and Lin, J.-H., "Microstructure and characterization of electrospun poly(vinyl alcohol) nanofiber

- scaffolds filled with graphene nanosheets,” *J. Appl. Polym. Sci.* 132(17):n/a-n/a, 2015, doi:10.1002/app.41891.
88. Girard, H.A., Scorsone, E., Saada, S., Gesset, C., Arnault, J.C., Perruchas, S., Rousseau, L., David, S., Pichot, V., Spitzer, D., and Bergonzo, P., “Electrostatic grafting of diamond nanoparticles towards 3D diamond nanostructures,” *Diam. Relat. Mater.* 23:83–87, 2012, doi:10.1016/j.diamond.2012.01.021.
89. Potocký, Š., Ižák, T., Rezek, B., Tesárek, P., and Kromka, A., “Transformation of polymer composite nanofibers to diamond fibers and films by microwave plasma-enhanced CVD process,” *Appl. Surf. Sci.* 312:188–191, 2014, doi:10.1016/j.apsusc.2014.05.119.
90. Varga, M., Potocky, S., Tesarek, P., Babchenko, O., Davydova, M., and Kromka, A., “Diamond growth on copper rods from polymer composite nanofibres,” *Appl. Surf. Sci.* 312:220–225, 2014, doi:10.1016/j.apsusc.2014.05.083.
91. Yanilmaz, M., Kalaoglu, F., Karakas, H., and Sarac, A.S., “Preparation and characterization of electrospun polyurethane-polypyrrole nanofibers and films,” *J. Appl. Polym. Sci.* 125(5):4100–4108, 2012, doi:10.1002/app.36386.
92. Visscher, G.T. and Bianconi, P.A., “Synthesis and characterization of polycarbynes, a new class of carbon-based network polymers,” *J. Am. Chem. Soc.* 116(5):1805–1811, 1994, doi:10.1021/ja00084a023.
93. Visscher, G.T., Nesting, D.C., Badding, J.V., and Bianconi, P.A., “Poly(phenylcarbyne): A Polymer Precursor to Diamond-Like Carbon,” *Science* 260(5113):1496–1499, 1993, doi:10.1126/science.260.5113.1496.
94. Jingsheng, C., Xuejun, W., Zhihao, Z., and Fengyuan, Y., “Nucleation and growth of diamond on silicon substrate coated with polymer,” *Thin Solid Films* 346(1–2):120–124, 1999, doi:10.1016/S0040-6090(98)01494-1.
95. Domonkos, M., Ižák, T., Proška, J., and Kromka, A., “Structuring of diamond films by reactive ion plasma etching,” *Nanomateriály a nanotechnologie ve stavebnictví, České vysoké učení technické v Praze*: 35–40, 2012, doi:978-80-01-05132-0.
96. Kalbacova, M., Broz, A., Babchenko, O., and Kromka, A., “Study on cellular adhesion of human osteoblasts on nano-structured diamond films,” *Phys. Status Solidi B* 246(11–12):2774–2777, 2009, doi:10.1002/pssb.200982253.
97. Babchenko, O., Kromka, A., Hruska, K., Kalbacova, M., Broz, A., and Vanecek, M., “Fabrication of nano-structured diamond films for SAOS-2 cell cultivation,” *Phys. Status Solidi A* 206(9):2033–2037, 2009, doi:10.1002/pssa.200982215.
98. Yang, N., Uetsuka, H., Osawa, E., and Nebel, C.E., “Vertically aligned diamond nanowires for DNA sensing,” *Angew. Chem. Int. Ed.* 47(28):5183–5185, 2008, doi:10.1002/anie.200801706.
99. Joshi, R.K. and Kumar, A., “Diamond and related nanomaterials for MEMS/NEMS applications,” *J. Nanomater.* 2009:1–1, 2009, doi:10.1155/2009/637530.

100. Davydova, M., Kromka, A., Rezek, B., Babchenko, O., Stuchlik, M., and Hruska, K., "Fabrication of diamond nanorods for gas sensing applications," *Appl. Surf. Sci.* 256(18):5602–5605, 2010, doi:10.1016/j.apsusc.2010.03.034.
101. Wang, Q., Qu, S.L., Fu, S.Y., Liu, W.J., Li, J.J., and Gu, C.Z., "Chemical gases sensing properties of diamond nanocone arrays formed by plasma etching," *J. Appl. Phys.* 102(10):103714, 2007, doi:10.1063/1.2817465.
102. Bacakova, L., Broz, A., Liskova, J., Stankova, L., Potocky, S., and Kromka, A., "The application of nanodiamond in biotechnology and tissue engineering," in: Aliofkhazraei, M., ed., *Diamond and Carbon Composites and Nanocomposites*, InTech, ISBN 978-953-51-2453-5, 2016, doi:10.5772/63549.
103. Uetsuka, H., Yamada, T., and Shikata, S., "ICP etching of polycrystalline diamonds: Fabrication of diamond nano-tips for AFM cantilevers," *Diam. Relat. Mater.* 17(4–5):728–731, 2008, doi:10.1016/j.diamond.2007.12.071.
104. Babchenko, O., Kromka, A., Hruska, K., Michalka, M., Potmesil, J., and Vanecek, M., "Nanostructuring of diamond films using self-assembled nanoparticles," *Cent. Eur. J. Phys.* 7(2):310–314, 2009, doi:10.2478/s11534-009-0026-8.
105. Biswas, A., Bayer, I.S., Biris, A.S., Wang, T., Dervishi, E., and Faupel, F., "Advances in top-down and bottom-up surface nanofabrication: techniques, applications & future prospects," *Adv. Colloid Interface Sci.* 170(1–2):2–27, 2012, doi:10.1016/j.cis.2011.11.001.
106. Meng, L., Zhang, J., and Zhu, X.D., "Carbon cone arrays by double-bias assisted hot filament plasma chemical vapor deposition," *Thin Solid Films* 516(10):2981–2986, 2008, doi:10.1016/j.tsf.2007.10.121.
107. Zou, Y.S., Yang, Y., Zhang, W.J., Chong, Y.M., He, B., Bello, I., and Lee, S.T., "Fabrication of diamond nanopillars and their arrays," *Appl. Phys. Lett.* 92(5):053105, 2008, doi:10.1063/1.2841822.
108. Kalbacova, M., Rezek, B., Baresova, V., Wolf-Brandstetter, C., and Kromka, A., "Nanoscale topography of nanocrystalline diamonds promotes differentiation of osteoblasts," *Acta Biomater.* 5(8):3076–3085, 2009, doi:10.1016/j.actbio.2009.04.020.
109. Lee, C.L., Choi, H.W., Gu, E., Dawson, M.D., and Murphy, H., "Fabrication and characterization of diamond micro-optics," *Diam. Relat. Mater.* 15(4–8):725–728, 2006, doi:10.1016/j.diamond.2005.09.033.
110. Potocký, Š., Kromka, A., Babchenko, O., Rezek, B., Martinová, L., and Pokorný, P., "Diamond structures grown from polymer composite nanofibers," *Adv. Sci. Eng. Med.* 5(6):519–521, 2013, doi:10.1166/ asem.2013.1341.
111. Gamo, H., Shimada, K., Nishitani-Gamo, M., and Ando, T., "Ultrafine patterning of nanocrystalline diamond films grown by microwave plasma-assisted chemical vapor deposition," *Jpn. J. Appl. Phys.* 46(9B):6267–6271, 2007, doi:10.7567/JJAP.46.6267.

112. Ando, Y., Nishibayashi, Y., and Sawabe, A., “‘Nano-rods’ of single crystalline diamond,” *Diam. Relat. Mater.* 13(4–8):633–637, 2004, doi:10.1016/j.diamond.2003.10.066.
113. Madou, M.J., “Fundamentals of microfabrication and nanotechnology. Volume II,” CRC Press, Boca Raton, FL, ISBN 978-1-4398-9530-6, 2012.
114. Smirnov, W., Kriele, A., Yang, N., and Nebel, C.E., “Aligned diamond nano-wires: Fabrication and characterisation for advanced applications in bio- and electrochemistry,” *Diam. Relat. Mater.* 19(2–3):186–189, 2010, doi:10.1016/j.diamond.2009.09.001.
115. Janssen, W. and Gheeraert, E., “Dry etching of diamond nanowires using self-organized metal droplet masks,” *Diam. Amp Relat. Mater.* 20(3):389–394, 2011.
116. Babchenko, O., Izak, T., Ukraintsev, E., Hruska, K., Rezek, B., and Kromka, A., “Toward surface-friendly treatment of seeding layer and selected-area diamond growth,” *Phys. Status Solidi B* 247(11–12):3026–3029, 2010, doi:10.1002/pssb.201000124.
117. Fox, N.A., Youh, M.J., Wang, W.N., Steeds, J.W., Cheng, H.-F., and Lin, I.-N., “Properties of electron field emitters prepared by selected area deposition of CVD diamond carbon films,” *Diam. Relat. Mater.* 9(3–6):1263–1269, 2000, doi:10.1016/S0925-9635(99)00262-9.
118. Varga, M., Stehlik, S., Kaman, O., Izak, T., Domonkos, M., Lee, D.S., and Kromka, A., “Templated diamond growth on porous carbon foam decorated with polyvinyl alcohol-nanodiamond composite,” *Carbon* 119:124–132, 2017, doi:10.1016/j.carbon.2017.04.022.
119. Lee, Y.-S. and Sun, J., “Preparation of functionalized nanofibers and their applications,” in: Kumar, A., ed., *Nanofibers*, InTech, ISBN 978-953-7619-86-2, 2010, doi:10.5772/8150.
120. Matsumoto, H. and Tanioka, A., “Functionality in electrospun nanofibrous membranes based on fiber’s size, surface area, and molecular orientation,” *Membranes* 1(3):249–264, 2011, doi:10.3390/membranes1030249.
121. Chee, W.K., Lim, H.N., Zainal, Z., Harrison, I., Huang, N.M., Andou, Y., Chong, K.F., and Pandikumar, A., “Electrospun nanofiber membranes as ultrathin flexible supercapacitors,” *RSC Adv* 7(20):12033–12040, 2017, doi:10.1039/C7RA00406K.
122. Calamak, S., Aksoy, E.A., Ertas, N., Erdogdu, C., Sagiroglu, M., and Ulubayram, K., “Ag/silk fibroin nanofibers: Effect of fibroin morphology on Ag<sup>+</sup> release and antibacterial activity,” *Eur. Polym. J.* 67:99–112, 2015, doi:10.1016/j.eurpolymj.2015.03.068.
123. Ramakrishna, S., Fujihara, K., Teo, W.-E., Yong, T., Ma, Z., and Ramaseshan, R., “Electrospun nanofibers: solving global issues,” *Mater. Today* 9(3):40–50, 2006, doi:10.1016/S1369-7021(06)71389-X.



124. Yalcinkaya, F., Yalcinkaya, B., and Jirsak, O., “Dependent and independent parameters of needleless electrospinning,” in: Haider, S. and Haider, A., eds., *Electrospinning - Material, Techniques, and Biomedical Applications*, InTech, ISBN 978-953-51-2821-2, 2016, doi:10.5772/65838.
125. Sasithorn, N., Martinová, L., Horáková, J., and Mongkholrattanasit, R., “Fabrication of silk fibroin nanofibres by needleless electrospinning,” in: Haider, S. and Haider, A., eds., *Electrospinning - Material, Techniques, and Biomedical Applications*, InTech, ISBN 978-953-51-2821-2, 2016, doi:10.5772/65835.
126. Gao, F. and Nebel, C.E., “Diamond-based supercapacitors: realization and properties,” *ACS Appl. Mater. Interfaces*, 2015, doi:10.1021/acsami.5b07027.
127. Ruffinatto, S., Girard, H.A., Becher, F., Arnault, J.-C., Tromson, D., and Bergonzo, P., “Diamond porous membranes: A material toward analytical chemistry,” *Diam. Relat. Mater.* 55:123–130, 2015, doi:10.1016/j.diamond.2015.03.008.
128. Kondo, T., Kodama, Y., and Yuasa, M., “Fabrication and electrochemical properties of boron-doped diamond hollow fiber wool,” *Trans. Mater. Res. Soc. Jpn.* 37(4):503–506, 2012.
129. Gao, F., Wolfer, M.T., and Nebel, C.E., “Highly porous diamond foam as a thin-film micro-supercapacitor material,” *Carbon* 80:833–840, 2014, doi:10.1016/j.carbon.2014.09.007.
130. Petrák, V., Vlčková Živcová, Z., Krýsová, H., Frank, O., Zukal, A., Klimša, L., Kopeček, J., Taylor, A., Kavan, L., and Mortet, V., “Fabrication of porous boron-doped diamond on SiO<sub>2</sub> fiber templates,” *Carbon* 114:457–464, 2017, doi:10.1016/j.carbon.2016.12.012.
131. Ondič, L., Babchenko, O., Varga, M., Kromka, A., Čtyroký, J., and Pelant, I., “Diamond photonic crystal slab: Leaky modes and modified photoluminescence emission of surface-deposited quantum dots,” *Sci. Rep.* 2(914):1–6, 2012, doi:10.1038/srep00914.
132. Li, L., Schröder, T., Chen, E.H., Bakhru, H., and Englund, D., “One-dimensional photonic crystal cavities in single-crystal diamond,” *Photonics Nanostructures - Fundam. Appl.* 15:130–136, 2015, doi:10.1016/j.photonics.2015.03.002.
133. Izak, T., Babchenko, O., Varga, M., Potocky, S., and Kromka, A., “Low temperature diamond growth by linear antenna plasma CVD over large area,” *Phys. Status Solidi B* 249(12):2600–2603, 2012, doi:10.1002/pssb.201200103.
134. Galář, P., Dzurňák, B., Varga, M., Marton, M., Kromka, A., and Malý, P., “Influence of non-diamond carbon phase on recombination mechanisms of photoexcited charge carriers in microcrystalline and nanocrystalline diamond studied by time resolved photoluminescence spectroscopy,” *Opt. Mater. Express* 4(4):624–637, 2014, doi:10.1364/OME.4.000624.
135. Kozák, M., Trojánek, F., Galář, P., Varga, M., Kromka, A., and Malý, P., “Coherent phonon dynamics in micro- and nanocrystalline diamond,” *Opt. Express* 21(25):31521–31529, 2013, doi:10.1364/OE.21.031521.

136. Rath, P., Khasminskaya, S., Nebel, C., Wild, C., and Pernice, W.H.P., “Diamond-integrated optomechanical circuits,” *Nat. Commun.* 4:1690, 2013, doi:10.1038/ncomms2710.
137. Malmström, M., Karlsson, M., Forsberg, P., Cai, Y., Nikolajeff, F., and Laurell, F., “Waveguides in polycrystalline diamond for mid-IR sensing,” *Opt. Mater. Express* 6(4):1286–1295, 2016, doi:10.1364/OME.6.001286.
138. Prajzler, V., Varga, M., Nekvindova, P., Remes, Z., and Kromka, A., “Design and investigation of properties of nanocrystalline diamond optical planar waveguides,” *Opt. Express* 21(7):8417–8425, 2013, doi:10.1364/OE.21.008417.
139. Baldwin, J.W., Zalalutdinov, M., Feygelson, T., Butler, J.E., and Houston, B.H., “Fabrication of short-wavelength photonic crystals in wide-band-gap nanocrystalline diamond films,” *J. Vac. Sci. Technol. B Microelectron. Nanometer Struct.* 24(1):50–54, 2006, doi:10.1116/1.2138722.
140. Krauss, T.F. and De La Rue, R.M., “Photonic crystals in the optical regime — past, present and future,” *Prog. Quantum Electron.* 23(2):51–96, 1999, doi:10.1016/S0079-6727(99)00004-X.
141. Pathak, S., Vanslebrouck, M., Dumon, P., Thourhout, D.V., and Bogaerts, W., “Compact SOI-based polarization diversity wavelength de-multiplexer circuit using two symmetric AWGs,” *Opt. Express* 20(26):B493–B500, 2012, doi:10.1364/OE.20.00B493.
142. Domonkos, M., Izak, T., Stolcova, L., Proška, J., and Kromka, A., “Controlled structuring of self-assembled polystyrene microsphere arrays by two different plasma systems,” *5th International Conference Proceedings, TANGER, Brno*, ISBN 978-80-87294-47-5: 34–38, 2013.
143. Domonkos, M., Ižák, T., Štolcová, L., Proška, J., and Kromka, A., “Reactive ion etching of polystyrene microspheres,” *Nanomateriály a nanotechnologie ve stavebnictví, České vysoké učení technické v Praze*, ISBN 978-80-01-05334-8: 24–28, 2013.
144. Yu, Y. and Zhang, G., “Colloidal lithography,” in: Hosaka, S., ed., *Updates in Advanced Lithography*, InTech, ISBN 978-953-51-1175-7, 2013, doi:10.5772/56576.
145. Deckman, H.W. and Dunsmuir, J.H., “Applications of surface textures produced with natural lithography,” *J. Vac. Sci. Technol. B* 1(4):1109–1112, 1983, doi:10.1116/1.582644.
146. Yang, S.-M., Jang, S.G., Choi, D.-G., Kim, S., and Yu, H.K., “Nanomachining by colloidal lithography,” *Small Weinh. Bergstr. Ger.* 2(4):458–475, 2006, doi:10.1002/sml.200500390.
147. Kosiorek, A., Kandulski, W., Chudzinski, P., Kempa, K., and Giersig, M., “Shadow Nanosphere Lithography: Simulation and Experiment,” *Nano Lett.* 4(7):1359–1363, 2004, doi:10.1021/nl049361t.

148. Acikgoz, C., “Controlled polymer nanostructures by alternative lithography,” University of Twente, Enschede, ISBN 978-90-365-2976-1, 2010.
149. Colson, P., Henrist, C., and Cloots, R., “Nanosphere lithography: a powerful method for the controlled manufacturing of nanomaterials,” *J. Nanomater.* 2013:1–19, 2013, doi:10.1155/2013/948510.
150. Domonkos, M., Izak, T., and Kromka, A., “Fabrication of self-assembled microsphere monolayers,” *Material analysis in vacuum*, Slovenská vákuová spoločnosť, Bratislava, Štrbské Pleso, ISBN 978-80-971179-4-8: 125–128, 2014.
151. Lebedev-Stepanov, P.V., Kadushnikov, R.M., Molchanov, S.P., Ivanov, A.A., Mitrokhin, V.P., Vlasov, K.O., Rubin, N.I., Yurasik, G.A., Nazarov, V.G., and Alfimov, M.V., “Self-assembly of nanoparticles in the microvolume of colloidal solution: Physics, modeling, and experiment,” *Nanotechnologies Russ.* 8(3–4):137–162, 2013, doi:10.1134/S1995078013020110.
152. Bensaude-Vincent, B., “Self-assembly, self-organization: nanotechnology and vitalism,” *NanoEthics* 3(1):31–42, 2009, doi:10.1007/s11569-009-0056-0.
153. Dommelen, R. van, Fanzio, P., and Sasso, L., “Surface self-assembly of colloidal crystals for micro- and nano-patterning,” *Adv. Colloid Interface Sci.*, 2017, doi:10.1016/j.cis.2017.10.007.
154. Ozin, G.A., Hou, K., Lotsch, B.V., Cademartiri, L., Puzzo, D.P., Scotognella, F., Ghadimi, A., and Thomson, J., “Nanofabrication by self-assembly,” *Mater. Today* 12(5):12–23, 2009, doi:10.1016/S1369-7021(09)70156-7.
155. McGorty, R., Fung, J., Kaz, D., and Manoharan, V.N., “Colloidal self-assembly at an interface,” *Mater. Today* 13(6):34–42, 2010, doi:10.1016/S1369-7021(10)70107-3.
156. Cheon, S.-E., Lee, H., Choi, J., Jeong, A.R., Lee, T.S., Jeong, D.S., Lee, K.-S., Lee, W.-S., Kim, W.M., Lee, H., and Kim, I., “Fabrication of parabolic Si nanostructures by nanosphere lithography and its application for solar cells,” *Sci. Rep.* 7(1), 2017, doi:10.1038/s41598-017-07463-7.
157. Stein, A., “Sphere templating methods for periodic porous solids,” *Microporous Mesoporous Mater.* 44–45:227–239, 2001, doi:10.1016/S1387-1811(01)00189-5.
158. Yu, J., Geng, C., Zheng, L., Ma, Z., Tan, T., Wang, X., Yan, Q., and Shen, D., “Preparation of high-quality colloidal mask for nanosphere lithography by a combination of air/water interface self-assembly and solvent vapor annealing,” *Langmuir* 28(34):12681–12689, 2012, doi:10.1021/la3026182.
159. Xia, Y., Gates, B., Yin, Y., and Lu, Y., “Monodispersed colloidal spheres: old materials with new applications,” *Adv. Mater.* 12(10):693–713, 2000, doi:10.1002/(SICI)1521-4095(200005)12:10<693::AID-ADMA693>3.0.CO;2-J.
160. Jódar-Reyes, A.B., Martín-Rodríguez, A., and Ortega-Vinuesa, J.L., “Effect of the ionic surfactant concentration on the stabilization/destabilization of polystyrene

- colloidal particles,” *J. Colloid Interface Sci.* 298(1):248–257, 2006, doi:10.1016/j.jcis.2005.12.035.
161. Lotito, V. and Zambelli, T., “Approaches to self-assembly of colloidal monolayers: A guide for nanotechnologists,” *Adv. Colloid Interface Sci.* 246:217–274, 2017, doi:10.1016/j.cis.2017.04.003.
162. Brown, E.C., Wilke, S.K., Boyd, D.A., Goodwin, D.G., and Haile, S.M., “Polymer sphere lithography for solid oxide fuel cells: a route to functional, well-defined electrode structures,” *J. Mater. Chem.* 20(11):2190, 2010, doi:10.1039/b920973e.
163. Zhang, J., Li, Y., Zhang, X., and Yang, B., “Colloidal self-assembly meets nanofabrication: from two-dimensional colloidal crystals to nanostructure arrays,” *Adv. Mater.* 22(38):4249–4269, 2010, doi:10.1002/adma.201000755.
164. Guo, W., Wang, M., Xia, W., and Dai, L., “Two substrate-confined sol–gel coassembled ordered macroporous silica structures with an open surface,” *Langmuir* 29(20):5944–5951, 2013, doi:10.1021/la304268b.
165. Burkhardt, C., Fuchsberger, K., Nisch, W., and Stelzle, M., “Micro- and nanopatterning of surfaces employing self assembly of nanoparticles and its application in biotechnology and biomedical engineering,” in: Wang, M., ed., *Lithography*, InTech, ISBN 978-953-307-064-3, 2010.
166. Pillai, S., Hemmersam, A.G., Mukhopadhyay, R., Meyer, R.L., Moghimi, S.M., Besenbacher, F., and Kingshott, P., “Tunable 3D and 2D polystyrene nanoparticle assemblies using surface wettability, low volume fraction and surfactant effects,” *Nanotechnology* 20(2):025604, 2009, doi:10.1088/0957-4484/20/2/025604.
167. Barcelo, S.J., Lam, S.-T., Gibson, G.A., Sheng, X., and Henze, D., “Nanosphere lithography based technique for fabrication of large area, well ordered metal particle arrays,” *SPIE Advanced Lithography*, International Society for Optics and Photonics: 83232L–83232L, 2012.
168. Kalantar-zadeh, K. and Fry, B., “Nanotechnology-Enabled Sensors,” Springer US, Boston, MA, ISBN 978-0-387-32473-9, 2008.
169. Rossi, R.C., Tan, M.X., and Lewis, N.S., “Size-dependent electrical behavior of spatially inhomogeneous barrier height regions on silicon,” *Appl. Phys. Lett.* 77(17):2698–2700, 2000, doi:10.1063/1.1319534.
170. Dimitrov, A.S. and Nagayama, K., “Continuous convective assembling of fine particles into two-dimensional arrays on solid surfaces,” *Langmuir* 12(5):1303–1311, 1996, doi:10.1021/la9502251.
171. Ye, X. and Qi, L., “Recent advances in fabrication of monolayer colloidal crystals and their inverse replicas,” *Sci. China Chem.* 57(1):58–69, 2014, doi:10.1007/s11426-013-5018-2.
172. Marczewski, D. and Goedel, W.A., “The preparation of submicrometer-sized rings by embedding and selective etching of spherical silica particles,” *Nano Lett.* 5(2):295–299, 2005, doi:10.1021/nl0481021.

173. X. Wang, Summers, C.J., and Wang, Z.L., “Large-scale hexagonal-patterned growth of aligned ZnO nanorods for nano-optoelectronics and nanosensor arrays,” *Nano Lett.* 4(3):423–426, 2004, doi:10.1021/nl035102c.
174. Fulda, K.-U. and Tieke, B., “Langmuir films of monodisperse 0.5  $\mu\text{m}$  spherical polymer particles with a hydrophobic core and a hydrophilic shell,” *Adv. Mater.* 6(4):288–290, 1994, doi:10.1002/adma.19940060405.
175. Domonkos, M., “Preparation of periodically arranged arrays of nanostructures by the reactive ion etching method,” Master’s thesis, Czech Technical University in Prague, Faculty of Nuclear Sciences and Physical Engineering, 2014.
176. Kumar, C.S.S.R., “Nanostructured thin films and surfaces,” 1 edition, Wiley-VCH, Weinheim, ISBN 978-3-527-32155-1, 2010.
177. Cheung, C.L., Nikolić, R.J., Reinhardt, C.E., and Wang, T.F., “Fabrication of nanopillars by nanosphere lithography,” *Nanotechnology* 17(5):1339–1343, 2006, doi:10.1088/0957-4484/17/5/028.
178. Domonkos, M., Izak, T., Demo, P., and Kromka, A., “Applications of self-assembled 2D polystyrene nanosphere arrays,” *Nanomateriály a nanotechnologie ve stavebnictví*, České vysoké učení technické v Praze, ISBN 978-80-01-05512-0: 42–47, 2014.
179. Le Ru, E.C., “Principles of surface-enhanced Raman spectroscopy: and related plasmonic effects,” 1st ed, Elsevier, Amsterdam; Boston, ISBN 978-0-444-52779-0, 2009.
180. Ngo, H.T., Wang, H.-N., Fales, A.M., and Vo-Dinh, T., “Label-free DNA biosensor based on SERS molecular sentinel on nanowave chip,” *Anal. Chem.* 85(13):6378–6383, 2013, doi:10.1021/ac400763c.
181. Tan, B.J.Y., Sow, C.H., Koh, T.S., Chin, K.C., Wee, A.T.S., and Ong, C.K., “Fabrication of size-tunable gold nanoparticles array with nanosphere lithography, reactive ion etching, and thermal annealing,” *J. Phys. Chem. B* 109(22):11100–11109, 2005, doi:10.1021/jp045172n.
182. Zhang, J. and Yang, B., “Patterning colloidal crystals and nanostructure arrays by soft lithography,” *Adv. Funct. Mater.* 20(20):3411–3424, 2010, doi:10.1002/adfm.201000795.
183. Hall, A.S., Friesen, S.A., and Mallouk, T.E., “Wafer-scale fabrication of plasmonic crystals from patterned silicon templates prepared by nanosphere lithography,” *Nano Lett.* 13(6):2623–2627, 2013, doi:10.1021/nl400755a.
184. Ellinas, K., Smyrnakis, A., Malainou, A., Tserepi, A., and Gogolides, E., “‘Mesh-assisted’ colloidal lithography and plasma etching: A route to large-area, uniform, ordered nano-pillar and nanopost fabrication on versatile substrates,” *Microelectron. Eng.* 88(8):2547–2551, 2011, doi:10.1016/j.mee.2010.12.073.
185. Valsesia, A., Meziani, T., Bretagnol, F., Colpo, P., Ceccone, G., and Rossi, F., “Plasma assisted production of chemical nano-patterns by nano-sphere lithography:

- application to bio-interfaces,” *J. Phys. Appl. Phys.* 40(8):2341–2347, 2007, doi:10.1088/0022-3727/40/8/S13.
186. Wang, C., Yap, F.L., and Zhang, Y., “Micropatterning of polystyrene nanoparticles and its bioapplications,” *Colloids Surf. B Biointerfaces* 46(4):255–260, 2005, doi:10.1016/j.colsurfb.2005.11.006.
187. Wang, M., Fu, L., Gan, L., Zhang, C., Rummeli, M., Bachmatiuk, A., Huang, K., Fang, Y., and Liu, Z., “CVD growth of large area smooth-edged graphene nanomesh by nanosphere lithography,” *Sci. Rep.* 3, 2013, doi:10.1038/srep01238.
188. Kanti Paul, R., Badhulika, S., Saucedo, N.M., and Mulchandani, A., “Graphene nanomesh as highly sensitive chemiresistor gas sensor,” *Anal. Chem.* 84(19):8171–8178, 2012.
189. Fünér, M., Wild, C., and Koidl, P., “Novel microwave plasma reactor for diamond synthesis,” *Appl. Phys. Lett.* 72(10):1149–1151, 1998, doi:10.1063/1.120997.
190. Kromka, A., Potocký, Š., Čermák, J., Rezek, B., Potměšil, J., Zemek, J., and Vaněček, M., “Early stage of diamond growth at low temperature,” *Diam. Relat. Mater.* 17(7–10):1252–1255, 2008, doi:10.1016/j.diamond.2008.03.035.
191. Kromka, A., Babchenko, O., Potocky, S., Rezek, B., Sveshnikov, A., Demo, P., Izak, T., and Varga, M., “Chapter 9 - Diamond nucleation and seeding techniques for tissue regeneration,” in: Narayan, R., ed., *Diamond-Based Materials for Biomedical Applications*, Woodhead Publishing, ISBN 978-0-85709-340-0: 206–255, 2013.
192. Potocký, Š., Babchenko, O., Hruška, K., and Kromka, A., “Linear antenna microwave plasma CVD diamond deposition at the edge of no-growth region of C-H-O ternary diagram,” *Phys. Status Solidi B* 249(12):2612–2615, 2012, doi:10.1002/pssb.201200124.
193. Tsugawa, K., Kawaki, S., Ishihara, M., Kim, J., Koga, Y., Sakakita, H., Koguchi, H., and Hasegawa, M., “Nanocrystalline diamond growth in a surface-wave plasma,” *Diam. Relat. Mater.* 20(5–6):833–838, 2011.
194. Jansen, H., Gardeniers, H., Boer, M. de, Elwenspoek, M., and Fluitman, J., “A survey on the reactive ion etching of silicon in microtechnology,” *J. Micromechanics Microengineering* 6(1):14, 1996.
195. Karouta, F., “A practical approach to reactive ion etching,” *J. Phys. Appl. Phys.* 47(23):233501, 2014, doi:10.1088/0022-3727/47/23/233501.
196. Nojiri, K., “Mechanism of dry etching,” *Dry Etching Technology for Semiconductors*, Springer International Publishing, Cham, ISBN 978-3-319-10294-8: 11–30, 2015, doi:10.1007/978-3-319-10295-5\_2.
197. Patrick Verdonck, *Dry Etching for Integrated Circuit Fabrication*, 1990.
198. Spin coating: a guide to theory and techniques, <https://www.ossila.com/pages/spin-coating>, Dec. 2017.

- 
199. [http://images.laurell.com/images/spin-coaters/wet-station-WS-650-23\\_m.jpg](http://images.laurell.com/images/spin-coaters/wet-station-WS-650-23_m.jpg).
200. Tyona, M.D., “A theoretical study on spin coating technique,” *Adv. Mater. Res.* 2(4):195–208, 2013, doi:10.12989/amr.2013.2.4.195.
201. Zheng, H. and Ravaine, S., “Bottom-up assembly and applications of photonic materials,” *Crystals* 6(5):54, 2016, doi:10.3390/cryst6050054.
202. Acikgoz, C., Hempenius, M.A., Huskens, J., and Vancso, G.J., “Polymers in conventional and alternative lithography for the fabrication of nanostructures,” *Eur. Polym. J.* 47(11):2033–2052, 2011, doi:10.1016/j.eurpolymj.2011.07.025.
203. Lubambo, A.F., Lucyszyn, N., Petzhold, C.L., Camargo, P.C. de, Sierakowski, M.-R., Schreiner, W.H., and Saul, C.K., “Self-assembled polystyrene/xyloglucan nanospheres from spin coating evaporating mixtures,” *Carbohydr. Polym.* 84(1):126–132, 2011, doi:10.1016/j.carbpol.2010.11.010.
204. Toolan, D.T.W., Fujii, S., Ebbens, S.J., Nakamura, Y., and Howse, J.R., “On the mechanisms of colloidal self-assembly during spin-coating,” *Soft Matter*, 2014, doi:10.1039/C4SM01711K.
205. Arutinov, G., Brichkin, S.B., and Razumov, V.F., “Self-assembling of polystyrene microsphere monolayers by spin-coating,” *Nanotechnologies Russ.* 5(1–2):67–72, 2010, doi:10.1134/S1995078010010064.
206. Nandiyanto, A.B.D., Ogi, T., Iskandar, F., and Okuyama, K., “Highly ordered porous monolayer generation by dual-speed spin-coating with colloidal templates,” *Chem. Eng. J.* 167(1):409–415, 2011, doi:10.1016/j.cej.2010.11.077.
207. Shinde, S.S. and Park, S., “Oriented colloidal-crystal thin films of polystyrene spheres via spin coating,” *J. Semicond.* 36:023001, 2015, doi:10.1088/1674-4926/36/2/023001.
208. Chandramohan, A., Sibirev, N.V., Dubrovskii, V.G., Petty, M.C., Gallant, A.J., and Zeze, D.A., “Model for large-area monolayer coverage of polystyrene nanospheres by spin coating,” *Sci. Rep.* 7:40888, 2017, doi:10.1038/srep40888.
209. Kralchevsky, P.A. and Denkov, N.D., “Capillary forces and structuring in layers of colloid particles,” *Curr. Opin. Colloid Interface Sci.* 6(4):383–401, 2001.
210. Armstrong, E. and O’Dwyer, C., “Artificial opal photonic crystals and inverse opal structures – fundamentals and applications from optics to energy storage,” *J. Mater. Chem. C* 3(24):6109–6143, 2015, doi:10.1039/C5TC01083G.
211. Ko, Y.G., Shin, D.H., Lee, G.S., and Choi, U.S., “Fabrication of colloidal crystals on hydrophilic/hydrophobic surface by spin-coating,” *Colloids Surf. Physicochem. Eng. Asp.* 385(1–3):188–194, 2011, doi:10.1016/j.colsurfa.2011.06.011.
212. Li, W., Wang, S., He, S., Hu, M., Ge, P., Wang, J., and Guo, Y., “Controlled fabrication of Si nanowires with nanodots using nanosphere lithography,” *J. Nanosci. Nanotechnol.* 16(2):1537–1540, 2016, doi:10.1166/jnn.2016.10857.



213. Wu, Y., Xu, X., Zhang, H., Liu, L., Li, J., and Yang, D., “Improving self-assembly quality of colloidal crystal guided by statistical design of experiments,” *Chin. Phys. B* 26(3):038105, 2017, doi:10.1088/1674-1056/26/3/038105.
214. Lu, Z. and Zhou, M., “Fabrication of large scale two-dimensional colloidal crystal of polystyrene particles by an interfacial self-ordering process,” *J. Colloid Interface Sci.* 361(2):429–435, 2011, doi:10.1016/j.jcis.2011.06.011.
215. Kannadorai, R.K., Dinish, U.S., Fu, C.Y., Olivo, M., and Asundi, A., “Fabrication and characterization of mono-layered polystyrene beads using nanosphere lithography (NSL) for metal-enhanced fluorescence (MEF),” 752269-752269–6, 2009, doi:10.1117/12.851636.
216. Zhang, C., Cvetanovic, S., and Pearce, J.M., “Fabricating ordered 2-D nanostructured arrays using nanosphere lithography,” *MethodsX*, 2017, doi:10.1016/j.mex.2017.07.001.
217. Innocenzi, P., Malfatti, L., and Falcaro, P., “Water droplets to nanotechnology: a journey through self-assembly,” RSC Publ., Royal Soc. of Chemistry, Cambridge, ISBN 978-1-84973-664-0, 2013.
218. Marcel Sperling and Michael Gradzielski, “Droplets, evaporation and a superhydrophobic surface: simple tools for guiding colloidal particles into complex materials,” *Gels* 3(2):15, 2017, doi:10.3390/gels3020015.
219. Cabrera, E.-J., Jaller, L.M., Amade, R., Portal, S.M., Pascual, E., and Bertran, E., “Photonic characteristics of Langmuir-Blodgett self-assembled monolayers of colloidal silica particles,” *Nanosci. Nanotechnol. Lett.* 5(1):41–45, 2013.
220. Hall, A.S., Friesen, S.A., and Mallouk, T.E., “Wafer-scale fabrication of plasmonic crystals from patterned silicon templates prepared by nanosphere lithography,” *Nano Lett.* 13(6):2623–2627, 2013, doi:10.1021/nl400755a.
221. Bauer, C.T., Wonn, A., Brodoceanu, D., Born, P., Kroner, E., and Kraus, T., “Size and shape evolution of PS particle layers during etching,” *Bioinspired Biomim. Nanobiomaterials* 2(3):130–140, 2013, doi:10.1680/bbn.13.00002.
222. Ji, D., Li, T., and Fuchs, H., “Nanosphere lithography for sub-10-nm nanogap electrodes,” *Adv. Electron. Mater.* 3(1):1600348, 2017, doi:10.1002/aelm.201600348.
223. Ni, H., Wang, M., Hao, H., and Zhou, J., “Integration of tunable two-dimensional nanostructures on a chip by an improved nanosphere lithography method,” *Nanotechnology* 27(22):225301, 2016, doi:10.1088/0957-4484/27/22/225301.
224. Ye, X., Huang, J., Geng, F., Liu, H., Sun, L., Yan, L., Jiang, X., Wu, W., and Zheng, W., “High power laser antireflection subwavelength grating on fused silica by colloidal lithography,” *J. Phys. Appl. Phys.* 49(26):265104, 2016, doi:10.1088/0022-3727/49/26/265104.

225. Akinoglu, E.M., Morfa, A.J., and Giersig, M., “Understanding anisotropic plasma etching of two-dimensional polystyrene opals for advanced materials fabrication,” *Langmuir* 140314113526001, 2014, doi:10.1021/la500003u.
226. Cao, H., Li, X., Zhou, B., Chen, T., Shi, T., Zheng, J., Liu, G., and Wang, Y., “On-demand fabrication of Si/SiO<sub>2</sub> nanowire arrays by nanosphere lithography and subsequent thermal oxidation,” *Nanoscale Res. Lett.* 12(1), 2017, doi:10.1186/s11671-017-1883-5.
227. Plettl, A., Enderle, F., Saitner, M., Manzke, A., Pfahler, C., Wiedemann, S., and Ziemann, P., “Non-close-packed crystals from self-assembled polystyrene spheres by isotropic plasma etching: adding flexibility to colloid lithography,” *Adv. Funct. Mater.* 19(20):3279–3284, 2009, doi:10.1002/adfm.200900907.
228. Cong, C., Junus, W.C., Shen, Z., and Yu, T., “New colloidal lithographic nanopatterns fabricated by combining pre-heating and reactive ion etching,” *Nanoscale Res. Lett.* 4(11):1324–1328, 2009, doi:10.1007/s11671-009-9400-0.
229. Potocký, Š., Čada, M., Babchenko, O., Ižák, T., Davydova, M., and Kromka, A., “Perspectives of linear antenna microwave system for growth of various carbon nano-forms and its plasma study,” *Phys. Status Solidi B* 250(12):2723–2726, 2013, doi:10.1002/pssb.201300085.
230. Geng, C., Zheng, L., Yu, J., Yan, Q., Wei, T., Wang, X., and Shen, D., “Thermal annealing of colloidal monolayer at the air/water interface: a facile approach to transferrable colloidal masks with tunable interstice size for nanosphere lithography,” *J. Mater. Chem.* 22(42):22678, 2012, doi:10.1039/c2jm33660j.
231. Lewicka, Z.A., Li, Y., Bohloul, A., Yu, W.W., and Colvin, V.L., “Nanorings and nanocrescents formed via shaped nanosphere lithography: a route toward large areas of infrared metamaterials,” *Nanotechnology* 24(11):115303, 2013, doi:10.1088/0957-4484/24/11/115303.
232. Pisco, M., Galeotti, F., Quero, G., Grisci, G., Micco, A., Mercaldo, L.V., Veneri, P.D., Cutolo, A., and Cusano, A., “Nanosphere lithography for optical fiber tip nanoprobe,” *Light Sci. Appl.* 6(5):e16229, 2017, doi:10.1038/lsa.2016.229.
233. Gong, J., Li, G., and Tang, Z., “Self-assembly of noble metal nanocrystals: Fabrication, optical property, and application,” *Nano Today* 7(6):564–585, 2012, doi:10.1016/j.nantod.2012.10.008.
234. Aiempanakit, M., Jearnkulprasert, N., and Panyajirawut, P., “Patterning of Nanoparticle Arrays by Self-assembly Lithography,” *Mater. Today Proc.* 4(5):6009–6014, 2017, doi:10.1016/j.matpr.2017.06.087.
235. Stolcová, L., Domonkos, M., Izák, T., Proška, J., Procházka, M., and Kromka, A., “Plasma treatment as a versatile technique for preparation of plasmonic nanoantenna arrays,” *Progress in Electromagnetics Research Symposium (PIERS) Proceedings*, Stockholm, Sweden: 426–430, 2013.

236. Choi, D.-G., Yu, H.K., Jang, S.G., and Yang, S.-M., “Colloidal lithographic nanopatterning via reactive ion etching,” *J. Am. Chem. Soc.* 126(22):7019–7025, 2004, doi:10.1021/ja0319083.
237. Zhao, J., Frank, B., Neubrech, F., Zhang, C., Braun, P.V., and Giessen, H., “Hole-mask colloidal nanolithography combined with tilted-angle-rotation evaporation: A versatile method for fabrication of low-cost and large-area complex plasmonic nanostructures and metamaterials,” *Beilstein J. Nanotechnol.* 5:577–586, 2014, doi:10.3762/bjnano.5.68.
238. Ingram, W., He, Y., Stone, K., Dennis, W.M., Ye, D., and Zhao, Y., “Tuning the plasmonic properties of silver nanopatterns fabricated by shadow nanosphere lithography,” *Nanotechnology* 27(38):385301, 2016, doi:10.1088/0957-4484/27/38/385301.
239. Tzeng, Y.-K., Jingyuan Linda Zhang, Lu, H., Ishiwata, H., Dahl, J., Carlson, R.M.K., Yan, H., Schreiner, P.R., Vučković, J., Shen, Z.-X., Melosh, N., and Chu, S., “Vertical-substrate MPCVD epitaxial nanodiamond growth,” *Nano Lett.* 17(3):1489–1495, 2017, doi:10.1021/acs.nanolett.6b04543.
240. Williams, O.A., Douhéret, O., Daenen, M., Haenen, K., Ōsawa, E., and Takahashi, M., “Enhanced diamond nucleation on monodispersed nanocrystalline diamond,” *Chem. Phys. Lett.* 445(4–6):255–258, 2007, doi:10.1016/j.cplett.2007.07.091.
241. Nave, A.S.C., Baudrillart, B., Hamann, S., Bénédic, F., Lombardi, G., Gicquel, A., Helden, J.H. van, and Röpcke, J., “Spectroscopic study of low pressure, low temperature H<sub>2</sub>–CH<sub>4</sub>–CO<sub>2</sub> microwave plasmas used for large area deposition of nanocrystalline diamond films. Part I: on temperature determination and energetic aspects,” *Plasma Sources Sci. Technol.* 25(6):065002, 2016, doi:10.1088/0963-0252/25/6/065002.
242. Nave, A.S.C., Baudrillart, B., Hamann, S., Bénédic, F., Lombardi, G., Gicquel, A., Helden, J.H. van, and Röpcke, J., “Spectroscopic study of low pressure, low temperature H<sub>2</sub>–CH<sub>4</sub>–CO<sub>2</sub> microwave plasmas used for large area deposition of nanocrystalline diamond films. Part II: on plasma chemical processes,” *Plasma Sources Sci. Technol.* 25(6):065003, 2016, doi:10.1088/0963-0252/25/6/065003.
243. Baudrillart, B., Bénédic, F., Brinza, O., Bieber, T., Chauveau, T., Achard, J., and Gicquel, A., “Microstructure and growth kinetics of nanocrystalline diamond films deposited in large area/low temperature distributed antenna array microwave-plasma reactor,” *Phys. Status Solidi A* 212(11):2611–2615, 2015, doi:10.1002/pssa.201532276.
244. H. Kuzmany, R.P., “The mystery of the 1140 cm<sup>-1</sup> Raman line in nanocrystalline diamond films,” *Carbon* 42(5):911–917, 2004, doi:10.1016/j.carbon.2003.12.045.
245. Arora, A.K., Rajalakshmi, M., Ravindran, T.R., and Sivasubramanian, V., “Raman spectroscopy of optical phonon confinement in nanostructured materials,” *J. Raman Spectrosc.* 38(6):604–617, 2007, doi:10.1002/jrs.1684.

- 
246. Yoshikawa, M., Mori, Y., Maegawa, M., Katagiri, G., Ishida, H., and Ishitani, A., "Raman scattering from diamond particles," *Appl. Phys. Lett.* 62(24):3114–3116, 1993, doi:10.1063/1.109154.
247. Jirásek, V., Ižák, T., Varga, M., Babchenko, O., and Kromka, A., "Investigation of residual stress in structured diamond films grown on silicon," *Thin Solid Films* 589:857–863, 2015, doi:10.1016/j.tsf.2015.07.022.
248. Izak, T., Sveshnikov, A., Demo, P., and Kromka, A., "Enhanced spontaneous nucleation of diamond nuclei in hot and cold microwave plasma systems: Spontaneous nucleation of diamond nuclei microwave plasma systems," *Phys. Status Solidi B* 250(12):2753–2758, 2013, doi:10.1002/pssb.201300117.
249. Kromka, A., Babchenko, O., Izak, T., Hruska, K., and Rezek, B., "Linear antenna microwave plasma CVD deposition of diamond films over large areas," *Vacuum* 86(6):776–779, 2012, doi:10.1016/j.vacuum.2011.07.008.
250. Tsugawa, K., Ishihara, M., Kim, J., Koga, Y., and Hasegawa, M., "Nanocrystalline diamond film growth on plastic substrates at temperatures below 100 ° C from low-temperature plasma," *Phys. Rev. B* 82(12), 2010, doi:10.1103/PhysRevB.82.125460.
251. Mehedi, H.-A., Achard, J., Rats, D., Brinza, O., Tallaire, A., Mille, V., Silva, F., Provent, C., and Gicquel, A., "Low temperature and large area deposition of nanocrystalline diamond films with distributed antenna array microwave-plasma reactor," *Diam. Relat. Mater.* 47:58–65, 2014, doi:10.1016/j.diamond.2014.05.004.
252. Babchenko, O., Potocký, Š., Ižák, T., Hruška, K., Bryknar, Z., and Kromka, A., "Influence of surface wave plasma deposition conditions on diamond growth regime," *Surf. Coat. Technol.* 271:74–79, 2015, doi:10.1016/j.surfcoat.2015.01.012.
253. Elliott, M.A., May, P.W., Petherbridge, J., Leeds, S.M., Ashfold, M.N.R., and Wang, W.N., "Optical emission spectroscopic studies of microwave enhanced diamond CVD using CH<sub>4</sub>/CO<sub>2</sub> plasmas," *Diam. Relat. Mater.* 9(3):311–316, 2000.
254. Butler, J.E., Mankelevich, Y.A., Cheesman, A., Ma, J., and Ashfold, M.N.R., "Understanding the chemical vapor deposition of diamond: recent progress," *J. Phys. Condens. Matter* 21(36):364201, 2009, doi:10.1088/0953-8984/21/36/364201.
255. Nelson, N., Rakowski, R.T., Franks, J., Woolliams, P., Weaver, P., and Jones, B.J., "The effect of substrate geometry and surface orientation on the film structure of DLC deposited using PECVD," *Surf. Coat. Technol.* 254:73–78, 2014, doi:10.1016/j.surfcoat.2014.05.066.
256. Aguilar, J., Valdez, Z., and Ortiz, U., "The reliability of thermocouples in microwave ceramics processing," *J. Microw. Power Electromagn. Energy Publ. Int. Microw. Power Inst.* 39(3–4):191–196, 2004.
257. Pert, E., Carmel, Y., Birnboim, A., Olorunyolemi, T., Gershon, D., Calame, J., Lloyd, I.K., and Wilson, O.C., "Temperature measurements during microwave

- processing: the significance of thermocouple effects,” *J. Am. Ceram. Soc.* 84(9):1981–1986, 2004, doi:10.1111/j.1151-2916.2001.tb00946.x.
258. Yun, J. and Dandy, D.S., “A kinetic model of diamond nucleation and silicon carbide interlayer formation during chemical vapor deposition,” *Diam. Relat. Mater.* 14(8):1377–1388, 2005, doi:10.1016/j.diamond.2005.02.008.
259. Kim, D.-G., Lee, H.-C., and Lee, J.-Y., “Effect of reaction pressure on the nucleation behaviour of diamond synthesized by hot-filament chemical vapour deposition,” *J. Mater. Sci.* 28(24):6704–6708, 1993, doi:10.1007/BF00356418.
260. Park, J.-W., Kim, K.-S., and Hwang, N.-M., “Gas phase generation of diamond nanoparticles in the hot filament chemical vapor deposition reactor,” *Carbon* 106:289–294, 2016, doi:10.1016/j.carbon.2016.05.035.
261. Kumar, A., Ann Lin, P., Xue, A., Hao, B., Khin Yap, Y., and Sankaran, R.M., “Formation of nanodiamonds at near-ambient conditions via microplasma dissociation of ethanol vapour,” *Nat. Commun.* 4:2618, 2013, doi:10.1038/ncomms3618.
262. Frenklach, M., Kematick, R., Huang, D., Howard, W., Spear, K.E., Phelps, A.W., and Koba, R., “Homogeneous nucleation of diamond powder in the gas phase,” *J. Appl. Phys.* 66(1):395, 1989, doi:10.1063/1.343890.
263. Narayan, J. and Bhaumik, A., “Novel phase of carbon, ferromagnetism, and conversion into diamond,” *J. Appl. Phys.* 118(21):215303, 2015, doi:10.1063/1.4936595.
264. Hwang, N.M., “Non-classical crystallization of thin films and nanostructures in CVD and PVD processes,” Springer, Dordrecht, ISBN 978-94-017-7616-5, 2016.
265. Badziag, P., Verwoerd, W.S., Ellis, W.P., and Greiner, N.R., “Nanometre-sized diamonds are more stable than graphite,” *Nature* 343(6255):244–245, 1990, doi:10.1038/343244a0.
266. Hwang, N.-M. and Lee, D.-K., “Charged nanoparticles in thin film and nanostructure growth by chemical vapour deposition,” *J. Phys. Appl. Phys.* 43(48):483001, 2010, doi:10.1088/0022-3727/43/48/483001.
267. Jung, J. and Hwang, N., “Non-classical crystallization of thin films and nanostructures in CVD and PVD processes,” in: Neralla, S., ed., *Chemical vapor deposition - recent advances and applications in optical, solar cells and solid state devices*, InTech, ISBN 978-953-51-2572-3, 2016, doi:10.5772/63926.
268. Kromka, A., Jira, J., Stenclova, P., Kriha, V., Kozak, H., Beranova, J., Vretenar, V., Skakalova, V., and Rezek, B., “Bacterial response to nanodiamonds and graphene oxide sheets: Bacterial response to nanodiamonds and graphene oxide,” *Phys. Status Solidi B* 253(12):2481–2485, 2016, doi:10.1002/pssb.201600237.
269. Kromka, A., Potocký, Š., Domonkos, M., Martinová, L., Rysová, L., Bačáková, L., Matějka, R., and Filová, E., *Multifunkční samonosná diamantová porézní podložka pro kultivaci buněk - Utility model: UV CZ 29864*, 2016.

270. Bacakova, L., Kopova, I., Stankova, L., Liskova, J., Vacik, J., Lavrentiev, V., Kromka, A., Potocky, S., and Stranska, D., “Bone cells in cultures on nanocarbon-based materials for potential bone tissue engineering: A review: Bone cells in cultures on nanocarbon-based materials,” *Phys. Status Solidi A* 211(12):2688–2702, 2014, doi:10.1002/pssa.201431402.
271. Domonkos, M., Izak, T., Stolcova, L., Proska, J., and Kromka, A., “Fabrication of periodically ordered diamond nanostructures by microsphere lithography,” *Phys. Status Solidi B* 251(12):2587–2592, 2014, doi:10.1002/pssb.201451172.
272. Domonkos, M., Ižák, T., Štolcová, L., Proška, J., Demo, P., and Kromka, A., “Structuring of diamond films using microsphere lithography,” *Acta Polytech.* 54(5):320–324, 2014, doi:10.14311/AP.2014.54.0320.
273. Prawer, S. and Nemanich, R.J., “Raman spectroscopy of diamond and doped diamond,” *Philos. Trans. R. Soc. Math. Phys. Eng. Sci.* 362(1824):2537–2565, 2004, doi:10.1098/rsta.2004.1451.
274. J. Filik, “Raman spectroscopy: a simple, non-destructive way to characterise diamond and diamond-like materials,” *Spectrosc. Eur.* Vol. 17(No. 5):10–17, 2005.
275. Kuzmany, H., Pfeiffer, R., Salk, N., and Günther, B., “The mystery of the 1140  $\text{cm}^{-1}$  Raman line in nanocrystalline diamond films,” *Carbon* 42(5–6):911–917, 2004, doi:10.1016/j.carbon.2003.12.045.
276. Wang, Q., Gu, C.Z., Xu, Z., Li, J.J., Wang, Z.L., Bai, X.D., and Cui, Z., “Diamond cone arrays with controlled morphologies formed by self-organized selective ions sputtering,” *J. Appl. Phys.* 100(3):034312, 2006, doi:10.1063/1.2222064.
277. Domonkos, M., Izak, T., Babchenko, O., Varga, M., Hruska, K., and Kromka, A., “Mask-free surface structuring of micro- and nanocrystalline diamond films by reactive ion plasma etching,” *Adv. Sci. Eng. Med.* 6(7):780–784, 2014.
278. Chao, C.L., Chou, W.C., Ma, K.J., Chen, T.T., Liu, Y.M., Huang, S.W., and Lin, H.Y., “Machining of CVD diamond film by RIE, laser ablation and thermochemical polishing (Ultra-precision machining),” *Proc. Int. Conf. Lead. Edge Manuf. 21st Century LEM21* 2005(3):1063–1068, 2005.
279. Tran, D.T., Grotjohn, T.A., Reinhard, D.K., and Asmussen, J., “Microwave plasma-assisted etching of diamond,” *Diam. Relat. Mater.* 17(4–5):717–721, 2008, doi:10.1016/j.diamond.2007.12.067.
280. Yang, Q., Chen, W., Xiao, C., Hirose, A., and Sammynaiken, R., “Simultaneous growth of well-aligned diamond and graphitic carbon nanostructures through graphite etching,” *Diam. Relat. Mater.* 14(10):1683–1687, 2005, doi:10.1016/j.diamond.2005.06.009.
281. Izak, T., Kromka, A., Babchenko, O., Ledinsky, M., Hruska, K., and Verveniotis, E., “Comparative study on dry etching of polycrystalline diamond thin films,” *Vacuum* 86(6):799–802, 2012, doi:10.1016/j.vacuum.2011.07.023.

282. Tran, D.T., Fansler, C., Grotjohn, T.A., Reinhard, D.K., and Asmussen, J., “Investigation of mask selectivities and diamond etching using microwave plasma-assisted etching,” *Diam. Relat. Mater.* 19(7–9):778–782, 2010, doi:10.1016/j.diamond.2010.02.001.
283. Zou, Y.S., Ma, K.L., Zhang, W.J., Ye, Q., Yao, Z.Q., Chong, Y.M., and Lee, S.T., “Fabrication of diamond nanocones and nanowhiskers by bias-assisted plasma etching,” *Diam. Relat. Mater.* 16(4–7):1208–1212, 2007, doi:10.1016/j.diamond.2006.11.036.
284. Stolcova, L., Proska, J., Novotny, F., Prochazka, M., and Richter, I., “Periodic arrays of metal nanobowls as sers-active substrates,” TANGER, Brno, ISBN 978-80-87294-27-7: 737–741, 2011.
285. Neves, A.J. and Nazaré, M.H., “Properties, growth and applications of diamond,” IET, ISBN 978-0-85296-785-0, 2001.
286. Zou, Y.S., Yang, Y., Zhang, W.J., Chong, Y.M., He, B., Bello, I., and Lee, S.T., “Fabrication of diamond nanopillars and their arrays,” *Appl. Phys. Lett.* 92(5):053105, 2008, doi:10.1063/1.2841822.
287. Bianconi, P.A., Joray, S.J., Aldrich, B.L., Sumranjit, J., Duffy, D.J., Long, D.P., Lazorcik, J.L., Raboin, L., Kearns, J.K., Smulligan, S.L., and Babyak, J.M., “Diamond and diamond-like carbon from a preceramic polymer,” *J. Am. Chem. Soc.* 126(10):3191–3202, 2004, doi:10.1021/ja039254l.
288. Wang, S.G., Zhang, Q., Yoon, S.F., Ahn, J., Zhou, Q., Wang, Q., Yang, D.J., Li, J.Q., and Zhang Shanyong, S., “Electron field emission enhancement effects of nano-diamond films,” *Surf. Coat. Technol.* 167(2–3):143–147, 2003, doi:10.1016/S0257-8972(02)00901-5.
289. A. van der Drif, “Evolutionary selection, a principle governing growth orientation in vapor-deposited layers,” *Phil Res Rep* 22:267–288, 1965.
290. Wolter, S.D., Stoner, B.R., Glass, J.T., Ellis, P.J., Buhaenko, D.S., Jenkins, C.E., and Southworth, P., “Textured growth of diamond on silicon via in situ carburization and bias-enhanced nucleation,” *Appl. Phys. Lett.* 62(11):1215, 1993, doi:10.1063/1.108738.
291. Nebel, C.E., Shin, D., Rezek, B., Tokuda, N., Uetsuka, H., and Watanabe, H., “Diamond and biology,” *J. R. Soc. Interface* 4(14):439–461, 2007, doi:10.1098/rsif.2006.0196.
292. Ondič, L., Dohnalová, K., Ledinský, M., Kromka, A., Babchenko, O., and Rezek, B., “Effective extraction of photoluminescence from a diamond layer with a photonic crystal,” *ACS Nano* 5(1):346–350, 2011, doi:10.1021/nn1021555.
293. Ohno, T., Wadell, C., Inagaki, S., Shi, J., Nakamura, Y., Matsushita, S., and Sannomiya, T., “Hole-size tuning and sensing performance of hexagonal plasmonic nanohole arrays,” *Opt. Mater. Express* 6(5):1594, 2016, doi:10.1364/OME.6.001594.



294. Reilly, T.H., Tenent, R.C., Barnes, T.M., Rowlen, K.L., and Lagemaat, J. van de, "Controlling the optical properties of plasmonic disordered nanohole silver films," *ACS Nano* 4(2):615–624, 2010, doi:10.1021/nn901734d.
295. Trompoukis, C., Massiot, I., Depauw, V., El Daif, O., Lee, K., Dmitriev, A., Gordon, I., Mertens, R., and Poortmans, J., "Disordered nanostructures by hole-mask colloidal lithography for advanced light trapping in silicon solar cells," *Opt. Express* 24(2):A191, 2016, doi:10.1364/OE.24.00A191.
296. Ondič, L., Kůsová, K., Cibulka, O., Pelant, I., Dohnalová, K., Rezek, B., Babchenko, O., Kromka, A., and Ganesh, N., "Enhanced photoluminescence extraction efficiency from a diamond photonic crystal via leaky modes," *New J. Phys.* 13(6):063005, 2011, doi:10.1088/1367-2630/13/6/063005.
297. Akinoglu, E.M., Morfa, A., and Giersig, M., "Nanosphere lithography-exploiting self-assembly on the nanoscale for sophisticated nanostructure fabrication," *Turk. J. Phys.* 38(3):563–572, 2014, doi:10.3906/fiz-1407-9.
298. Varga, M., Remes, Z., Babchenko, O., and Kromka, A., "Optical study of defects in nano-diamond films grown in linear antenna microwave plasma CVD from H<sub>2</sub>/CH<sub>4</sub>/CO<sub>2</sub> gas mixture," *Phys. Status Solidi B* 249(12):2635–2639, 2012, doi:10.1002/pssb.201200154.
299. Potocký, Š., Ižák, T., Varga, M., and Kromka, A., "Influence of gas chemistry on Si-V color centers in diamond films," *Phys. Status Solidi B* 252(11):2580–2584, 2015, doi:10.1002/pssb.201552222.
300. Sotillo, B., Bharadwaj, V., Hadden, J.P., Sakakura, M., Chiappini, A., Fernandez, T.T., Longhi, S., Jedrkiewicz, O., Shimotsuma, Y., Criante, L., Osellame, R., Galzerano, G., Ferrari, M., Miura, K., Ramponi, R., Barclay, P.E., and Eaton, S.M., "Diamond photonics platform enabled by femtosecond laser writing," *Sci. Rep.* 6(1):35566, 2016, doi:10.1038/srep35566.
301. Portal-Marco, S., Vallvé, M.À., Arteaga, O., Ignés-Mullol, J., Corbella, C., and Bertran, E., "Structure and physical properties of colloidal crystals made of silica particles," *Colloids Surf. Physicochem. Eng. Asp.* 401:38–47, 2012, doi:10.1016/j.colsurfa.2012.03.007.
302. Jiang, P. and McFarland, M.J., "Large-scale fabrication of wafer-size colloidal crystals, macroporous polymers and nanocomposites by spin-coating," *J. Am. Chem. Soc.* 126(42):13778–13786, 2004, doi:10.1021/ja0470923.
303. Colson, P., Cloots, R., and Henrist, C., "Experimental design applied to spin coating of 2D colloidal crystal masks: a relevant method?," *Langmuir* 27(21):12800–12806, 2011, doi:10.1021/la202284a.
304. Moitra, P., Slovick, B.A., Li, W., Kravchenko, I.I., Briggs, D.P., Krishnamurthy, S., and Valentine, J., "Large-scale all-dielectric metamaterial perfect reflectors," *ACS Photonics* 2(6):692–698, 2015, doi:10.1021/acsphotonics.5b00148.

305. Weekes, S.M., Ogrin, F.Y., Murray, W.A., and Keatley, P.S., “Macroscopic arrays of magnetic nanostructures from self-assembled nanosphere templates,” *Langmuir* 23(3):1057–1060, 2007, doi:10.1021/la061396g.
306. Chandramohan, A., Sibirev, N.V., Dubrovskii, V.G., Petty, M.C., Gallant, A.J., and Zeze, D.A., “Model for large-area monolayer coverage of polystyrene nanospheres by spin coating,” *Sci. Rep.* 7:40888, 2017, doi:10.1038/srep40888.

## About the author

### Curriculum Vitae

#### **Personal data:**

**Name:** Ing. Mária Domonkos  
**Date of birth:** 21 Oct, 1987  
**Place of birth:** Dunajská Streda, Slovakia  
**Email:** mariadomonkos@gmail.com

---

#### **Education:**

Feb. 2014 – Czech Technical University in Prague  
 Faculty of Civil Engineering, Department of Physics  
 Physical and Material Engineering  
 Doctoral degree programme

2011 – 2014 Czech Technical University in Prague  
 Faculty of Nuclear Sciences and Physical Engineering  
 Physics of Nanostructures  
 Master's degree: *Preparation of periodically arranged arrays of nanostructures by the reactive ion etching method*

2007 – 2011 Czech Technical University in Prague  
 Faculty of Nuclear Sciences and Physical Engineering  
 Applications of Natural Sciences - Physical Engineering  
 Bachelor's degree: *Study of diamond thin film growth by linear-antenna microwave plasma assisted chemical vapor deposition*

2003 – 2007 Selye János Gimnázium Komárom - secondary grammar school

---

#### **Research activities:**

Oct. 2010 – Czech Academy of Sciences  
 Institute of Physics  
 Department of Optical Materials

#### **Teaching activities:**

2014/2015 Czech Technical University in Prague General Physics - compulsory 1<sup>st</sup>-year undergraduate course

#### **Other activities:**

Mar. 2008 – Mar. 2013 Hungarian Student Association Ady Endre in Prague  
 member of the organization team  
 Sept. 2008 – Mar. 2011 vice president

---

#### **Skills:**

Microsoft Office, Power Point, CorelDraw, Origin, Atlas

#### **Languages:**

Hungarian – native speaker  
 English, Czech, Slovak – upper-intermediate

**Current research interests:** nanotechnology, diamond films, carbon nanostructures, microsphere lithography, plasma etching

<b>Awards</b>	OTDK (National Scientific Students' Associations Conference), Section of Physics-Earth Science-Mathematics
2013	national round in Slovakia (Nitra, SK): section winner and conference grand prize
2015	international round (Cluj-Napoca, Ru): section 3. prize and award of Hungarian Academy of Science
2014	Nanomaterials and Nanotechnologies in Civil Engineering, CTU best presentation award

## List of publications

### Scientific journals with impact factor:

- [A1] **Domonkos, M.**, Ižák, T., Štolcová, L., Proška, J., and Kromka, A., "Fabrication of periodically ordered diamond nanostructures by microsphere lithography," *Phys. Status Solidi B* 251(12):2587–2592, 2014, doi:10.1002/pssb.201451172, IF: 1.674.
- [A2] Ižák, T., **Domonkos, M.**, Babchenko, O., Varga, M., Rezek, B., Jurka, V., Hruška, K., and Kromka, A., "Technological aspects in fabrication of micro- and nano-sized carbon based features: nanorods, periodical arrays and self-standing membranes," *J. Electr. Eng.* 66(5):282–286, 2015, doi:10.2478/jee-2015-0046., IF: 0.525.
- [A3] **Domonkos, M.**, Ižák, T., Kromka, A., and Varga, M., "Polymer-based nucleation for chemical vapour deposition of diamond," *J. Appl. Polym. Sci.* 133(29), 2016, doi:10.1002/app.43688, IF: 1.86.
- [A4] Fedorov, N., Geoffroy, G., Duchateau, G., Štolcová, L., Proška, J., Novotný, F., **Domonkos, M.**, Jouin, H., Martin, P., and Raynaud, M., "Enhanced photoemission from laser-excited plasmonic nano-objects in periodic arrays," *J. Phys. Condens. Matter* 28(31):315301, 2016, doi:10.1088/0953-8984/28/31/315301, IF: 2.649.
- [A5] Varga, M., Stehlik, S., Kaman, O., Ižák, T., **Domonkos, M.**, Lee, D.S., and Kromka, A., "Templated diamond growth on porous carbon foam decorated with polyvinyl alcohol-nanodiamond composite," *Carbon* 119:124–132, 2017, doi: 10.1016/j.carbon.2017.04.022, IF: 6.337.
- [A6] **Domonkos, M.**, Varga, M., Ondič, L., Gajdošová, L., and Kromka, A., "Microsphere lithography for scalable polycrystalline diamond-based near-

infrared photonic crystals fabrication,” *Mater. Des.* 139:363–371, 2018, doi:10.1016/j.matdes.2017.10.076, IF: 4.364.

- [A7] **Domonkos, M.**, Ižák, T., Varga, M., Potocký, Š., Demo, P., and Kromka, A., “Diamond nucleation and growth on horizontally and vertically aligned Si substrates at low pressure in a linear antenna microwave plasma system,” *Diam. Relat. Mater.* 82:41–49, 2018, doi:10.1016/j.diamond.2017.12.018, IF: 2.561.

### **Journals indexed in Web of Science/Scopus:**

- [B1] **Domonkos, M.**, Ižák, T., Štolcová, L., Proška, J., and Kromka, A., “Controlled structuring of self-assembled polystyrene microsphere arrays by two different plasma systems,” *5th International Conference Proceedings*, TANGER, Brno, ISBN 978-80-87294-47-5: 34–38, 2013.
- [B2] Štolcová, L., **Domonkos, M.**, Ižák, T., Proška, J., Procházka, M., and Kromka, A., “Plasma treatment as a versatile technique for preparation of plasmonic nanoantenna arrays,” *Progress in Electromagnetics Research Symposium (PIERS) Proceedings*, Stockholm, Sweden: 426–430, 2013.
- [B3] **Domonkos, M.**, Ižák, T., Babchenko, O., Varga, M., Hruška, K., and Kromka, A., “Mask-free surface structuring of micro- and nanocrystalline diamond films by reactive ion plasma etching,” *Adv. Sci. Eng. Med.* 6(7):780–784, 2014.
- [B4] **Domonkos, M.**, Ižák, T., Štolcová, L., Proška, J., Demo, P., and Kromka, A., “Structuring of diamond films using microsphere lithography,” *Acta Polytech.* 54(5):320–324, 2014, doi:10.14311/AP.2014.54.0320.

### **Conference proceedings:**

- [C1] **Domonkos, M.**, Ižák, T., Babchenko, O., Kromka, A., and Hruška, K., “Influence of CO<sub>2</sub> concentration on diamond film morphology in pulsed linear antenna microwave plasma CVD system,” *Proceedings of 2nd Rokytnice Educational Workshop*, Czech Republic, ISBN 978-80-260-0911-5, 2011.
- [C2] **Domonkos, M.**, Ižák, T., Proška, J., and Kromka, A., “Structuring of diamond films by reactive ion plasma etching,” *Nanomateriály a nanotechnologie ve stavebnictví*, České vysoké učení technické v Praze: 35–40, doi:978-80-01-05132-0., 2012.
- [C3] Ižák, T., Babchenko, O., Varga, M., Potocký, Š., Marton, M., Vojs, M., **Domonkos, M.** and Kromka, A., “Study of nucleation and growth of diamond thin films,” *Proceedings of the 3rd Winter Education Seminar in Rokytnice nad Jizerou*, Czech Republic, ISBN 978-80-260-3425-4: 39–49, 2012.
- [C4] **Domonkos, M.**, Ižák, T., Štolcová, L., Proška, J., and Kromka, A., “Reactive ion etching of polystyrene microspheres,” *Nanomateriály a nanotechnologie ve*

- stavebnictví*, České vysoké učení technické v Praze, ISBN 978-80-01-05334-8: 24–28, 2013.
- [C5] **Domonkos, M.**, Ižák, T., and Kromka, A., “Fabrication of self-assembled microsphere monolayers,” *Material analysis in vacuum*, Slovenská vákuová spoločnosť, Bratislava, Štrbské Pleso, Slovak Republic ISBN 978-80-971179-4-8: 125–128, 2014.
- [C6] **Domonkos, M.**, Ižák, T., Demo, P., and Kromka, A., “Applications of self-assembled 2D polystyrene nanosphere arrays,” *Nanomateriály a nanotechnologie ve stavebnictví*, České vysoké učení technické v Praze, ISBN 978-80-01-05512-0: 42–47, 2014.
- [C7] Proška, J., Štolcová, L., **Domonkos, M.**, Ižák, T., Procházka, M., and Kromka, A., “Versatile templates for ad-hoc SERS-active substrate preparation,” *International Conference on Advanced Vibrational Spectroscopy*, Vienna University of Technology, Vienna, Austria, ISBN 978-3-200-04205-6: 322–323, 2015.
- [C8] **Domonkos, M.**, “Vékony gyémánt rétegek strukturálása reaktív ionmaratással”, *National Scientific Students’ Associations Conference*, Presa Universitară Clujeană, Cluj-Napoca, Romania, ISBN: 978-973-595-834-3, 2015.
- [C9] **Domonkos, M.**, Varga, M., Ižák, T., Demo, P., and Kromka, A. “Polymer-based nucleation for diamond CVD growth”, *Conference proceedings of the NANOCON*, Brno, Czech Republic, Ostrava: Tanger, ISBN 978-80-87294-59-8, 2015.
- [C10] **Domonkos, M.**, Ižák, T., Varga, M., Potocký, Š., and Kromka, A., “Diamond growth on horizontally and vertically aligned Si substrates in low pressure surface wave plasma”, *2nd International Conference on Applied Surface Science (ICASS)*, Dalian, China, ISSN 0169-4332, 2017.
- [C11] Varga, M., Ondič, L., Hruška, K., Fait, J., **Domonkos, M.**, Prajzler, V., Potocký, Š., Remeš, Z., and Kromka, A., “Polycrystalline diamond films for optical and photonic applications”, *Conference proceedings of the NANOCON*, Brno, Czech Republic, Ostrava: Tanger, ISBN: 978-80-87294-59-8, 2017.
- [C12] Varga, M., Ondič, L., Hruška, K., Babchenko, O., **Domonkos, M.**, Prajzler, Š. Potocký, Š., Kozak, H., Remeš, Z. and Kromka, A., “Diamond in optics and photonics” *KIST-CAS-CEITEC Joint Workshop for Nanotechnology and Nanoscience*, KIST, Seoul, Korea, 2017.

### **Utility model:**

- [D1] Kromka, A., Potocký, Š., **Domonkos, M.**, Martinová, L., Rysová, L., Bačáková, L., Matějka, R., and Filová, E., Multifunkční samonosná diamantová porézní podložka pro kultivaci buněk - Utility model: UV CZ 29864, 2016